UC Berkeley

UC Berkeley Electronic Theses and Dissertations

Title

Magnetic Resonance Characterization of Structure and Dynamics in Rare Earth Phosphate Materials

Permalink

https://escholarship.org/uc/item/5pp6z1ck

Author

Stettler, Joel Michael

Publication Date

2011

Peer reviewed|Thesis/dissertation

eScholarship.org Powered by the California Digital Library
University of California

Magnetic Resonance Characterization of Structure and Dynamics in Rare Earth Phosphate Materials

by

Joel Michael Stettler

A dissertation submitted in partial satisfaction of the
requirements for the degree of
Doctor of Philosophy

in

Chemical Engineering

in the

Graduate Division

of the

University of California, Berkeley

Committee in charge:

Jeffrey A. Reimer, Chair
Lutgard C. De Jonghe
David B. Graves
Roya Maboudian

Spring 2011

Magnetic Resonance Characterization of Structure and Dynamics in Rare Earth Phosphate Materials

Copyright 2011
by
Joel Michael Stettler

Abstract

Magnetic Resonance Characterization of Structure and Dynamics in Rare Earth Phosphate Materials

by

Joel Michael Stettler

Doctor of Philosophy in Chemical Engineering

University of California, Berkeley

Jeffrey A. Reimer, Chair

This thesis develops magnetic resonance techniques to characterize the structure and proton dynamics of rare earth phosphates. Structural characterization is accomplished primarily through the use of ^{31}P magic angle spinning (MAS) nuclear magnetic resonance (NMR). Spectroscopic characterization is used to develop chemical shift references on calcium and lanthanum phosphate materials in order to better understand the phases and phosphate environments in a calcium lanthanum phosphate glass-ceramic material. Similar methods are used to characterize cerium orthopohsphate, a material that has often been called "NMR invisible" in the literature, and the phosphate structures that are formed when two differing synthetic approaches are performed.

Structural characterization is enhanced through the use of double resonance techniques, such as ^{1}H -^{31}P cross polarization (CP) MAS NMR and heteronuclear correlation (HETCOR) spectroscopy. Such techniques are a powerful way to associate protons present in the material with phosphate hosting sites in the material. In a strontium cerium metaphosphate glass-ceramic, ^{31}P MAS NMR spectroscopic, relaxation, and variable temperature techniques are used to characterize and identify the structure of this partially crystalline material, while ^{1}H -^{31}P cross polarization (CP) MAS NMR allows the preferred proton hosting site in the material to be identified.

In order to measure proton dynamics in the rare earth phosphates, field gradient NMR techniques are adapted to the particular challenges of rare earth phosphates. Relatively low proton conductivities in the materials being studied suggest that proton motion in these materials will be slow. The combination of slow proton motion, the known short ^{1}H relaxation times of rare earth phosphates, and the required high temperatures at which proton diffusion takes place rule out standard field gradient techniques that have been developed for liquids. Small scale pulsed field gradient NMR probe designs and stray field steady gradient NMR have been investigated, and methods by which one can make such measurements more straightforward are discussed. It is demonstrated that high temperature stray field steady gradient NMR methods can measure proton self diffusion in a relatively proton-rich barium lanthanum metaphosphate glass.

Dedication

Learning to do magnetic resonance well is a bit like learning to swim by jumping into the ocean. The fact that I was able to accomplish anything during my time in graduate school is a tribute to the many helping hands I received from members of the Reimer lab, the Chemical Engineering department, and the greater NMR community. I first must thank my advisor, Jeff. I consider myself lucky to have had such a knowledgeable, kind and interested mentor and friend over the past six years. Your simultaneous ability to think about the underlying physics of NMR and the experimental nuances is absolutely remarkable (and your consistent solution to check "cross diodes to ground" or to add a "shorted quarter wave" solved more experimental problems than I care to admit). To my labmates, past and present, thank you for all your help over the years and for providing me with my nuclear magnetic resonance education. Sam, thanks for teaching me standard MAS NMR techniques. To Pat McGrath, Pat Coles, and Ross, thank you for input and feedback during group meetings and the major hurdles of my education. To Shashi and Marie, thank you for taking the time to cultivate my fundamental knowledge of magnetic resonance by (slowly) reading through Slichter with me. To Paul and Brian, thank you for helping and challenging me during my intermediate graduate school years, providing suggestions when I got stuck and for being wonderful friends. To the more current members of the Reimer lab - Jon, Michael, Megan, Matt, Eric, Sean, Jian and YT - thank you for making the Reimer lab a pleasant and collaborative place to work, for helping me during my various side-investigations and for providing inspiration for new ways to better understand the systems that we are studying.

Many other people have made my time in California and graduate school wonderful. I must also thank my wonderful classmates in my program for helping me both in my coursework and in finding so many delightful distractions. Thank you for all my my friends and family, for your wonderful support.

And finally, to my wife, Barbara. Thank you so much for being such a supportive, caring, and loving person ever since the day I met you. I could not have made it this far without you.

Contents

List of Figures **v**

List of Tables **viii**

1 Introduction **1**
1.1 Motivation . . . 1
1.2 Methodology: Nuclear Magnetic Resonance . . . 2
1.2.1 Structural Studies . . . 2
1.2.2 Dynamics . . . 3
1.3 Objectives . . . 3

2 Structural Study of a Calcium Lanthanum Phosphate Glass-Ceramic **5**
2.1 Acknowledgement . . . 5
2.2 Introduction . . . 5
2.3 Methods . . . 6
2.4 Results and Discussion . . . 6
2.4.1 Calcium phosphate glass . . . 6
2.4.2 Heat treated calcium phosphate glass . . . 7
2.4.3 Melt quenched lanthanum phosphate glass . . . 8
2.4.4 Heat treated lanthanum phosphate glass . . . 9
2.4.5 Calcium lanthanum phosphate glass . . . 10
2.4.6 Heat treated calcium lanthanum phosphate glass . . . 10
2.5 Conclusion . . . 13

3 Structural Study of Strontium Substituted Cerium Phosphate **15**
3.1 Acknowledgement . . . 15
3.2 Introduction . . . 15
3.3 Methods . . . 16
3.4 Results and Discussion . . . 16
3.5 Conclusions . . . 26
3.6 Supporting Information: Results of Line Shape Analyses . . . 27

4 Proton conduction in (Ce,Sr) metaphosphate glass-ceramic composites **29**
4.1 Acknowledgement . . . 29
4.2 Abstract . . . 29
4.3 Introduction . . . 29
4.4 Experimental . . . 30
4.4.1 Sample preparation . . . 30
4.4.2 Open circuit voltage measurements . . . 30
4.4.3 Structural and chemical characterization . . . 32
4.4.4 Conductivity measurement . . . 32
4.4.5 Nuclear Magnetic Resonance measurements . . . 32
4.5 Results and discussion . . . 33
4.5.1 Characterization of the (Ce,Sr) metaphosphate . . . 33
4.5.2 Effect of crystallization and aliovalent substitution on conductivity . . . 33
4.5.3 Crystallization and aliovalent substitution effect on conductivity . . . 33
4.5.4 Identification of proton-hosting sites . . . 35
4.6 Conclusions . . . 51

5 Self Diffusion **52**
5.1 Acknowledgement . . . 52
5.2 Introduction . . . 52
5.3 Theory . . . 52
5.4 Fundamental Pulse Sequences and Practical Concerns . . . 54
5.5 Methods . . . 58
5.5.1 Development of a High Pulsed Field Gradient NMR Probe . . . 58
5.5.2 STRAy FIeld (STRAFI) NMR for High Temperature Self Diffusion Measurements . . . 60
5.6 Results and Discussion . . . 66
5.7 Conclusions . . . 70
5.8 Future Work . . . 70

Bibliography **73**

A Mathematical Analysis of Typical Experimental NMR Data **78**
A.1 Fitting Longitudinal Relaxation Data, T_1 . . . 78
A.1.1 Fitting Data from Inversion Recovery Data . . . 78
A.1.2 Fitting Saturation Recovery Data . . . 80
A.2 Fitting Spin-Spin Relaxation Data, T_2 . . . 81
A.2.1 Fitting Spin Echo Data . . . 82
A.3 Fitting NMR Spectra for Line Shape Analysis . . . 83
A.4 Fitting Field Gradient Diffusion Data . . . 85
A.4.1 Pulsed Gradient Spin Echo Experiment with Square Pulses . . . 85
A.4.2 Pulsed Gradient Spin Echo Experiment with Sinusoidal Pulses . . . 86
A.4.3 Steady Gradient Spin Echo Experiment . . . 87

B Diffusion Studies in Polymer Systems **89**
B.1 Methods . . . 89
B.2 Results of ^{7}Li Experiments in Annealed and Non-Annealed SEO4 . . . 90
B.3 Results of Variable Diffusion Time ^{7}Li Self Diffusion Experiments . . . 94
B.3.1 SEO6 Sample . . . 94
B.3.2 PEO Sample . . . 97
B.3.3 SEO5 Sample . . . 97
B.3.4 SEO2 Sample . . . 97
B.4 Results of Variable Diffusion Time ^{19}F Self Diffusion Experiments . . . 99
B.4.1 PEO Sample . . . 99
B.4.2 SEO5 Sample . . . 99
B.4.3 SEO6 Sample . . . 100
B.4.4 SEO2 Sample . . . 100

C Single T_1 Inversion Recovery Fit: Example Mathematica Code **102**

D Multiple T_1 Inversion Recovery Fit: Example Mathematica Code **106**

E Single and Multiple T_1 Saturation Recovery Fit: Example Mathematica Code **110**

F Single T_2 Spin Echo Fit: Example Mathematica Code **118**

G Multiple T_2 Spin Echo Fit: Example Mathematica Code **122**

H Line Shape Fitting: Example Mathematica Code **128**

I Single Self Diffusion Coefficient Measurement with PGSE with Square Pulses: Example Mathematica Code **138**

J Single Self Diffusion Coefficient Measurement with PGSE with Square Pulses: Example Mathematica Code **142**

K Single Self Diffusion Coefficient Measurement with STRAFI: Example Mathematica Code **148**

L Single Self Diffusion Coefficient Measurement with STRAFI: Example Mathematica Code **155**

List of Figures

2.1 ^{31}P NMR Spectrum of the Calcium Phosphate Glass 7
2.2 ^{31}P NMR Spectrum of the Heat-Treated Calcium Phosphate Glass 8
2.3 ^{31}P NMR Spectrum of the melt quenched La_2O_3 - P_2O_5 Glass Sample 9
2.4 ^{31}P NMR Spectrum of the Heat-Treated Lanthanum Phosphate Glass 10
2.5 ^{31}P NMR Spectrum of the Calcium Lanthanum Phosphate Glass 11
2.6 ^{31}P NMR Spectrum of the Heat-Treated Calcium Lanthanum Phosphate Glass . . . 12

3.1 ^{31}P NMR Spectrum of the 2.5% SrCePO4 Co-Precipitation Sample 17
3.2 ^{31}P NMR Spectrum of the 2.5% SrCePO4 Solid State Sample 18
3.3 Direct excitation ^{31}P MAS NMR of the CeP_3O_9 glass-ceramic 19
3.4 ^{31}P NMR MAS NMR of the 0%Sr $CePO_4$ Co-Precipitation Series 20
3.5 ^{31}P NMR MAS NMR of the 2.5%Sr $CePO_4$ Co-Precipitation Series 21
3.6 ^{31}P NMR MAS NMR of the 5%Sr $CePO_4$ Co-Precipitation Series 22
3.7 ^{31}P NMR MAS NMR of the 10%Sr $CePO_4$ Co-Precipitation Series 23
3.8 Summary of Relative Populations of ^{31}P Environments of $CePO_4$ Co-Precipitation Series 23
3.9 Summary of Relative Populations of ^{31}P Environments of $CePO_4$ Solid State Series . 24
3.10 ^{31}P NMR MAS NMR of the 2.5%Sr $CePO_4$ Solid State Sample 25
3.11 ^{31}P NMR MAS NMR of the 5%Sr $CePO_4$ Solid State Sample 25
3.12 ^{31}P NMR MAS NMR of the 10%Sr $CePO_4$ Solid State Sample 26

4.1 The unit cell of $CePO_4$ (b) and CeP_3O_9 (c). The PO_4 tetrahedra (or -(PO_3)- chains) can be seen along the 010 projection in a 1 x 1 x 5 supercell of CeP_3O_9 (a). 31
4.2 ^{31}P NMR XRD of $Ce_{1-x}Sr_xP_3O_9$ Glass-Ceramic Materials 34
4.3 AC conductivity of the $Ce_{1-x}Sr_xP_3O_9$ materials with respect to inverse temperature 36
4.4 Z-contrast images for the $Sr_{0.16}Ce_{0.84}P_3O_9$ glass-ceramic material. In (a), the Z-contrast imaging of the sample is shown. Figures (b) and (c) display the Ce and Sr mapping, respectively, and demonstrate qualitatively that the Ce is present predominantly in the grains and the Sr is present predominantly in the intergranular regions. 38

4.5 EDX composition analysis for the $Sr_{0.16}Ce_{0.84}P_3O_9$ glass-ceramic material. Figure (a) displays the Z-contrast imagining with two boxes indicating where the EDX composition was done. The black box shows the location of the EDX of the intergranular region (b) and the white box shows the EDX of the crystalline grains (c). 39
4.6 Direct excitation ^{31}P MAS NMR of the $Sr_0.16Ce_0.84P_3O_9$ glass-ceramic 40
4.7 Infinite temperature extrapolation of ^{31}P MAS NMR chemical shifts of the $Sr_{0.16}Ce_{0.84}P_3O_9$ glass-ceramic 42
4.8 Direct excitation ^{31}P MAS NMR of the CeP_3O_9 glass-ceramic 42
4.9 Direct excitation ^{1}H MAS NMR of the $Sr_{0.16}Ce_{0.84}P_3O_9$ glass-ceramic 44
4.10 Comparison of direct excitation ^{31}P MAS NMR and ^{1}H -^{31}P CPMAS NMR of $Sr_{0.16}Ce_{0.84}P_3O_9$ glass-ceramic sample 45
4.11 Two-dimensional ^{1}H -^{31}P ramp CP HETCOR of $Sr_{0.16}Ce_{0.84}P_3O_9$ glass-ceramic sample 46
4.12 Two-dimensional ^{31}P -^{31}P Exchange NMR Spectrum of $Sr_{0.16}Ce_{0.84}P_3O_9$ Glass Ceramic Sample with 5.5 ms Mixing Time 47
4.13 Two-dimensional ^{31}P -^{31}P Exchange NMR Spectrum of $Sr_{0.16}Ce_{0.84}P_3O_9$ Glass Ceramic Sample with 8.4 ms Mixing Time 48
4.14 Two-dimensional ^{31}P -^{31}P Exchange NMR Spectrum of $Sr_{0.16}Ce_{0.84}P_3O_9$ Glass Ceramic Sample with 2.8 ms Mixing Time 49

5.1 Gradient and RF pulse sequences used for diffusion studies 55
5.2 The top view (a) and side view (b) of the homebuilt PFG NMR probe based on the design of Zhang and Cory[47]. The NMR coil is a standard solenoid connected to a Tank circuit that has leads entering and leaving the gradient support perpendicular to the gradient coil leads, as can be seen in (a). The gradient support is made of Teflon, and is connected to a Teflon support that is connected to the brass head of the probe. In (b), the anitparallel Helmholtz gradient coils are shown, which are necessary for creating a linear magnetic field gradient in the sample volume of the probe. The dimensions of the gradient support are provided. The axis of the *rf* coil (not shown) goes from left to right parallel to the plane of the picture in the 2.75 mm region between the gradient coils. 59
5.3 Glycerol Calibration of Model PFG Probe 60
5.4 Measurement of Magnetic Field Gradient in a 300 MHz Magnet 61
5.5 Magnetic Field and Magnetic Field Gradient in the Stray Field of a 300 MHz NMR Magnet 62
5.6 Measurement of Glycerol Self Diffusion Coefficient in the Stray Field 62
5.7 Variable Temperature Calibration with Ethylene Glycol on Stray Field NMR Probe 63
5.8 STRAFI CPMG Pulse Sequence 64
5.9 STRAFI CPMG Experimental Results for 50-50 Ionic Liquid Mixture at 250°C . . . 65
5.10 STRAFI CPMG Experimental Results for 50-50 Ionic Liquid Mixture at 250°C . . . 65
5.11 STRAFI CPMG Acquisition for B1 Sample at 200°C 66
5.12 T_2 as a function Inverse Temperature for the B1 Sample 67
5.13 Self Diffusion as a function of Inverse Temperature for the B1 Sample 69

5.14 Self Diffusion of Slowly Diffusing Component as a function of Inverse Temperature for the B1 Sample 70

B.1 Temperature Dependence of ^{7}Li T_1 in Annealed and Non-Annealed SEO4 Sample . 92
B.2 Temperature Dependence of ^{7}Li self diffusion coefficients for the Annealed and Non-Annealed SEO4 Sample 93
B.3 Dependence of ^{7}Li Self Diffusion Coefficients on Diffusion Time in SEO6 Sample . . 95
B.4 Dependence of ^{7}Li Self Diffusion Coefficients on Diffusion Time in SEO6 Sample . . 95

List of Tables

2.1 ^{31}P NMR chemical shift line shape analysis for the CaP_2O_6 Glass Sample 7
2.2 ^{31}P NMR chemical shift line shape analysis for the heat-treated CaP_2O_6 Glass Sample 8
2.3 ^{31}P NMR chemical shift line shape analysis for the melt quenched La_2O_3 - P_2O_5 Glass Sample 9
2.4 ^{31}P NMR chemical shift line shape analysis for the heat-treated La_2O_3 - P_2O_5 Glass Sample 10
2.5 ^{31}P NMR chemical shift line shape analysis for the Calcium Lanthanum Phosphate Glass Sample 11
2.6 ^{31}P NMR chemical shift line shape analysis for the heat-treated CaO-La_2O_3 - $(NH_4)_2HPO_4$ Glass Sample 12

3.1 ^{31}P NMR chemical shift line shape analysis for the 0% $CePO_4$ Co-Precipitation Sample 27
3.2 ^{31}P NMR chemical shift line shape analysis for the 2.5% $CePO_4$ Co-Precipitation Sample 27
3.3 ^{31}P NMR chemical shift line shape analysis for the 5% $CePO_4$ Co-Precipitation Sample 27
3.4 ^{31}P NMR chemical shift line shape analysis for the 10% $CePO_4$ Co-Precipitation Sample 28
3.5 ^{31}P NMR chemical shift line shape analysis for the 2.5% $CePO_4$ Solid State Sample 28
3.6 ^{31}P NMR chemical shift line shape analysis for the 5% $CePO_4$ Solid State Sample . 28
3.7 ^{31}P NMR chemical shift line shape analysis for the 10% $CePO_4$ Solid State Sample . 28

4.1 Activation energies of $Ce_{1-x}Sr_xP_3O_9$ conductivity 35
4.2 ^{31}P MAS NMR chemical shift and spin-lattice relaxation (T_1) data for $Sr_{0.16}Ce_{0.84}P_3O_9$ glass-ceramic sample 41
4.3 Variable temperature ^{31}P MAS NMR chemical shift data for $Sr_{0.16}Ce_{0.84}P_3O_9$ glass-ceramic sample 43
4.4 Infinite temperature extrapolations of ^{31}P MAS NMR chemical shift data for $Sr_{0.16}Ce_{0.84}P_3O_9$ glass-ceramic sample 43

5.1 Equations describing signal attenuation due to diffusion and relaxation during field gradient NMR experiments 54
5.2 Summary of Measured Self Diffusion Coefficients in B1 Sample 68

B.1 Co-Block Polymer Samples Studied with ^{7}Li and ^{19}F PFG NMR 89
B.2 Summary of Variable Temperature ^{7}Li T_1 in Annealed and Non-Annealed SEO4 Sample 91
B.3 Summary of Variable Temperature ^{7}Li Self Diffusion Study in Annealed SEO4 Sample 91
B.4 Summary of Variable Temperature ^{7}Li Self Diffusion Study in Non-Annealed SEO4 Sample 92
B.5 Summary of ^{7}Li Self Diffusion Coefficients in SEO6 Sample 96
B.6 Summary of ^{7}Li Self Diffusion Coefficients in PEO Sample 97
B.7 Summary of ^{7}Li Self Diffusion Coefficients in SEO5 Sample 98
B.8 Summary of ^{7}Li Self Diffusion Coefficients in SEO2 Sample 98
B.9 Summary of ^{19}F Self Diffusion Coefficients in PEO Sample 99
B.10 Summary of ^{19}F Self Diffusion Coefficients in SEO5 Sample 100
B.11 Summary of ^{19}F Self Diffusion Coefficients in SEO6 Sample 100
B.12 Summary of ^{19}F Self Diffusion Coefficients in SEO2 Sample 101

Acknowledgments

This material is based upon work supported by the Director, Office of Science, Office of Basic Energy Sciences, Materials Science Division, of the U.S. Department of Energy under Contract No. De-AC02-05CH11231. Part of this work was supported by a Air Products Fellowship Fellowship (2009).
The author would also like to acknowledge the following:
The Reimer lab, UC Berkeley, for teaching me all that I know about spectroscopy,
The De Jonghe Group, LBNL, for synthetic expertise,
Dr. Shashi Vyas, LBNL, for such insightful discussions,
Undergraduate researchers Hassan Khan, Diana Rodriguez-Ortiz, Juan Lucio-Vega and Yuping Li, for their hard work
ChemE Class of 2005, UC Berkeley, for keeping me focused,
Mrs. Barbara Stettler, for keeping me distracted.

Chapter 1

Introduction

1.1 Motivation

Proton conducting electrolytes are an essential component of hydrogen fuel cells that operate below 800°C. Current hydrogen fuel cell research and development is largely focused on polymer-based proton exchange membranes (PEMs) such as perfluorinated co-polymers with sulfonated side-branches (e.g., Nafion), which are limited in operational temperatures (less than 150°C) and require very expensive platinum or platinum alloys as a catalyst[1]. Furthermore, at low temperatures such catalysts are very sensitive to CO[5]. An increase in operating temperatures of proton conducting fuel cells to greater than 250°C results in simplifying the thermal management of the system while enabling the use of non-noble metal catalysts.

Solid oxide fuel cells (SOFCs) have managed to avoid the requirement of platinum as a catalyst, but unfortunately must be maintained at very high temperatures (greater than 600°C) in order to have an efficient oxygen anion conducting membrane. As a result, SOFCs require longer startup times for the membrane to reach operating temperatures and require expensive materials that can withstand such operating conditions.

The combination of these factors points to the necessity of exploring inorganic proton conductors capable of operating in the 250-500°C temperature range[1, 2, 3]. This opens the door to the possibility of formulating effective non-noble metal catalysts, avoiding the platinum-based catalysts that have so far remained a significant and irreducible cost factor in lower temperature systems. One approach to attaining the said temperature region would be to combine inorganic nanocomposite electrolytes with non-noble metal catalysts to enable hydrogen or bio(m)ethanol fuel cells operating in the 250-500°C range. It is hypothesized that a nanocomposite proton conductor composed of aliovalently-substituted rare earth phosphates would retain the high temperature stability of rare earth phosphates (e.g. lanthanum or cerium phosphates) while displaying elevated levels of proton conduction.

1.2 Methodology: Nuclear Magnetic Resonance

Nuclear magnetic resonance offers a microscopic perspective of materials that is rich in structural and dynamic information. The characteristic frequencies at which nuclei absorb *rf* radiation provide a very sensitive probe into the local electronic environment of the individual nucleus. This information can be further manipulated to provide insight into the internuclear chemical connectivity as well as the physical proximity to other nuclei, providing an instructive picture of the microstructure of the material. Additionally, the stochastic phenomena that relax nuclear magnetic resonance signals are often correlated to macroscopic transport processes, such as conduction, and can be studied by a range of relaxation and imaging techniques to yield very useful dynamic information.

1.2.1 Structural Studies

^{31}P NMR chemical shifts are very responsive to the chemical environment of the phosphorus nuclei, providing information about the electronic environment, internuclear connectivity, and physical proximity to other nuclei. In phosphate materials, the $(PO_4)^{3-}$ tetrahedron can polymerize when one of the oxygen atoms on the $(PO_4)^{3-}$ tetrahedron forms a bridging oxygen to another tetrahedron. The terminology used to describe the degree of polymerization of a phosphorus tetrahedron is based upon the number of these bridging oxygens, where a Q(n) phosphate group has n bridging and (4-n) non-bridging oxygens. The formation of a bridging oxygen bond to another phosphate tetrahedron causes results in a pull of the electronic density away from the phosphorus nucleus, causing the observed NMR chemical shift to be increasingly negative. As a result, a Q(3) nucleus is more negatively shifted than a Q(2) nucleus, which in turn is more negatively shifted than a Q(1), and so on[36].

The network modifying counterions affect the NMR chemical shift of the phosphate material as well. The counterion chemical potential (z/a), defined as the ratio of the charge of the counterion (z) and the apparent ionic radius (a), plays a significant role in polarizing the phosphorus-oxygen bond[11]. An increase in counterion chemical potential will pull more electron density from the phosphorus to the oxygen, causing an increasingly negative NMR chemical shift, thus having a direct effect on the chemical shift of the material. Additionally, an increase in the network modifier to phosphate ratio will typically decrease the length of polymerized phosphate chains, which brings about an increase in the number of Q(1) nuclei in the ^{31}P NMR spectrum.

Proton (^{1}H) NMR spectroscopy directly probes the conducting moiety in proton-conducting materials, allowing the investigator to probe the environment of the proton using ^{1}H NMR spectroscopy and standard NMR relaxation experiments. Furthermore, a quantitative measurement of the number of protons present in each environment can be made because NMR signal is proportional to the number of spin-bearing particles (e.g., ^{1}H , ^{31}P) present in the sample. Such information can be connected to the phosphate structure through the use of ^{1}H -^{31}P double resonance techniques, which allow the researcher to associate the ^{1}H environments with the hosting ^{31}P environments.

1.2.2 Dynamics

Magnetic resonance methods can be used to investigate both self-diffusion, that is, the translational displacements of molecules as a consequence of Brownian motion, and interdiffusion of molecules of different species that are initially separated[4]. In the case of the materials being studied, the self-diffusion of protons in the proposed proton conducting membrane is of interest in order to better understand the dynamics of proton movement through the material. Field gradient nuclear magnetic resonance techniques allow the researcher to measure the self diffusion of nuclei over a range of time and length scales.

1.3 Objectives

This work is a part of a larger research program that focuses on the design, synthesis and characterization of new materials for proton fuel cell membranes operational in the temperature region of 200-500°C. This is accomplished by a multidisciplinary approach, in particular, a combination of theoretical, synthetic and diagnostic approaches. The goal of this work is to develop a methodology to help answer the following questions about the rare earth phosphate materials under investigation:

1. Where are the protons?

The rare earth metaphosphate materials examined in this work include glasses, glass-ceramics, and ceramics that have varying degrees of disorder and a great deal of structural heterogeneity. This means that while we might expect protons in these materials to exist as either a P-O-H proton or a water proton associated with the surface or bulk of the material, there can be numerous types of phosphates on which these protons can sit. Furthermore, these protons can have microstructural domains that preferentially host protons, especially as these materials are lowered to room temperature following synthesis.

In order to answer this question, standard ^{31}P techniques such as magic angle spinning (MAS), relaxation studies, and ^{31}P -^{31}P exchange experiments will be used to develop an understanding of the phosphate sites and structure in the material. When possible, this information will then be combined with ^{1}H and ^{1}H -^{31}P double resonance experiments, which provide insight into the proton environement(s) and allow ^{1}H environments to be associated with hosting ^{31}P environments.

2. Are these protons mobile?

Once the protons in potential proton-conducting materials have been identified, it will be helpful to understand which of these protons are mobile. Correlating the protons themselves to the proton-hosting environments in these materials, as mentioned above, will provide some insight into whether of not the protons are likely to contribute to macroscopic proton transport. There are a variety of NMR techniques, such as NMR relaxation experiments, that allow the experimenter to observe the presence of proton motion on various time scales. Self diffusion studies, mentioned again further below, are even more helpful because they provide a (quantitative) measurement of

the proton self diffusion coefficient in the materials, which allows the researcher to compare these results to those found from other characterization techniques. These methods have been used extensively in other systems, and will be adapted to the unique limitations of rare earth phosphates.

3. How mobile?

While a great deal of information about proton transport in these materials can be gathered through various transport and ac impedance techniques, NMR is somewhat unique in not only being able to identify both mobile and static protons, but diffusometry techniques are also able to quantify the proton motion in terms of a self-diffusion coefficient. Furthermore, variable temperature relaxation and self-diffusion studies allow measurement of the activation energy associated with the processes involved, allowing for comparison with activation energies predicted both from first principle studies and from conductivity measurements made on the materials themselves.

4. How do we get more (mobile) protons into the material?

By combining the studies of the phosphate structure of the material, the identification of those phosphate groups actually hosting protons, and the quantification of proton motion, a better understanding of what phosphate structures are necessary for facile proton conduction will be found.

The work that follows strives to adapt nuclear magnetic resonance techniques to the idiosyncrasies of rare earth proton conducting materials in order to address these questions.

Chapter 2

Structural Study of a Calcium Lanthanum Phosphate Glass-Ceramic

2.1 Acknowledgement

The author gratefully acknowledges the contribution of Dr. Guojing Zhang, a material science researcher in the group of Professor Lutgard De Jonghe at Lawrence Berkeley National Laboratory, to this work.

2.2 Introduction

Bright field transmission electron microscopy (TEM) of a $La(PO_3)_3$-$Ca(PO_3)_2$ glass-ceramic system demonstrated the two-phase structure of this composite and suggests that one component is crystalline and the other is amorphous[6]. Zhang et al. concluded, based on local energy dispersive X-ray spectroscopy (EDS) analysis of the different phase regions, that the structure consisted of amorphous $Ca(PO_3)_2$ intertwined with a crystalline $La(PO_3)_3$ with a grain size of a few hundred nanometers. X-ray diffraction (XRD) also indicated that the only crystalline material present was $La(PO_3)_3$.

In this chapter, a dual-phase glass-ceramic composite consisting of intertwined $La(PO_3)_3$ and $Ca(PO_3)_2$ phases is characterized using ^{31}P magic angle spinning (MAS) NMR spectroscopy. Because of the complexity of the resulting ^{31}P MAS spectrum of this sample, a series of chemical shift references were developed by synthesizing and characterizing reference compounds consisting of calcium phosphate ($Ca(PO_3)_2$) glass, calcium phosphate glass-ceramic, lanthanum metaphosphate ($La(PO_3)_3$) glass, lanthanum metaphosphate glass-ceramic, and the $CaLa(PO_3)_5$ glass. The ^{31}P NMR lineshapes of the calcium region of the glass-ceramic composite are narrow, which would normally indicate that the calcium (rather than the lanthanum) phase is highly ordered and crystalline. This discrepancy between the X-ray characterization and the ^{31}P NMR may be interesting in light of recent observations by others[7] who have seen such contradictions as a means of yielding insight into the order and disorder present in nanoscale systems.

2.3 Methods

Glasses of composition $Ca(PO_3)_2$, $La(PO_3)_3$, and $CaLa(PO_3)_5$ was prepared as described in Zhang et al [6]. Of note for this analysis is that a mixture of $CaCO_3$, La_2O_3, and $(NH_4)_2HPO_4$ were used as starting materials for these mixtures and the molar ratio 1:0.5:5 was used for the $CaLa(PO_3)_5$ glass. This mixture was heated to 1300°C in air, held at that temperature for 30 minutes, and then poured onto a preheated stainless steel plate, in air, forming a clear glass (designated as glass). Some of this same sample was further transformed at 800°C for 20 hours, in air, to form a glass-ceramic (designated as glass-ceramic).

Solid state ^{31}P NMR spectra were collected on a LapNMR (Tecmag) spectrometer operating at 26.56069 MHz with a Doty, magic angle spinning (MAS) probe DSI-945. All NMR spectra were collected at a spinning rate of 11kHz. The 90 degree pulses were 2µs and the recycle delays between subsequent scans were set to 600 seconds to ensure complete relaxation. All chemical shifts are reported with respect to 85% phosphoric acid.

The data presented below was fitted using a nonlinear regression package Mathematica. All peaks were fit using Gaussian lineshapes for the data, of form

$$S(x) = A * Exp(-\frac{(x-C)^2}{2*W^2})$$

The use of nonlinear regression fitting techniques for multiple Gaussian systems are discussed further in the Appendix.

2.4 Results and Discussion

As was described Chapter 1, ^{31}P NMR chemical shifts are very responsive to the chemical environment of the ^{31}P nucleus. The ^{31}P chemical shift environments of the rare earth phosphates studied here are very dependent on both the degree of phosphate connectivity and on the network modifying counterion(s) proximate to the ^{31}P nucleus. The chemical shift environment is further complicated for glasses, which have a high degree of disorder that causes distributions of chemical shifts and a subsequent broadening of NMR peaks. For calcium phosphate glasses, the chemical shift ranges from -8 ppm (Q(1)) to -44 ppm (Q(3)), whereas for lanthanum phosphate glasses the expected shifts are between -30 ppm (Q(1)) to -46 ppm (Q(3))[8, 9, 10].

2.4.1 Calcium phosphate glass

Figure 2.1 displays the one dimensional ^{31}P NMR spectrum of a calcium phosphate glass prepared as described above. The broad Gaussian peak centered at -29.0 ppm is indicative of a distribution of Q(2) environments. Also discernible is a peak centered at -11.2 ppm which indicates that a small percentage of the phosphorus nuclei are in the Q(1) form. This means that the glass is made of long chains of phosphate Q(2) tetrahedra with very few Q(1) ends so that the ratio of ^{31}P nuclei in Q(2) form to that in Q(1) form is very high (see Table 2.1 for populations). A lineshape analysis further reveals the existence of a weak yet broad peak centered at -41.0 ppm. This is not surprising since a small percentage of Q(3) type polymerization has been observed before

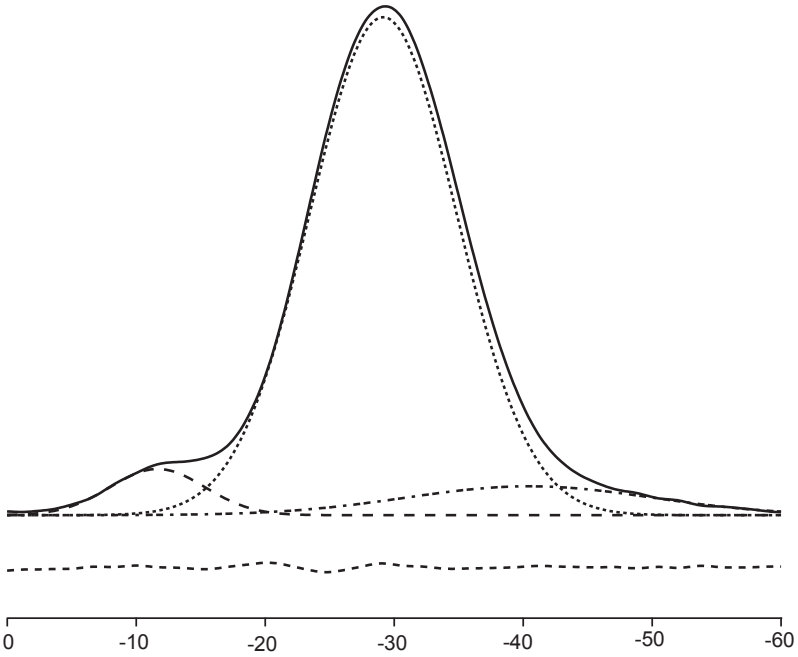


Figure 2.1: ^{31}P NMR spectrum of the calcium phosphate glass at 65.6 MHz and 11 kHz MAS. Chemical shifts are reported with respect to 85% phosphoric acid.

at this molar ratio of CaO:P_2O_5 [8, 9]. A summary of the chemical shifts and the populations in the different ^{31}P environments is outlined in Table 2.1.

Table 2.1: Summary of fitting parameters for peaks in Figure 2.1.

CaP_2O_6 Glass	**Chemical Shift**	**% Population**	**Linewidth**	**Shape**
Peak 1	-29.0 ppm	86.4%	5.7 ppm	Gaussian
Peak 2	-11.2 ppm	5.2%	3.7 ppm	Gaussian
Peak 3	-41.0 ppm	8.2%	9.6 ppm	Gaussian

2.4.2 Heat treated calcium phosphate glass

Figure 2.2 displays the one-dimensional ^{31}P NMR spectrum of the heat-treated calcium phosphate glass. The spectrum is strikingly different from the glass melt spectrum. The appearance of sharp peaks indicates crystallization. The chemical shifts at -28.7 ppm, -32.1 ppm and -34.1 ppm point to three distinct Q(2) environments. Noticeably the Q(1) population, present in the non heat-treated glass, vanishes upon heat treatment. The formation of this dual phase glass ceramic is

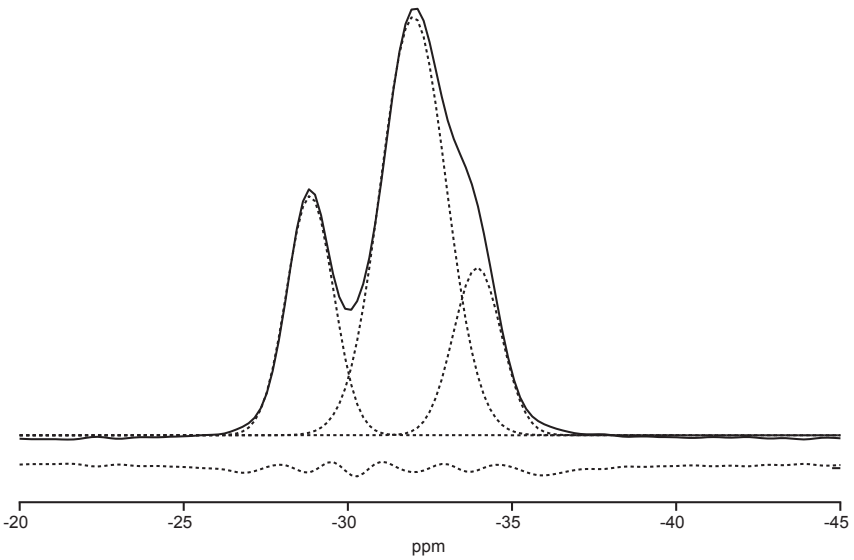


Figure 2.2: ^{31}P NMR spectrum of the heat treated calcium phosphate glass at 65.6 MHz and 11 kHz MAS. Chemical shifts are reported with respect to 85% phosphoric acid.

corroborated by the materials transition from clear transparency to opalescence as a result of the heat treatment. Assignment of these peaks to the phosphorus environments described in the X-ray crystal structure is difficult since there is no evidence of crystallographically distinct phosphorus sites. However, there is evidence of differing Ca-O bond lengths due to the two coordination environments for Ca^2+, which can result in differing degrees of P-O bond polarization and multiple ^{31}P chemical shifts. It will be instructive to compare our chemical shift values with those of pure crystalline CaP_2O_6 in the future. The results of line shape analysis are tabulated in Table 2.2.

Table 2.2: Summary of fitting parameters for peaks in Figure 2.2.

CaP_2O_6 Glass (Heat Treated)	**Chemical Shift**	**% Population**	**Linewidth**	**Shape**
Peak 1	-28.7 ppm	23.6%	0.8 ppm	Gaussian
Peak 2	-32.1 ppm	67.0%	1.2 ppm	Gaussian
Peak 3	-34.1 ppm	9.4%	0.8 ppm	Gaussian

2.4.3 Melt quenched lanthanum phosphate glass

Figure 2.3 displays the one-dimensional ^{31}P NMR spectrum of La_2O_3 $(NH_4)_2HPO_4$ glass prepared as described above. The broad nature of the dominant peak at -35.1 ppm shows that the material is predominantly amorphous. Further, most of the phosphorus population is in a Q(2) environment (97.4%) which signifies very long chains of Q(2) tetrahedra. The chemical shifts,

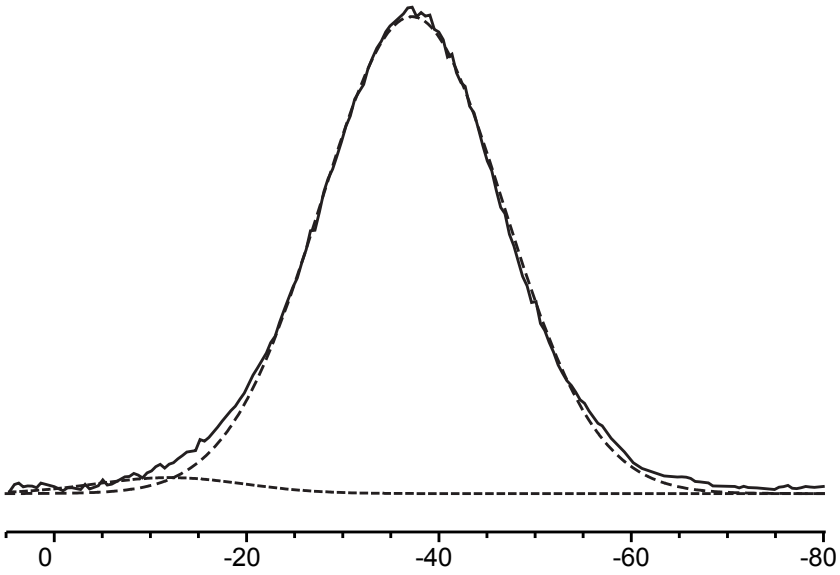


Figure 2.3: ^{31}P NMR spectrum of the lanthanum phosphate glass at 65.6 MHz and 11 kHz MAS. Chemical shifts are reported with respect to 85% phosphoric acid.

linewidths and populations are listed in Table 2.3.

Table 2.3: Summary of fitting parameters for peaks in Figure 2.3.

LaP_3O_9 Glass	**Chemical Shift**	**% Population**	**Linewidth**	**Shape**
Peak 1	-9.9 ppm	2.6%	7.7 ppm	Gaussian
Peak 2	-35.1 ppm	97.4%	9.5 ppm	Gaussian

2.4.4 Heat treated lanthanum phosphate glass

Figure 2.4 displays the one-dimensional ^{31}P NMR spectrum of the heat-treated lanthanum phosphate glass. Effects of crystallization are evident in the appearance of distinct peaks. A lineshape analysis reveals two Q(2) peaks at -32.3 ppm and -45.3 ppm. These peaks compare well with the spectrum reported for LaP_3O_9 in a previous study[10]. There, crystalline lanthanum metaphosphate gave ^{31}P resonances at similar chemical shifts and the reported population ratios were appropriate to the phosphorus populations described by the crystal structure. The broad linewidths point to a partially amorphous, glass-ceramic composition. Finally, 8% of the phosphorus nuclei are in an amorphous Q(3) environment. The lineshape analysis results are tabulated in Table 2.4.

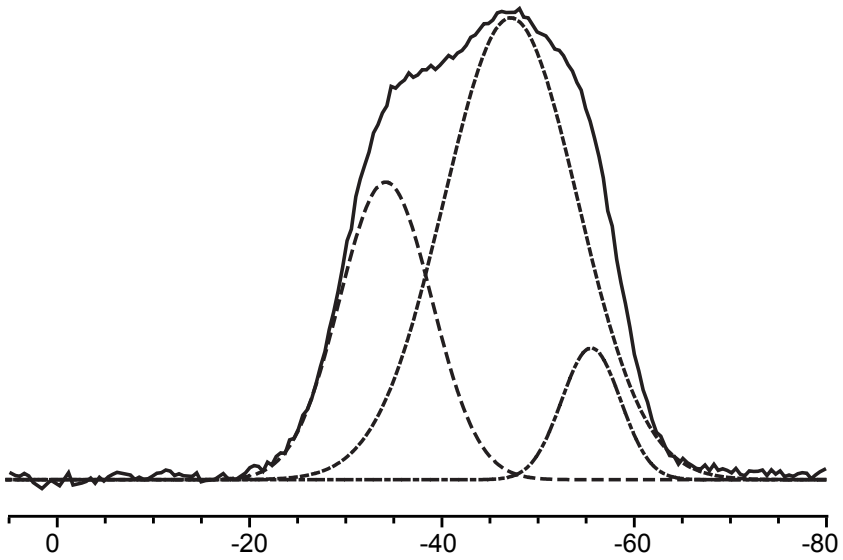


Figure 2.4: ^{31}P NMR spectrum of the heat treated lanthanum phosphate glass at 65.6 MHz and 11 kHz MAS. Chemical shifts are reported with respect to 85% phosphoric acid.

Table 2.4: Summary of fitting parameters for peaks in Figure 2.4.

LaP_3O_9 Glass (Heat Treated)	**Chemical Shift**	**% Population**	**Linewidth**	**Shape**
Peak 1	-32.3 ppm	28.3%	4.8 ppm	Gaussian
Peak 2	-45.3 ppm	63.7%	6.9 ppm	Gaussian
Peak 3	-53.6 ppm	8.0%	3.1 ppm	Gaussian

2.4.5 Calcium lanthanum phosphate glass

The ^{31}P NMR spectrum of the $CaLa(PO_3)_5$ glass composite in Figure 2.5 shows that the material is largely amorphous with a Q(2) peak at -31.2 ppm dominating the spectrum. Similar to the calcium phosphate and lanthanum phosphate melt quenched glasses, the composite glass is also composed of very long chains of Q(2) tetrahedra. A small peak at -12.1 ppm indicates a small percentage of terminal phosphate tetrahedra. The lineshape analysis results are tabulated in Table 2.6.

2.4.6 Heat treated calcium lanthanum phosphate glass

Figure 2.6 shows the ^{31}P NMR spectrum representing the various chemical environments for phosphorus in the heat treated calcium lanthanum phosphate glass composite. As a result of the heat treatment, the otherwise disordered glass separates into regions of lanthanum phosphate and calcium phosphate phases. The TEM images of the material confirm this phase separation[6]. On

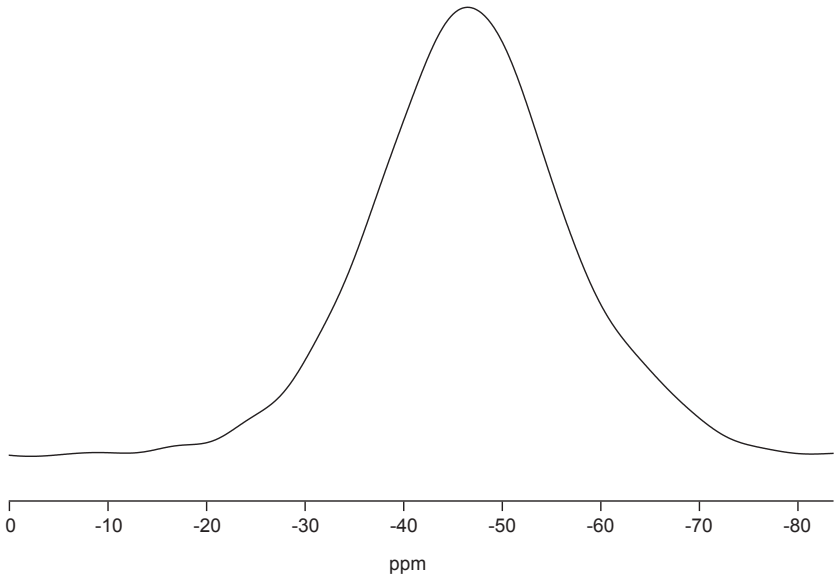


Figure 2.5: ^{31}P NMR spectrum of the heat treated calcium lanthanum phosphate glass at 65.6 MHz and 11 kHz MAS. Chemical shifts are reported with respect to 85% phosphoric acid.

Table 2.5: Summary of fitting parameters for the calcium lanthanum phosphate glass sample. The line shape analysis corresponds to those peaks seen in Figure 2.5.

La_2O_3 $(NH_4)_2HPO_4$ Glass	**Chemical Shift**	**% Population**	**Linewidth**	**Shape**
Peak 1	-12.1 ppm	3.2%	3.8 ppm	Gaussian
Peak 2	-31.2 ppm	96.8%	8.6 ppm	Gaussian

the basis of the information gleaned from the pure lanthanum phosphate and calcium phosphate glasses, as well as the impact of the heat treatment on these materials, a lineshape analysis was performed. A summary of chemical shifts and the corresponding chemical environments is presented in Table 2.4. The results of the ^{31}P MAS NMR study reveal the coexistence of partially crystalline LaP_3O_9 with partially crystalline calcium phosphate regions. The Q(2) peaks of LaP_3O_9 are consistent with literature values. All chemical shift values of the heat treated composite glass correspond to the individual heat treated lanthanum phosphate and calcium phosphate component glasses: The peaks at -28.5,-33.7, and -31.7 correspond to the chemical shifts seen in heat treated calcium phosphate glass, and the peaks at -35.1, -44.7, and -48.9 correspond to the chemical shifts seen in the heat treated lanthanum phosphate glass. The linewidths of the peaks from this analysis also agree with that seen from the analysis of the heat treated calcium and lanthanum phosphate glasses. The heat treated calcium phosphate has vary narrow lineshapes, indicative of a vary narrow distribution of phosphate environments and generally associated with a crystalline material. The heat treated lanthanum phosphate glasses have much broader lineshapes than the calcium

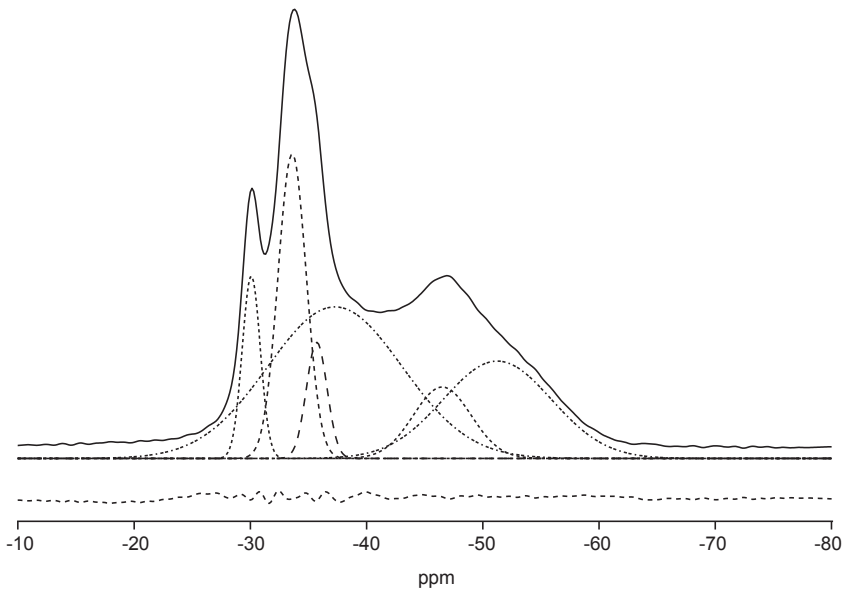


Figure 2.6: ^{31}P NMR spectrum of the heat treated calcium lanthanum phosphate glass at 65.6 MHz and 11 kHz MAS. Chemical shifts are reported with respect to 85% phosphoric acid.

phosphates, suggesting a distribution of bond lengths in the heat treated lanthanum phosphate phase. Although the lineshapes of the lanthanum phosphate are greatly narrowed when compared to the melt-quenched glass, it maintains a surprisingly large linewidth for a crystalline material.

Curiously, NMR lineshape analysis provides evidence of partial crystallization in the calcium phosphate regions, a fact that is not corroborated by TEM. Although it is true that the TEM technique reveals highly localized and sample dependent information and may not have accessed the regions of crystallinity, this is somewhat surprising since the results of the ^{31}P NMR analysis did not observe the presence of any calcium phosphate glass component.

Table 2.6: Summary of fitting parameters for peaks in Figure 2.6.

La_2O_3 $(NH_4)_2HPO_4$ HT Glass	**Chemical Shift**	**% Population**	**Linewidth**	**Shape**
Peak 1	-28.5 ppm	6.5%	0.7 ppm	Gaussian
Peak 2	-33.7 ppm	5.1%	0.8 ppm	Gaussian
Peak 3	-31.7 ppm	15.8%	1.0 ppm	Gaussian
Peak 4	-35.1 ppm	40.0%	5.3 ppm	Gaussian
Peak 5	-44.7 ppm	8.9%	2.4 ppm	Gaussian
Peak 6	-48.9 ppm	23.6%	5.0 ppm	Gaussian

There are unfortunately few spectroscopic methods available to the NMR spectroscopist seeking to better understand the nature of these interactions. ^{1}H MAS NMR experiments indicate

that the number of protons present in this sample are very small, since a proton signal was not observable above the probe background in the $La(PO_3)_3$ -$Ca(PO_3)_2$ composite material, and suggests that the chemical shift differences in the material were not due to the presence of protons being hosted on some of the phosphate tetrahedra within the two phases of this material. The lack of protons, while perhaps disappointing for the development of proton conducting materials, is probably not surprising, considering the primary means by which protons are expected to be introduced into the structure of the rare earth phosphates is by aliovalent substitution - in this case, the substitution of a Ca^{2+} for a La^{3+} - in the material. EDS results from the original study indicate that the relative ratios of La:Ca:P are 25:1:74 in the lanthanum metaphosphate phase and 0:30:70 in the calcium phosphate phase[**?**], which suggests that very little aliovalent substitution is taking place. The similarity of the chemical shifts present in the chemical shift reference materials (pure calcium phosphate and lanthanum metaphosphate) and the calcium lanthanum phosphate composite material provides additional support that the calcium and lanthanum cations remain confined to their respective phases.

The use of two dimensional experiments could provide a great deal of insight into the local structure of the material. The use of double resonance experiments, either ^{43}Ca-^{31}P or ^{138}La-^{31}P , could provide insight into the cation-phosphate interaction in these materials. Unfortunately, neither ^{43}Ca nor ^{138}La has a high natural abundance, and such experiments would be further complicated by the quadrupolar nature of these nuclei. ^{31}P -^{31}P exchange experiments could provide insight into the proximity of the various phosphate groups to one another and perhaps could even provide insight into the nature of the boundary between the two phases. Unfortunately, this experiment (and, in fact, any double resonance experiment in which the ^{31}P T_1 determines the length of the recycle delay) would be incredibly time consuming, with a single experiment time lasting on the order of weeks, because of the long T_1s in this system. As a result, there are few spectroscopic tricks that alone could provide further insight into the nature of this behavior. Some further insight might be gained by using a synthetic variable - such as heat treatment time - to understand the change in structure during the course of the crystallization process observed in this study. It is possible that at much longer heat treatment times may give rise to narrowed lineshapes in the lanthanum phosphate environments in this system.

2.5 Conclusion

In this study, the phosphate structure of a heat-treated $La(PO_3)_3$ -$Ca(PO_3)_2$ phosphate composite glass was characterized through a systematic study of as-synthesized and heat treated lanthanum and calcium phosphate glasses. The observation that the ^{31}P NMR lineshapes of the calcium region of the glass-ceramic composite are narrow, which would normally indicate that the calcium (rather than the lanthanum) phase is highly ordered and crystalline, disagrees with the results of previous X-ray characterization which determined the lanthanum metaphosphate to be the only crystalline phase present in the material. Comparison of the pure calcium and lanthanum phosphate standards with the calcium lanthanum phosphate composition material indicate that he resulting composite material is a mixture of these two phases. The data also agrees with previous EDS studies that indicate that the calcium and lanthanum cations remain largely confined to their

respective phases.

Chapter 3

Structural Study of Strontium Substituted Cerium Phosphate

3.1 Acknowledgement

The author gratefully acknowledges the contributions of Lindsey Karpowich, a material science researcher in the group of Professor Lutgard De Jonghe at Lawrence Berkeley National Laboratory, to this work.

3.2 Introduction

In developing a solid-state proton conducting membrane, it is very important to establish and ensure structural control over the materials being synthesized. While it is true that both ^{31}P NMR and IR spectroscopies can structurally characterize phosphate materials, ^{31}P NMR provides the distinct advantage of both providing quantitative information regarding the number of phosphorus nuclei in each chemical shift environment and allowing characterization of amorphous phosphorus materials.

One of many materials currently being investigated for sufficient proton conductivity is strontium doped cerium phosphate with modified grain boundaries. It is hypothesized that doping the cerium phosphate crystals with strontium will introduce structural defects in the cerium phosphate crystalline lattice, providing physical space for water molecules and improving proton conductivity through the use of water-assisted proton transport[17]. Other studies have shown that doping rare earth metaphosphates with strontium has led to an increase in protonic conduction with increasing strontium substitution[18]. There are two synthetic approaches being investigated that would allow doping of the cerium orthophosphate with small amounts of strontium. The first is a liquid state synthesis method[15] (here referred to as the co-precipitation method) that is based upon a similar method for doping $LaPO_4$, and the latter is a solid-state method[16].

In this work, these two synthetic techniques used to prepare strontium-substituted cerium orthophosphate are investigated through characterization of the phosphate structure using ^{31}P MAS NMR. The results are very suggestive that the liquid state synthesis actually creates a mixture of

cerium orthophosphate and cerium metaphosphate in which the cerium metaphosphate in the sample more readily accepts added strontium than does the cerium orthophosphate. No cerium metaphosphate is seen in samples prepared by the solid state synthesis route. In both cases, a separate chemical shift is seen with higher addition of strontium to the material, suggesting that the addition of large amounts of strontium serve only to create an additional strontium-rich phase in the material.

3.3 Methods

The rare earth nanocomposite phosphate materials were prepared by Dr. Lutgard De Jonghes group at Lawrence Berkeley National Laboratory. The cerium phosphate materials used in the discussion of structural characterization of rare earth phosphate materials were synthesized by Lindsay Karpowich. The liquid state synthesis[15] (referred to as the co-precipitation method below) was conducted by mixing a 2M solution of $Ce(NO_3)_3$ and a 0.2M solution of $Sr(NO_3)_2$ in the appropriate molar ratios for x = 0% , 2.5%, 5%, and 10% for $Ce_{(1-x)}Sr_xPO_4$, and titrating 2M solution $(NH_4)_2HPO_4$ such that P:Ce+Sr = 1. Once dry, the material is calcined for 8 hours at 800°C, ground, and pellets were made in a uniaxial die-press. The pellets are then sintered for 5 hours at 1200°C.

The solid state method[16] of preparing strontium doped cerium phosphate was done by mixing monazite $CePO_4$ powder (from Alfa Aesar, calcined 8 hours at 800°C) and $SrHPO_4$ (as received from Sigma Aldrich) in the appropriate molar ratios for x = 2.5%, 5%, 10% for $Ce_{(1-x)}Sr_xPO_4$. The materials were then placed in an attritor mill in acetone for 2 hours at 400 rpm. The material was the calcined for 5 hours at 800°C, ground, and pellets were made in a uniaxial die-press. The pellets were then sintered for 5 hours at 1200°C.

The rare earth phosphate nanocomposite and glass samples were prepared for NMR analysis by grinding the materials to a very fine powder by hand using a quartz mortar and pestle. Sample amounts ranged from 0.05 to 0.15 grams depending on material density and were packed in a SiN_3 rotor with Torlon caps. Unless otherwise noted, measurements were performed at 26.560614 MHz, the resonant frequency of 85% phosphoric acid, using a Tecmag LapNMR spectrometer and a Doty 945 MAS probe operating at approximately 11kHz. All ^{31}P MAS NMR experiments took place in a 65.61 MHz superconducting magnet. ^{31}P $\frac{\pi}{2}$ excitation pulses of 2.1μs and π excitation pulses of 4.2μs were used. Relaxation delays varied widely based on the material. Cerium phosphate materials generally required a relaxation delay of less than 5 seconds (with a T_1 for crystalline $CePO_4$ of 14 ms and a T_1 for amorphous phosphate located in cerium phosphate inter-granular boundaries of 27 ms), while crystalline and glass lanthanum phosphates generally required a delay on the order of ten minutes. Values for T_1 were found using the traditional inversion recovery experiment.

3.4 Results and Discussion

Ce^{3+} is a paramagnetic ion[19], causing increasingly negative chemical shifts and very short relaxation times[37]. Paramagnetic compounds allow for a unique approach to NMR char-

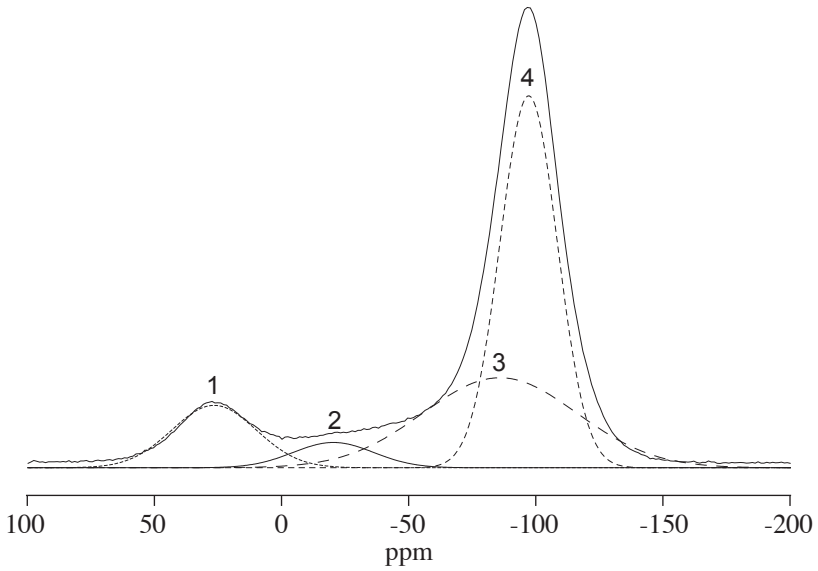


Figure 3.1: ^{31}P NMR MAS NMR spectrum of the 2.5% strontium substituted cerium phosphate co-precipitation sample at 65.6 MHz and 11 kHz MAS. Chemical shifts are reported with respect to 85% phosphoric acid.

acterization due to the sensitivity of relaxation time scales and chemical shifts to the distance separating the ^{31}P nucleus and the paramagnetic ion[20]. Because the Ce^{3+} ion causes a dramatic negative shift in cerium phosphate materials, those phosphorus nuclei located closest to the ion will have the most negative chemical shift, and will likely relax much faster than other phosphorus nuclei.

In order to clearly observe changes in each of the phosphorus environments as the amount of theoretical strontium doping increases, a line shape analysis is performed. In solid-state NMR, there tends to be a distribution of environments surrounding a mean for nuclei because the solid materials fail to be in a perfect crystal configuration, causing bond angles to vary across the sample, and resulting in the observation of inhomogeneous (i.e., Gaussian) broadening of the spectroscopic absorption. As a result, Gaussian line shapes are used to separate the NMR data into separate phosphorus environments. Because there are generally multiple environments in a solid-state material, multiple Gaussian line shapes are fit using a nonlinear regression fit function using the mathematical software package Mathematica. The details of the performing a line shape analysis using a nonlinear regression package is provided in the appendix at the end of this manuscript.

Figure 3.1 show ^{31}P MAS NMR spectra and line shape analysis of 2.5% strontium-doped $CePO_4$ as prepared by the co-precipitation method and Figure 3.2 shows the ^{31}P MAS NMR spectra and line shape analysis of 2.5% strontium-doped CePO4 as prepared by the solid-state method. The results of the line shape analyses for these two spectra are provide in Table 3.5 and Table 3.10, respectively, given in the Supporting Information section of this chapter. Comparison of the two

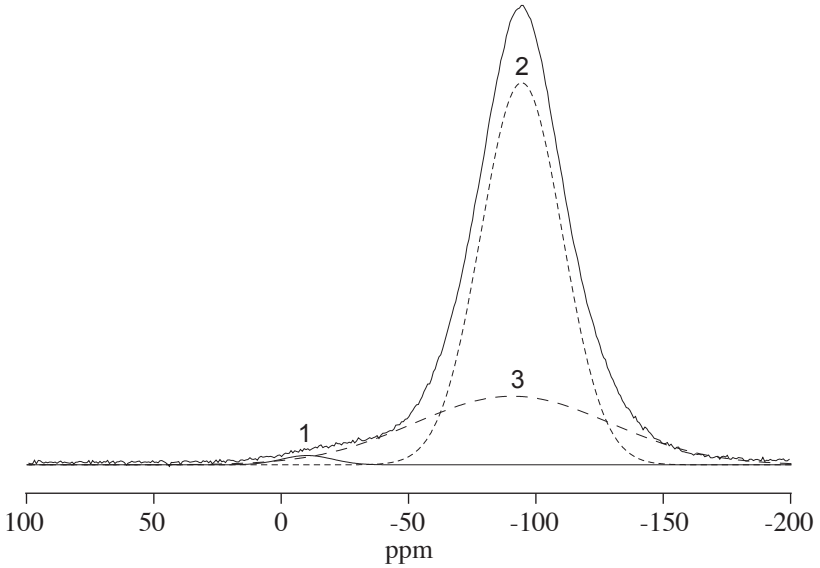


Figure 3.2: ^{31}P NMR MAS NMR spectrum of the 2.5% strontium substituted cerium phosphate solid state sample at 65.6 MHz and 11 kHz MAS. Chemical shifts are reported with respect to 85% phosphoric acid.

spectra and line shape analyses indicates several similarities. Both materials show a peak indicative of monazite cerium orthophosphate ($CePO_4$)[37] at -94 ppm, and a broad peak between -85 and -90 ppm, which suggests a disordered cerium orthophosphate state. Both samples also show a small formation of a strontium phosphate species (possibly strontium hydrogen phosphate) at -18 ppm. The most striking difference between the two spectra is the existence of a phosphorus environment possessing a chemical shift of 29 ppm, which is present in the co-precipitation sample (Figure 3.1) but is absent from the solid-state spectrum (Figure 3.1). Although this peak is located closest to Q(0) peaks, which generally falls in the range of 12-15 ppm, these chemical shifts are actually due to cerium metaphosphate (CeP_3O_9) which has a very temperature sensitive peak that appears at approximately +27.5 ppm at 20°C. Figure 3.3 below demonstrates a ^{31}P MAS NMR spectrum of cerium metaphosphate taken under identical experimental conditions at 20°C which will be discussed in greater detail in Chapter 4. While this provides a chemical shift reference for the peak at +27.5 ppm, the second characteristic peak of cerium metaphosphate at -66.8 ppm is not seen. It is possible that the broadness of the cerium metaphosphate, the cerium orthophosphate, and the disordered cerium orthophosphate peaks do not allow resolution at 11kHz MAS. Furthermore, the analysis of strontium substituted cerium metaphosphate samples described in Chapter 4 also indicates that a peak at -35 ppm is often due to a glassy strontium-rich phase that is difficult to observe and characterize with other techniques due to its lack of structure.

The structural effects of increasing amounts of strontium in a particular synthetic method can also be observed. Figures 3.4-3.7 show the ^{31}P MAS NMR spectra of a series of increasingly

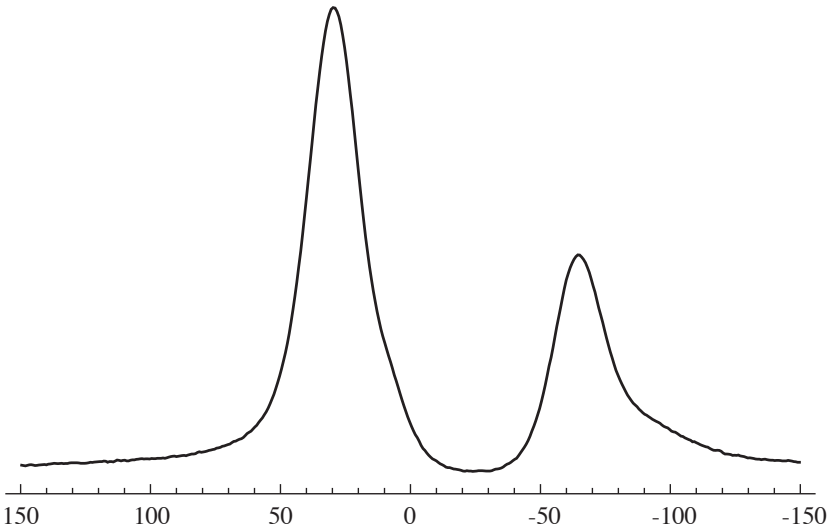


Figure 3.3: Direct excitation ^{31}P MAS NMR of the CeP_3O_9 glass-ceramic material at 25.6 MHz, 11kHz MAS speed and 20°C.

strontium-doped cerium orthophosphate samples prepared by the co-precipitation method. The corresponding line shape analyses are presented in Tables 3.1-3.4 in the Supporting Information section of this chapter with line shape analysis of the four phosphorus regions in the material. With increasing addition of strontium to the sample, one sees a clear decrease in the cerium metaphosphate peak observed at 28.9 ppm and the formation and subsequent increase of a peak at approximately -20 ppm. Because this peak at chemical shift -20 ppm appears only at higher Sr concentrations, there are two possible explanations for the nature of this peak. The first is that it could be a paramagnetically shifted glassy strontium-rich phase, similar to those seen in cerium metaphosphates (typically -35 ppm). This would not be unexpected, because this sample, which was intended to be a cerium orthophosphate, has a much higher metal concentration, so more Ce^{3+} would be expected in any additional phases of the material. A second explanation is that it is a disorganized $Sr_2P_2O_7$ or $SrHPO_4$ phase with some Ce^{3+} present in the phase which causes a change in the chemical shift. The chemical shifts of ^{31}P NMR peaks of $Sr_2P_2O_7$ without any Ce^{3+} present is -5 and -8 ppm, which is consistent with Q(1) phosphates. The ^{31}P MAS NMR chemical shift of $SrHPO_4$ without any Ce^{3+} present is +3 ppm, which is consistent with a Q(0) phosphates. Because the paramagnetic shift induced by the Ce^{3+} cation is so dramatic, the peak observed at -20 ppm could represent a disordered and paramagnetically shifted version of either material. Because ^1H MAS NMR signal is not observed in these materials, it is somewhat unlikely that this phase is $SrHPO_4$.

Figure 3.8 summarizes the changes in the relative population of the various peaks with strontium introduction in the sample. Although the populations of the peaks at approximately -94 ppm and -84 ppm change slightly with changing composition, it is expected that these are due

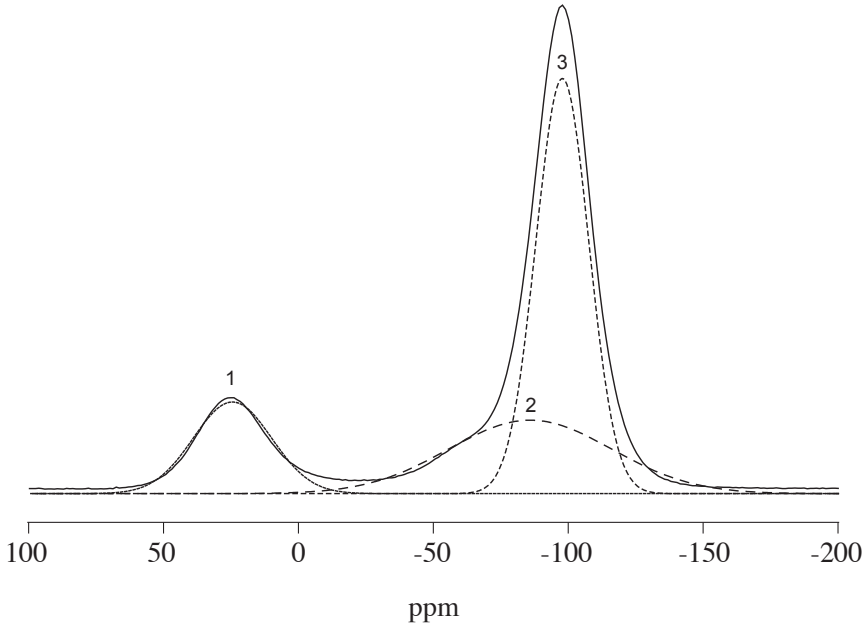


Figure 3.4: ^{31}P NMR MAS NMR spectra of the 0% strontium substituted cerium phosphate co-precipitation samples at 65.6 MHz and 11 kHz MAS. Chemical shifts are reported with respect to 85% phosphoric acid.

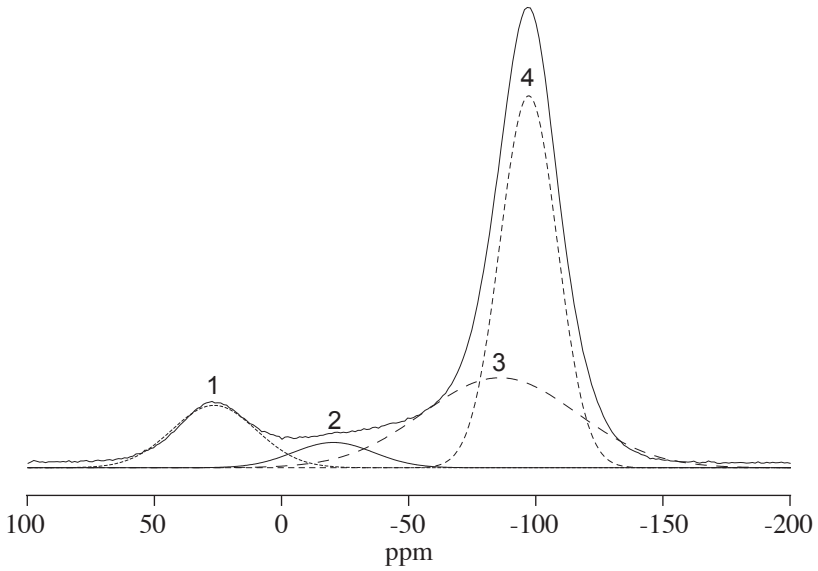


Figure 3.5: ^{31}P NMR MAS NMR spectra of the 2.5% strontium substituted cerium phosphate co-precipitation samples at 65.6 MHz and 11 kHz MAS. Chemical shifts are reported with respect to 85% phosphoric acid.

to sample variation and errors introduced during the nonlinear regression performed to provide a best fit of the ^{31}P spectrum and that these changes are not a part of a trend that occurs in this system. This is supported by the fact that the sum of the population of these two regions remains approximately constant for all four samples. It is interesting to note, however, that the line width of the organized cerium orthophosphate peak increases as the amount of strontium in the sample increases, suggesting that the crystalline cerium orthophosphate phase may achieve modest strontium introduction. Such strontium introduction would best be observed by ^{31}P -^{87}Sr double resonance techniques.

The structural effects of increasing amounts of strontium in the solid state samples can also be investigated. Figures 3.10-3.12 show the ^{31}P MAS NMR spectra of a series of increasingly strontium-doped cerium orthophosphate samples prepared by the solid state method. The corresponding line shape analyses and presented in Tables 3.5-3.7 in the Supporting Information section at the end of this chapter, with line shape analysis of the three phosphorus regions in the material. In this synthetic approach, the population of the peak at -17.9 ppm approximately matches that of the amount of strontium added to the material, suggesting that most of the strontium added to this material is proximate to the phosphorus environment represented by this peak. The broad and narrow peaks of the cerium orthophosphate (assigned as ordered and disordered cerium orthophosphate, respectively) do not undergo a significant change in line width as the amount of strontium is varied. This suggests that addition of strontium does not significantly change the structure of the cerium phosphate synthesized by the solid state synthesis. It is possible that the solubility of

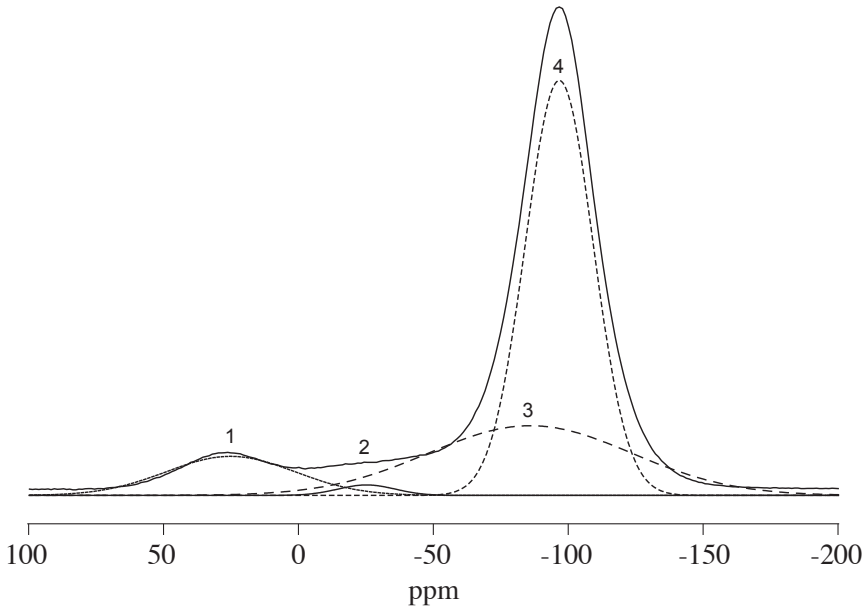


Figure 3.6: ^{31}P NMR MAS NMR spectra of the 5% strontium substituted cerium phosphate co-precipitation samples at 65.6 MHz and 11 kHz MAS. Chemical shifts are reported with respect to 85% phosphoric acid.

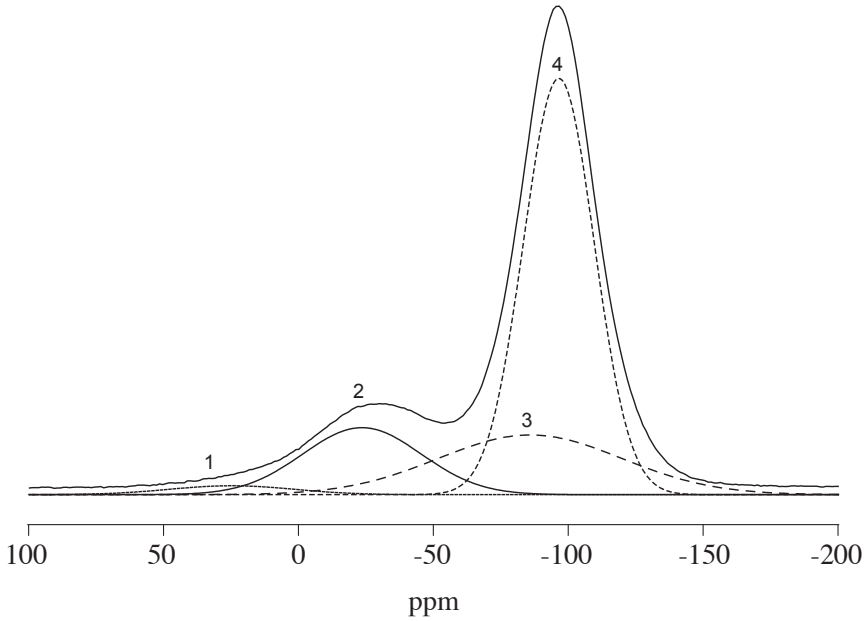


Figure 3.7: ^{31}P NMR MAS NMR spectra of the 10% strontium substituted cerium phosphate co-precipitation samples at 65.6 MHz and 11 kHz MAS. Chemical shifts are reported with respect to 85% phosphoric acid.

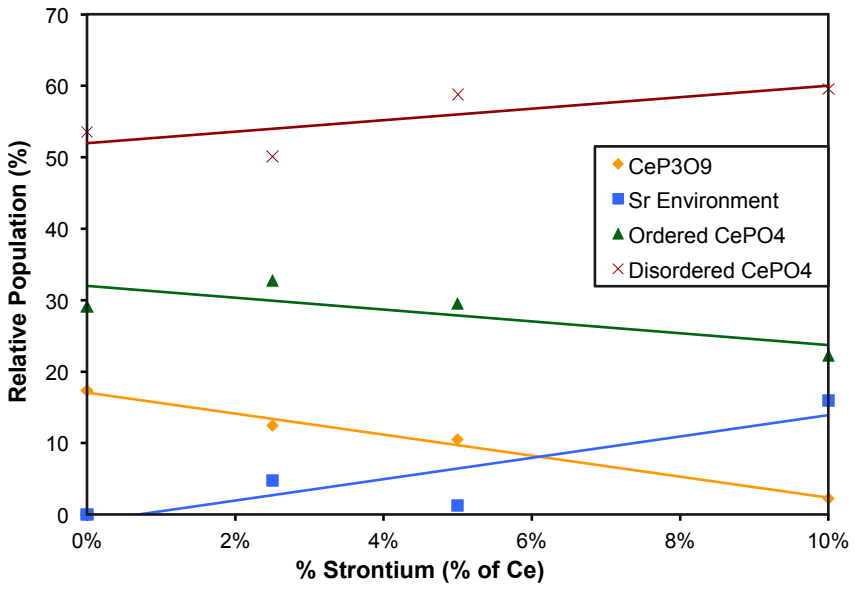


Figure 3.8: Summary of the relative populations of the ^{31}P NMR environments as a function of strontium introduction.

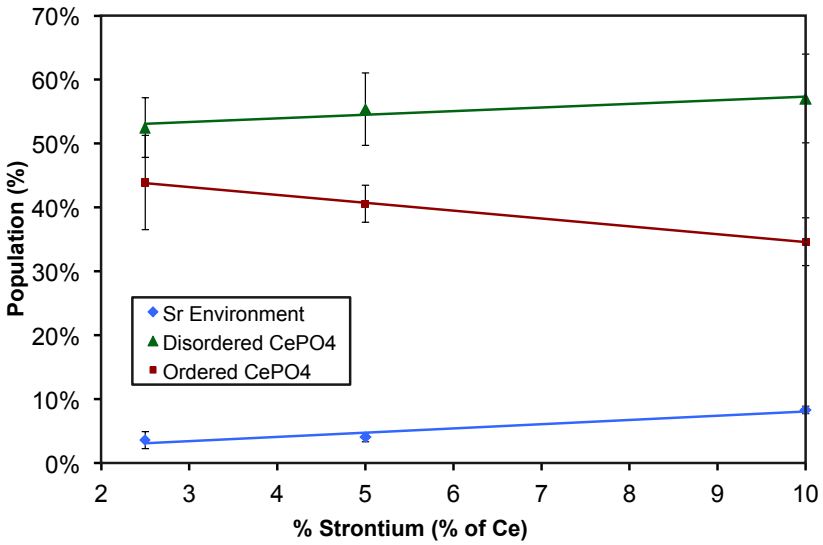


Figure 3.9: Summary of the relative populations of the ^{31}P NMR environments of the ceas a function of strontium introduction.

strontium in cerium orthophosphate is very low (lower than 2.5%) and that all strontium added above this amount simply precipitates into a separate phase that appears at -17.9 ppm. It is also possible that this method incorporates strontium into the phosphate structure and only causes a local change in the phosphate environment and does not cause a longer-range change in the phosphate structure. In either case, it is clear that the peak does not correspond to a separate $SrHPO_4$ phase, since ^{31}P MAS NMR of $SrHPO_4$ yields a single peak at +3 ppm. Such strontium introduction could be further investigated by ^{31}P -^{87}Sr double resonance techniques to confirm that the strontium is associated only with the peak at -17.9 ppm.

Figure 3.9 summarizes the changes in the relative population of the various peaks with strontium introduction in the sample. The populations of the ordered cerium orthophosphate peak does show some dependence on strontium concentration. As the amount of strontium is increased, the population percentage of ordered cerium orthophosphate decreases by amounts approximately corresponding to the percentage amount of strontium introduced to the sample. This is not surprising, since the relative amount of cerium orthophosphate decreases as the amount of strontium increases.

Both the solid state and co-precipitation cerium orthophosphate synthesis techniques result in samples with more complicated ^{31}P NMR spectra than expected. In both cases, a ^{31}P -^{31}P exchange study might provide insight into the proximate phosphate groups and provide better evidence of any phase separation that might be taking place. Unfortunately, such experiments are likely to be severely limited by the short relaxation times in this system. ^{31}P -^{87}Sr double resonance techniques would provide further insight into the location of the Sr^{2+} cations in the

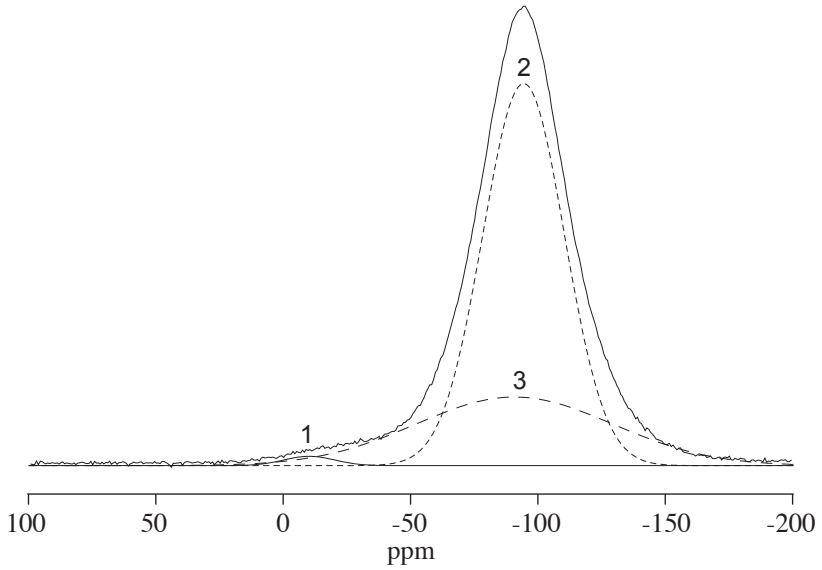


Figure 3.10: ^{31}P NMR MAS NMR spectra of the 2.5% strontium substituted cerium phosphate solid state sample at 65.6 MHz and 11 kHz MAS. Chemical shifts are reported with respect to 85% phosphoric acid.

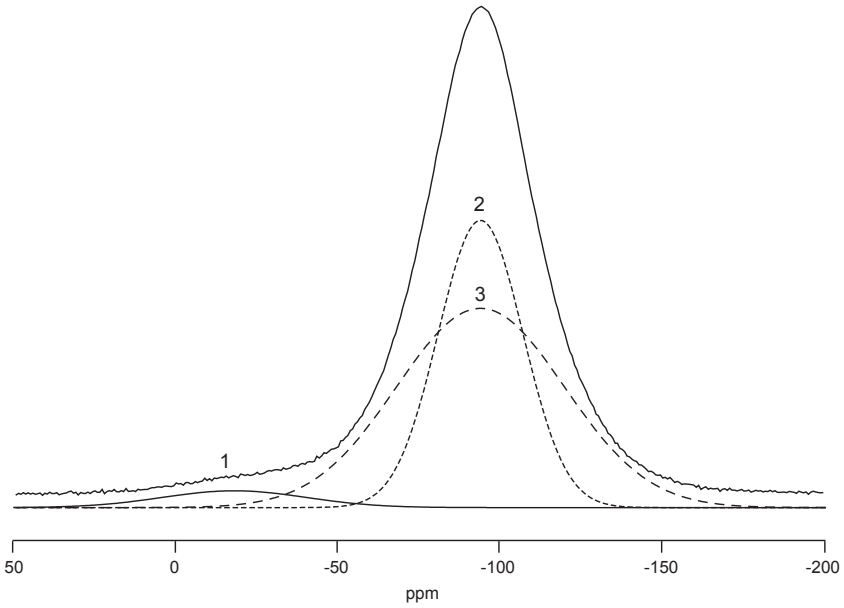


Figure 3.11: ^{31}P NMR MAS NMR spectra of the 5% strontium substituted cerium phosphate solid state sample at 65.6 MHz and 11 kHz MAS. Chemical shifts are reported with respect to 85% phosphoric acid.

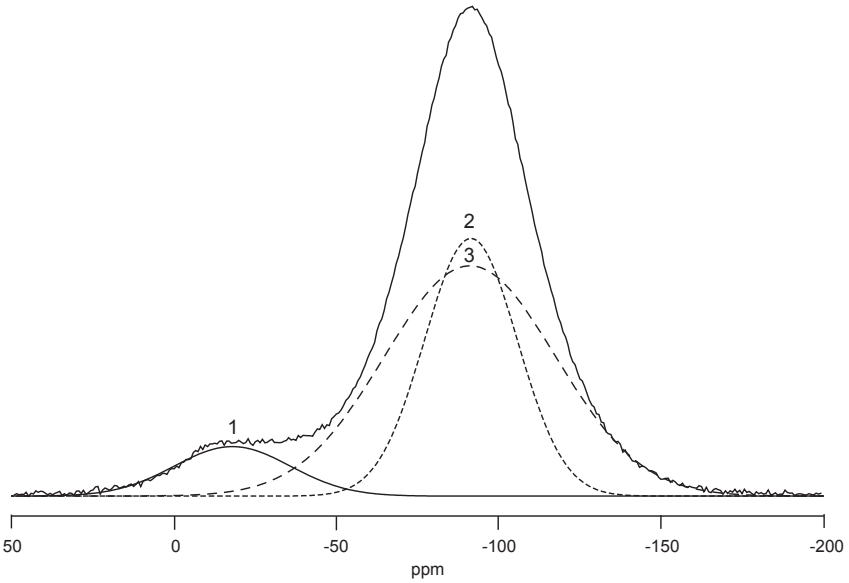


Figure 3.12: ^{31}P NMR MAS NMR spectra of the 10% strontium substituted cerium phosphate solid state sample at 65.6 MHz and 11 kHz MAS. Chemical shifts are reported with respect to 85% phosphoric acid.

material, although strontium quadrupole moment is very large and natural abundance is quite low. More recently, there has been some evidence that conductivity observed in cerium orthophosphates is primarily electronic rather than protonic[12], which may explain why the material has high conductivities when measured in air but very little or no detectable ^{1}H NMR signal.

3.5 Conclusions

In this work, these two synthetic techniques used to prepare strontium-substituted cerium orthophosphate are investigated through characterization of the phosphate structure using ^{31}P MAS NMR. The results are very suggestive that the liquid state synthesis actually creates a mixture of cerium orthophosphate and cerium metaphosphate in which the cerium metaphosphate in the sample more readily accepts added strontium than does the cerium orthophosphate, although a change in cerium orthophosphate line shape may indicate successful aliovalent substitution. No cerium metaphosphate is seen in samples prepared by the solid state synthesis route. In both cases, a separate chemical shift was seen that grows with higher addition of strontium to the material, suggesting that the addition of large amounts of strontium serve only to create an additional strontium-rich phase in the material.

3.6 Supporting Information: Results of Line Shape Analyses

Table 3.1: Summary of fitting parameters for peaks in the 0% $CePO_4$ Co-Precipitation Sample shown in Figure 3.4.

0% Sr $CePO_4$	**Chemical Shift**	**% Population**	**Linewidth**	**Shape**
Peak 1	26.8 ppm	17.4%	14.5 ppm	Gaussian
Peak 2	-83.6 ppm	29.1%	30.2 ppm	Gaussian
Peak 3	-95.5 ppm	53.5%	9.8 ppm	Gaussian

Table 3.2: Summary of fitting parameters for peaks in the 2.5% $CePO_4$ Co-Precipitation Sample shown in Figure 3.5.

2.5% Sr $CePO_4$	**Chemical Shift**	**% Population**	**Linewidth**	**Shape**
Peak 1	28.9 ppm	12.4%	16.6 ppm	Gaussian
Peak 2	-18.1 ppm	4.8%	15.9 ppm	Gaussian
Peak 3	-83.6 ppm	32.7%	30.3 ppm	Gaussian
Peak 4	-94.9 ppm	50.1%	11.3 ppm	Gaussian

Table 3.3: Summary of fitting parameters for peaks in the 5% $CePO_4$ Co-Precipitation Sample shown in Figure 3.6.

5% Sr $CePO_4$	**Chemical Shift**	**% Population**	**Linewidth**	**Shape**
Peak 1	27.5 ppm	10.5%	23.9 ppm	Gaussian
Peak 2	-22.9 ppm	1.2%	10.6 ppm	Gaussian
Peak 3	-83.6 ppm	29.5%	37.7 ppm	Gaussian
Peak 4	-94.4 ppm	58.8%	12.6 ppm	Gaussian

Table 3.4: Summary of fitting parameters for peaks in the 10% $CePO_4$ Co-Precipitation Sample shown in Figure 3.7.

10% Sr $CePO_4$	**Chemical Shift**	**% Population**	**Linewidth**	**Shape**
Peak 1	27.1 ppm	2.2%	23.0 ppm	Gaussian
Peak 2	-21.2 ppm	16.0%	22.0 ppm	Gaussian
Peak 3	-83.6 ppm	22.2%	34.1 ppm	Gaussian
Peak 4	-94.2.0 ppm	59.6%	13.1 ppm	Gaussian

Table 3.5: Summary of fitting parameters for peaks in the 2.5% $CePO_4$ Solid State Sample shown in Figure 3.10.

2.5% Sr $CePO_4$	**Chemical Shift**	**% Population**	**Linewidth**	**Shape**
Peak 1	-17.9 ppm	3.6%	21.7 ppm	Gaussian
Peak 2	-93.8 ppm	43.9%	13.9 ppm	Gaussian
Peak 3	-94.9 ppm	52.5%	27.4 ppm	Gaussian

Table 3.6: Summary of fitting parameters for peaks in the 5% $CePO_4$ Solid State Sample shown in Figure 3.11.

5% Sr $CePO_4$	**Chemical Shift**	**% Population**	**Linewidth**	**Shape**
Peak 1	-17.9 ppm	4.0%	22.3 ppm	Gaussian
Peak 2	-93.8 ppm	40.6%	13.1 ppm	Gaussian
Peak 3	-93.8 ppm	55.4%	25.9 ppm	Gaussian

Table 3.7: Summary of fitting parameters for peaks in the 10% $CePO_4$ Solid State Sample shown in Figure 3.12.

10% Sr $CePO_4$	**Chemical Shift**	**% Population**	**Linewidth**	**Shape**
Peak 1	-17.9 ppm	8.3%	17.9 ppm	Gaussian
Peak 2	-91.4 ppm	34.6%	14.3 ppm	Gaussian
Peak 3	-91.2 ppm	57.1%	26.4 ppm	Gaussian

Chapter 4

Proton conduction in (Ce,Sr) metaphosphate glass-ceramic composites

4.1 Acknowledgement

The author gratefully acknowledges the contributions of Hannah L. Ray, Dr. Ruigang Wang, Dr. Jian Feng, Professor Jeffrey A. Reimer, and Professor Lutgard C. De Jonghe to this work.

4.2 Abstract

An increase in conductivity of a (Ce,Sr)-metaphosphate glass-ceramic composite by more than two orders of magnitude in air has been observed through the synergistic effects of microstructural and compositional control during material synthesis, with particular attention to crystallization and aliovalent cation substitution. A detailed nuclear magnetic resonance study shows that the protons reside preferentially in the crystalline cerium-rich grains of this partially crystallized material.

4.3 Introduction

There is currently a lack of materials that function as proton conductors in the temperature range 300-550°C[1]. Of the many candidate materials for such proton conductors, alkaline doped rare-earth phosphate ceramics, glasses, and glass-ceramics have been investigated by several groups[21, 2, 3, 22, 6, 12, 13] because it is hypothesized that doping the trivalent rare earth phosphates with divalent cations will introduce protons as charge-compensating defects, increasing the carrier concentration and thus the conductivity of the compounds.

The family of rare earth phosphates possesses a range of compositional and structural possibilities (ultra-, meta-, pyro-, and ortho-) based on the oxygen to phosphorus (O/P) ratio, which can be used to tailor chemical and physical properties of these materials[23]. A study using first-principle calculations[14] suggested that intertetrahedral proton transfer in $LaPO_4$ (lanthanum orthophosphate) may be characterized by a low energy barrier, suggesting the examination of phosphates with long $(PO_4)^{3-}$ tetrahedra chains that may afford continuous proton conduction by intertetrahedral proton transfer. For example, in the rare earth metaphosphate (CeP_3O_9 or LaP_3O_9), the infinite $(PO_4)^{3-}$ tetrahedra (or -(PO_3)-) chain structure along 001 directions may be conducive to proton hopping via intertetrahedral PO_4 transfer. This is visualized in Figure 4.1(b) and 4.1(c) where the unit cells of $CePO_4$ (cerium orthophosphate) and CeP_3O_9 (cerium metaphosphate) are shown. The $(PO_4)^{3-}$ tetrahedra are all isolated in $CePO_4$, but are interconnected to form chains along the 001 direction in CeP_3O_9. Figure 4.1(a) depicts the 1 x 1 x 5 supercell of CeP_3O_9 along the 010 projection in which the $(PO_4)^{3-}$ chain in red can be more clearly identified.

In the present work we show that both crystallization of a bulk metaphosphate glass to a crystalline-metaphosphate composite and addition of aliovalent cations to bulk metaphosphate glasses increases conductivity as predicted. Surprisingly, these two approaches synergistically yield a higher proton conductivity improvement from either approach individually. The (Ce, Sr) metaphosphate glass and glass-ceramics synthesized possess both thermal stability and high proton conductivity. Furthermore, a single proton-hosting phosphate environment is found in the glass-ceramic material, indicating the importance of the crystallite presence and structure to the proton conductivity in these materials.

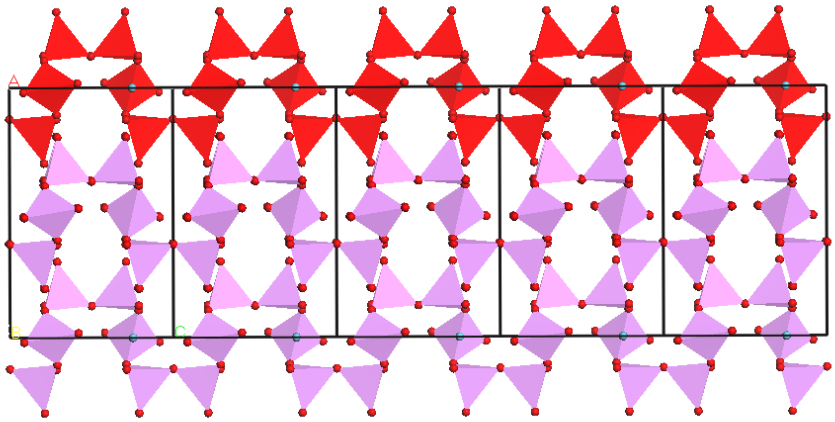
4.4 Experimental

4.4.1 Sample preparation

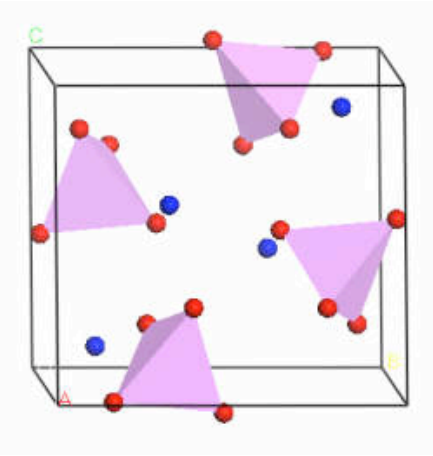
Samples were prepared by Hannah Ray in the Materials Science and Engineering department at UC Berkeley. Samples of nominal composition $Ce_{1-x}Sr_xP_3O_9$ in which x=0.0, 0.16, and 0.32 were prepared by melting the appropriate amounts of reagent-grade cerium oxide, strontium hydroxide hydrate, and 85% phosphoric acid in a platinum crucible at 1300C for 30 minutes, and then pouring the melt onto a steel plate preheated to approximately 350C. The glass was annealed at 450C for 2 hours, and then cut into wafers 1 cm in diameter x 0.5 mm in thickness using a slow speed diamond saw. To crystallize the glasses, the wafers were slowly heated in argon over a period of 3 hours to 700C and held at that temperature for 2 hours.

4.4.2 Open circuit voltage measurements

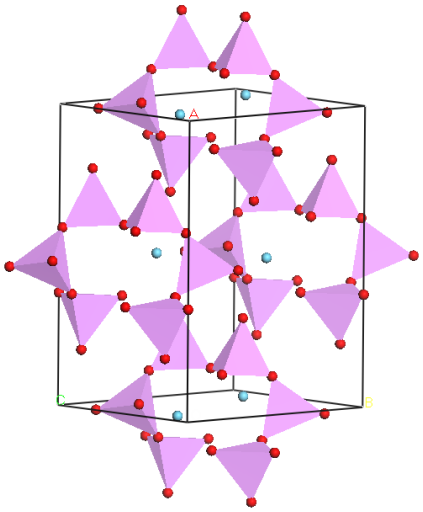
Open circuit voltage measurements were performed by Hannah Ray in the Materials Science and Engineering department at UC Berkeley. Glass and glass-ceramic samples were sliced into discs approximately 1 mm in thickness. Electrical contacts were formed by radiofrequency sputtering a layer of platinum onto the surface of the discs, and then attaching a platinum mesh to the layer using gold paste. For measurement of the open circuit voltage (OCV), each disc was bonded to a home-built test instrument using ceramic bond. One side of the disc was exposed to ambient



(a) The 1 x 1 x 5 super cell of CeP_3O_9



(b) The unit cell of $CePO_4$



(c) The unit cell of CeP_3O_9

Figure 4.1: The unit cell of $CePO_4$ (b) and CeP_3O_9 (c). The PO_4 tetrahedra (or -(PO_3)- chains) can be seen along the 010 projection in a 1 x 1 x 5 supercell of CeP_3O_9 (a).

air, and the other to hydrogen gas bubbled through water at room temperature. A Keithley 642 electrometer with a high impedance remote head was used to measure the electrochemical potential that developed across the disc. Measurements were carried out at 500°C.

4.4.3 Structural and chemical characterization

X-ray diffraction (XRD) measurements, electron micrographs, EDS studies, EDX studies, HAADF and TEM samples were performed by Ruigang Wang while at Lawrence Berkeley National Lab. X-ray diffraction (XRD) measurements were taken on a Philips PW3040 XPert Pro Diffractometer using Cu Kα (λ =1.54056) source operated with a 45keV X-ray tube voltage. Electron micrographs were obtained with an analytical scanning electron microscope (SEM, Zeiss Gemini Ultra-55) and a transmission electron microscope (TEM, JEOL 2100F) operated at 200kV, both equipped with energy dispersive X-ray spectroscope (EDS). The lateral distribution of elements by high angle annular dark-field (HAADF-STEM, also called Z-contrast) imaging and EDX mapping were acquired on JEOL 2100F with an annular dark-field detector and Oxford INCA EDX microanalysis system. In scanning mode (STEM mode), the 2.0 nanometer focused electron beam was stepped across the specimen for imaging and chemical analysis. HAADF imaging in STEM is a technique based on the theory that higher atomic number (Z) elements scatter electrons with higher angle than that of lower Z elements, thus providing contrast between heavier and lighter atoms [24]. The TEM plan-view samples were prepared by mechanical pre-thinning (Gatan dimple grinder) and then Ar ion milling (Fischione) with a liquid nitrogen cooling stage to eliminate the artifacts.

4.4.4 Conductivity measurement

Conductivity measurements were performed by Hannah Ray in the Materials Science and Engineering department at UC Berkeley. Platinum mesh electrodes were attached to the polished glass and glass-ceramic wafers using platinum paste. The wafers were about 1 cm in diameter and 0.5 mm thick. A Solartron 1260 impedance analyzer was used to measure the total conductivity of the samples. The frequency ranged from 10 MHz to 1 Hz, with alternating voltage amplitude of 800 mV_{p-p}. The temperature ranged from 325-600°C. Conductivity measurements were taken in air.

4.4.5 Nuclear Magnetic Resonance measurements

Variable temperature direct excitation ^{31}P MAS NMR spectra and direct excitation ^{1}H MAS NMR spectra were acquired at 1.54 T in a broadband single channel 4mm Doty Scientific XC probe using a Tecmag LapNMR spectrometer. Ammonium hydrogen phosphate was used as a secondary reference for ^{1}H and ^{31}P chemical shift values. All experiments were performed at approximately 10 kHz MAS and a Doty Scientific temperature controller was used to measure and control the temperature of the sample in the probe.

Room temperature ^{1}H -^{31}P cross polarization (CP)/MAS NMR spectroscopy[25] and heteronuclear correlation (HETCOR) spectroscopy[26, 27, 28] experiments were acquired at 7.05 T in

a triple channel 4mm Doty Scientific XC probe at 14kHz MAS using a Tecmag Apollo double channel spectrometer. Ammonium hydrogen phosphate was used as a secondary reference for ^{1}H and ^{31}P chemical shift values. A ^{1}H decoupling pulse of field strength 31.25 kHz was applied after the CP contact pulse through acquisition of the free induction decay. The two dimensional HETCOR data was processed using the Tecmag program NTNMR.

The ^{31}P -^{31}P 2D exchange NMR experiments were performed by Jian Feng in Reimer Group at UC Berkeley and Lawrence Berkeley National Laboratory. The ^{31}P -^{31}P 2D exchange NMR experiments were performed at 7.05 T in a triple channel 4mm Doty Scientific XC probe at 17 kHz MAS using a Tecmag Discovery spectrometer. Radio frequency dipolar-recoupling (RFDR)[29] used in combination with XY-8 phase cycling scheme[30] was applied during the mixing time of 2D chemical shift correlation spectroscopy experiments in order to recouple the ^{31}P -^{31}P homonuclear dipolar interaction diminished by fast magic angle spinning while minimizing the effect of pulse imperfection. No decoupling sequence was employed during the acquisition.

4.5 Results and discussion

4.5.1 Characterization of the (Ce,Sr) metaphosphate

The $Ce_{1-x}Sr_xP_3O_9$ as-melted glasses were light orange and transparent as synthesized, and became opaque and gray after heat-treatment. Figure 4.2 presents an XRD of the x=0, 0.16, and 0.32 $Ce_{1-x}Sr_xP_3O_9$ glass-ceramics after heat treatment at 700°C. The XRD patterns for the glass samples were featureless (not shown in Figure 4.2), characteristic of amorphous materials. The XRD pattern for the heat-treated samples show specimens to be nearly a single crystalline phase of CeP_3O_9 metaphosphate (JCPDS card 33-0336).

4.5.2 Effect of crystallization and aliovalent substitution on conductivity

The open circuit voltage (OCV) of each glass and glass-ceramic sample was measured. The theoretical OCV is predicted by summing the standard reduction potentials for the half reactions $H_2 = 2H^+ + 2e^-$, $E_0 = 0$ V, and $O_2 + 4H^+ + 4e^- = 2H_2O$, taken to be $E_0 = 1.23$ V, which becomes 1.15V after correcting for temperature (500°C). The OCV for all of the samples was statistically the same and was found to be 0.9 +/− 0.05 V. Because rare earth metaphosphate glasses and glass-ceramics of this type are known to incorporate protons upon aliovalent substitution[21, 6] and since the measured OCV is very close to the theoretical, it is assumed that the dominant charge carrier in these samples is protonic. The small negative deviation from the theoretical OCV could be attributed to leakage of H_2 gas through the ceramic bond, a small contribution of electronic carriers to the total conductivity or a voltage drop due to irreversible electrode processes.

4.5.3 Crystallization and aliovalent substitution effect on conductivity

Figure 4.3 shows the temperature dependant conductivity results for both the glasses and recrystallized glass ceramics. It is noteworthy that the proton conductivity increases by an order of magnitude when the (x = 0) CeP_3O_9 glass sample is recrystallized. While the addition of strontium

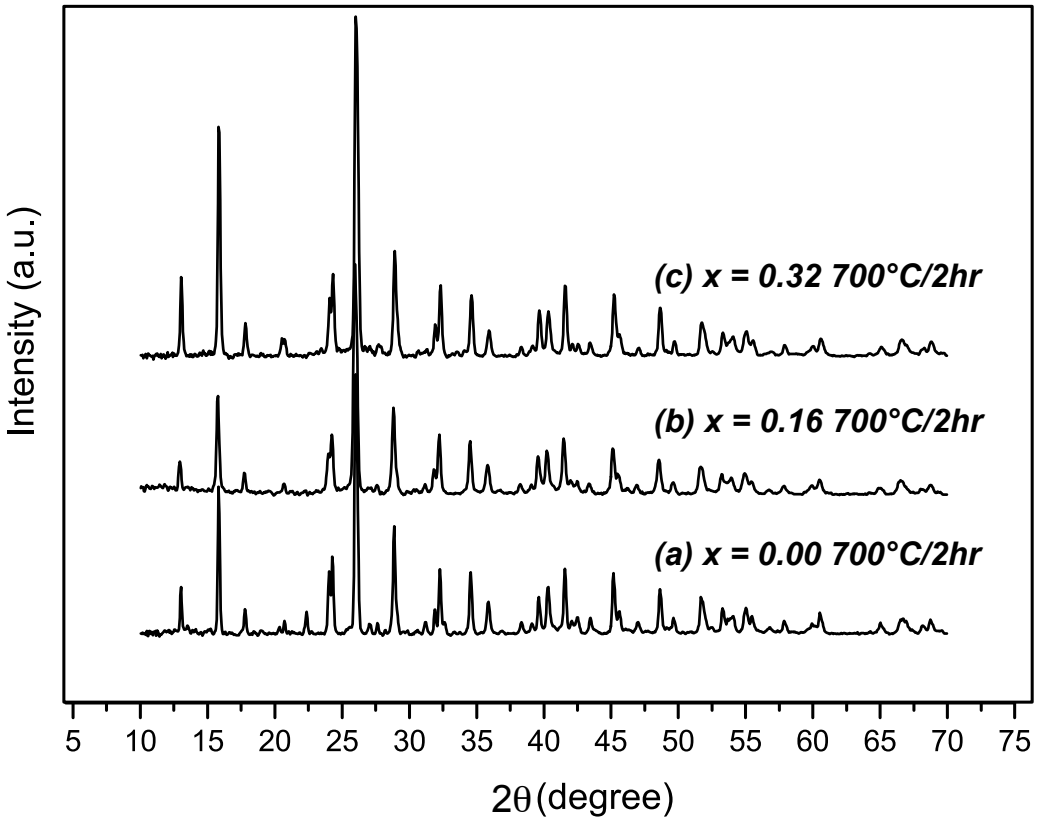


Figure 4.2: XRD patterns for the x = 0, 0.16, and 0.32 $Ce_{1-x}Sr_xP_3O_9$ glass-ceramic materials heat-treated at 700°C.

to glass metaphosphate improves the conductivity only modestly (in the case of the materials investigated here, roughly a factor of two), another order of magnitude increase in conductivity is seen when one compares the recrystallized (Ce, Sr) metaphosphates to the pure cerium metaphosphate, resulting in a total improvement of two orders of magnitude in the conductivity of the glass-ceramic (Ce, Sr) metaphosphates as compared to the glass metaphosphates. This conductivity, which the OCV indicates is primarily protonic, is nearly $10^{-4.2}$ S/cm at 430°C in air, which is much higher than protonic conductivity in $CePO_4$ orthophosphate[31], and is in agreement with the hypothesis that metaphosphate has higher conductivity than orthophosphate due to the lower barrier energy for proton hopping mechanism or stronger trapping effect in orthophosphate[32]. This conductivity is higher than that of reported (La,Ca)-metaphosphate proton conductors prepared by a similar procedure[6]. The activation energies calculated from the conductivity data are presented in Table 4.1. It is seen that the glass samples, in general, have higher activation energies than the glass-ceramic samples. It is worth noting that the differences in activation energies seen among the glass samples are not statistically significant; likewise, the much smaller differences in activation energies seen among the glass-ceramic samples also are too small to be statistically significant.

Table 4.1: Activation energies calculated from conductivity measurements for the glass and glass-ceramic $Ce_{1-x}Sr_xP_3O_9$ materials. These values were calculated using Arrhenius fits to the conductivity data presented in Figure 4.3.

Sample	**Activation Energy (eV)**
CeP_3O_9 Glass	1.15
$Sr_0.16Ce_0.84P_3O_9$ Glass	0.98
$Sr_0.32Ce_0.68P_3O_9$ Glass	1.02
CeP_3O_9 Glass-Ceramic	0.75
$Sr_0.16Ce_0.84P_3O_9$ Glass-Ceramic	0.73
$Sr_0.32Ce_0.68P_3O_9$ Glass-Ceramic	0.76

4.5.4 Identification of proton-hosting sites

Definitive structural analysis of metaphosphates is nearly impossible with TEM due to rapid electron beam damage, thus TEM chemical analysis was used to gain further insights on these samples. Figure 4.4(a) shows the typical high-angle annual dark field (HAADF, also called Z-contrast) scanning transmission electron microscopy (STEM) images and corresponding EDX spectra of the 700°C heat-treated $Ce_{0.84}Sr_{0.16}P_3O_9$ specimen. The Z-contrast images, in Figure 4.4(b) and 4.4(c), reveals two different domains. Based on the principle of Z-contrast imaging (higher atomic number, stronger intensity)[24], it is clearly seen that the crystallized phase is Ce-rich and the glass phase is Sr-rich. This was confirmed by the correlated EDX elemental analysis of Ce and Sr, shown in Figure 4.5(b) and 4.5(c) through both the glass and crystal regions, where the Cliff-Lorimer ratio method[33] was used to quantify the concentration of each element. Elemental mappings of O and P were also obtained and exhibit homogeneous distribution (not shown here).

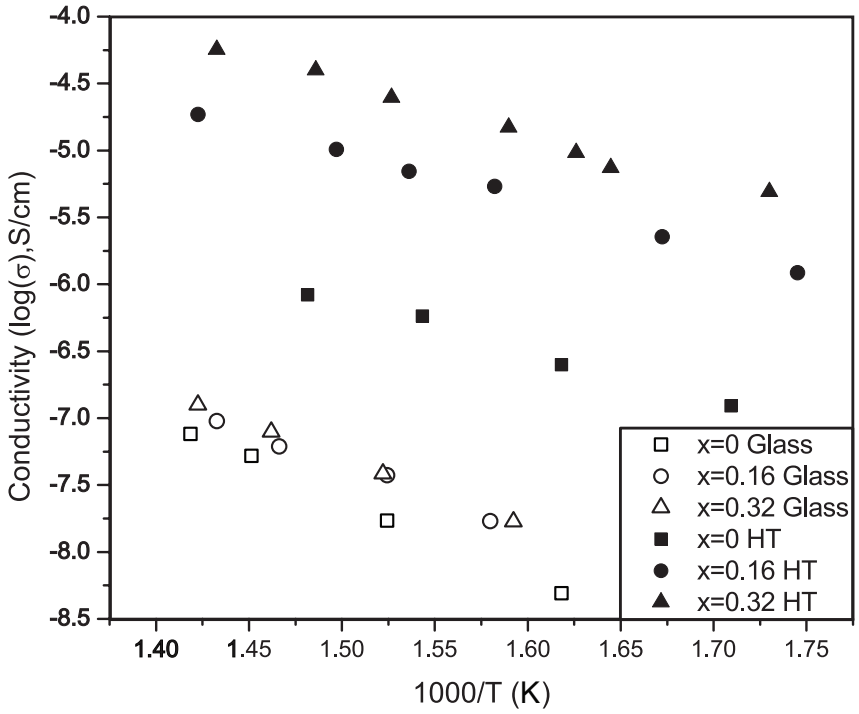


Figure 4.3: AC conductivity of the $Ce_{1-x}Sr_xP_3O_9$ glass and glass-ceramic materials with respect to inverse temperature. The highest conductivity is observed for the $Ce_{0.68}Sr_{0.32}P_3O_9$ material.

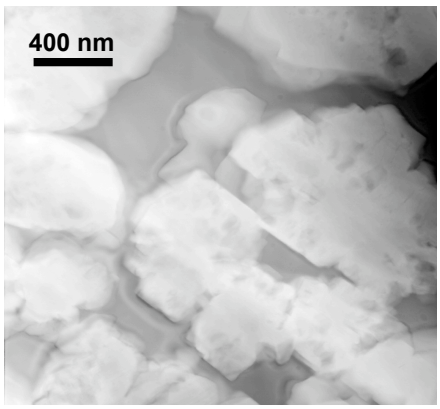
With a focused electron beam (2 nm) in STEM mode, the local chemical composition using EDX point measurement (square areas in Figure 4.5(a)) from the glass and crystallized phases in both of samples were obtained, shown in Figure 5 4.5(b) and 4.5(c). In general, the spectrum from the glass matrix shows a high content of Sr, P, and O, and a small amount of Ce is also present. In contrast, the spectrum from the area containing crystallites presents a dominant Ce, P, and O concentration. Combined with the results of XRD, it is concluded that Ce ions are mainly concentrated in the crystallites.

The Ce ions were determined to be in the +3 oxidation state using Ce $M_{4,5}$ edge intensity ratios in the electron energy loss spectrum (EELS)[34]. In the Ce-rich phase, the M_5:M_4 area ratio is 0.82 and the M_5:M_4 branching ratio is 0.54, which are both in the range expected for materials containing only Ce^{3+}. In the Sr-rich glass phase, the M_5:M_4 area ratio is 0.86 and the M_5:M_4 branching ratio is 0.52, which in the range expected for materials containing only Ce^{3+} using the M_5:M_4 area ratio but the branching ratio value lies in between the those reported for materials containing only Ce^{3+} and those containing both Ce^{3+} and Ce^{4+}. It is therefore concluded that the cerium present in the Ce-rich crystalline phase is exclusively Ce^{3+}, while that cerium in the Sr-rich phase could be a mixture of Ce^{3+} and Ce^{4+}.

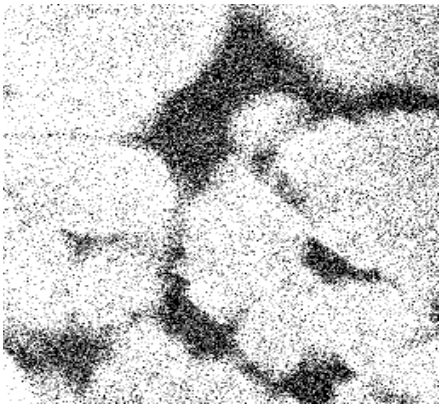
The composition (atomic percentage) of the starting materials was selected as $21CeO_2$-$4Sr(OH)_2$-$75H_3PO_4$ (Ce: Sr: P=21: 4: 75) to obtain a metaphosphate glass (total atomic ratio of cation to phosphorus P=1:3). However, the EDX analysis from a larger spatial region in a low magnification image mode reveals a composition of Ce:Sr:P=19:4:72, which is slightly different from the expected values. The SEM EDX spectrum analysis shows a similar composition result, but provides an analysis of much larger region (mm scale) and better statistical analysis (analysis accuracy is limited to about 5%). Possible explanations of this difference could be compositional variation in the sample or P loss during glass preparation and heat treatment since P_2O_5 volatilization is well known problem in the preparation of phosphate glasses at high temperature[35]. While EDX point measurements in both sample domains revealed dominant Ce (e.g. in Figure 4.5, Ce: Sr=91.0:9.0) and Sr (Sr: Ce=70.5:29.5) in the crystallite and glass phases, respectively, it is also clear that the Ce-rich crystallite and Sr-rich glass phases still contain small amounts of Sr and Ce, respectively.

^{31}P MAS NMR Variable Temperature Studies

Direct excitation ^{31}P NMR yields the chemical bond environments of polyphosphate compounds, as established on the basis of the ^{31}P chemical shift[36]. All other things being equal, increasing connectivity of the phosphate groups causes the ^{31}P chemical shift to move to increasingly negative ppm values. Figure 4.6 shows the results of direct excitation (90-acquire) ^{31}P MAS NMR experiments performed at 20°C on the $Ce_{0.84}Sr_{0.16}P_3O_9$ sample. Unpaired electrons often interact with neighboring nuclei producing dramatic effects on the NMR spectrum of the proximate nuclei. The Ce^{3+} ions in cerium phosphate (configuration [Xe]5d1) contain an unpaired electron which can interact with neighboring nuclei. Previous studies have shown Ce^{3+} in cerium phosphates to be paramagnetic[37, 38], and the paramagnetic interaction between the unpaired electron and the ^{31}P nuclei results in dramatically shortened relaxation times, line width broadening, and chemical shifts that depend on sample temperature, often resulting in chemical shifts at room temperature that are very different than those expected for rare earth phosphates. Although this paramagnetic behavior often complicates analysis of NMR spectra, it can also provide insight into the proximity of nucleus in question to the paramagnetic moiety.



(a) Z-contrast of the sample.

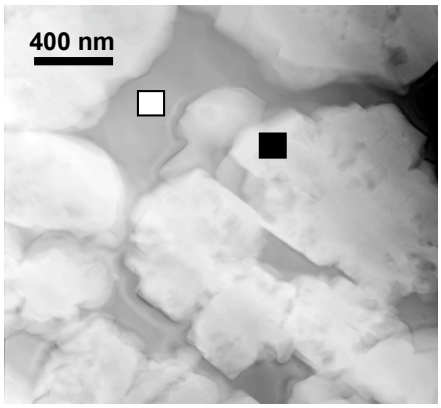


(b) Ce mapping of the Z-contrast image.

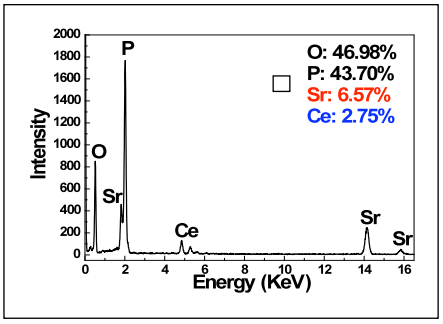


(c) Sr mapping of the Z-contrast image.

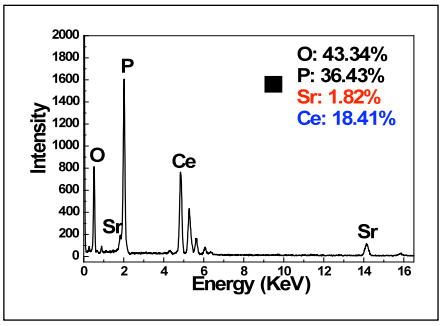
Figure 4.4: Z-contrast images for the $Sr_{0.16}Ce_{0.84}P_3O_9$ glass-ceramic material. In (a), the Z-contrast imaging of the sample is shown. Figures (b) and (c) display the Ce and Sr mapping, respectively, and demonstrate qualitatively that the Ce is present predominantly in the grains and the Sr is present predominantly in the intergranular regions.



(a) Z-contrast of the sample



(b) EDX of the intergranular region (black box)



(c) EDX of the crystalline region (white box)

Figure 4.5: EDX composition analysis for the $Sr_{0.16}Ce_{0.84}P_3O_9$ glass-ceramic material. Figure (a) displays the Z-contrast imagining with two boxes indicating where the EDX composition was done. The black box shows the location of the EDX of the intergranular region (b) and the white box shows the EDX of the crystalline grains (c).

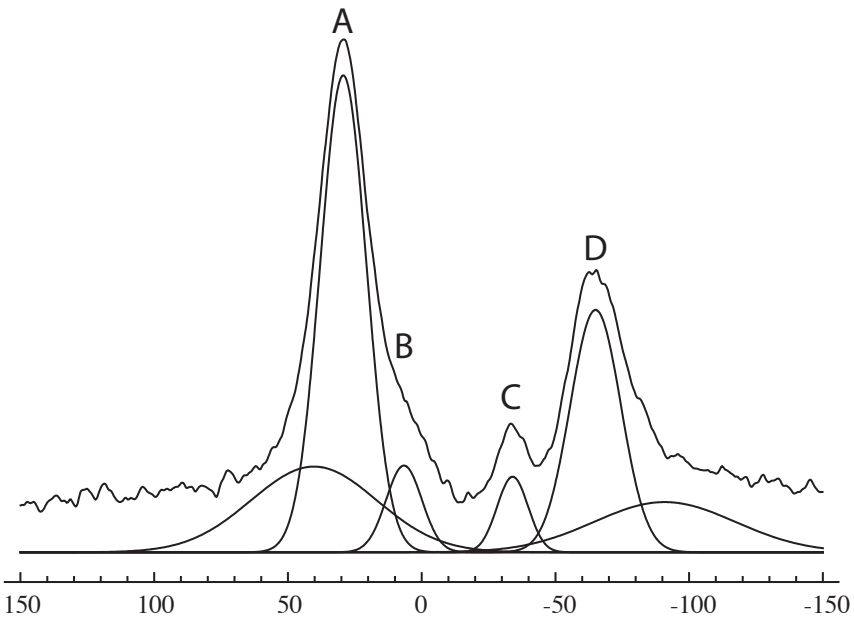


Figure 4.6: Direct excitation ^{31}P MAS NMR of the $Sr_{0.16}Ce_{0.84}P_3O_9$ glass-ceramic material at 25.6 MHz, 11kHz MAS speed and 20°C.

A line shape analysis was performed to deconvolute the NMR spectrum and allow assignment and identification of resonances specific to phosphate environments within the material. The ^{31}P NMR data was fit using a nonlinear fit algorithm in Mathematica that fit multiple Gaussian line shapes to the data. Table 4.2 shows the peak centers (isotropic chemical shifts) of each of the peaks in the $Ce_{0.84}Sr_{0.16}P_3O_9$ sample at 20°C. Chemical shifts assignments were assigned with the help of literature studies[36] and additional variable temperature NMR line shape analyses. To simplify subsequent discussion of the ^{31}P MAS NMR chemical shift spectrum, the different ^{31}P environments will be grouped into four environments for discussion: the peaks at 38.5 ppm and 27.5 ppm (A), the peak at 4.8 ppm (B), the peak at -35.8 ppm (C), and the peaks at -66.8 and -92.6 ppm (D), as indicated in Table 4.2 and Figure 4.6.

Table 4.2: Chemical shift and spin-lattice relaxation (T_1) data for direct excitation ^{31}P MAS NMR study of the $Sr_{0.16}Ce_{0.84}P_3O_9$ sample at 20°C at 26.6 MHz. The phosphate environments are grouped A-D as described in the text

Group	**Chemical Shift 20°C**	**T_1 at 20°C**	**Assignment**
	(ppm)	(s)	
A	38.5	0.030 +/- 0.016	Disordered cerium metaphosphate
A	27.5	0.031 +/- 0.004	Crystalline cerium metaphosphate
B	4.8	0.027 +/- 0.012	P-O-H metaphosphate
C	-35.8	6 +/- 9	Sr-rich Region
C	-35.8	110 +/- 150	Sr-rich Region
D	-66.8	0.011 +/- 0.002	Crystalline cerium metaphosphate
D	-92.6	0.012 +/- 0.006	Disordered cerium metaphosphate

Direct excitation ^{31}P MAS NMR were performed at 20°C, 40°C, 60°C, and 80°C to probe the temperature dependence of the chemical shift values measured by the line shape analysis. Table 4.3 shows the results of the line shape analysis at each temperature. All peaks except for that at -35.8 ppm (C) change significantly over this temperature range. Infinite temperature chemical shifts are given in Table 4.4 and demonstrated in Figure 4.7. Such behavior is consistent with nuclei experiencing contact shifts from electrons characterized by Curie-Weiss paramagnetic behavior, as seen in ^{7}Li and ^{1}7O studies of oxides[39, 40], and is indicative of proximity to Ce^{3+}. The peak at -35.8 ppm does not change over the temperature range probed here, suggesting these phosphorus nuclei are not proximate to Ce^{3+}.

Because there is no reference chemical shift value(s) for CeP_3O_9 in the literature, a direct excitation (90-acquire) ^{31}P MAS NMR experiment performed at 20°C on the strontium-free (CeP_3O_9) sample for use as a standard in Figure 4.8. The same peaks (A) and (D) that are seen in the strontium-containing sample at 20°C are present in the cerium metaphosphate sample, and so peaks A and D in the strontium-containing sample will be attributed to cerium metaphosphate.

A ^{31}P MAS saturation recovery experiment was performed at 20°C on the $Ce_{0.84}Sr_{0.16}P_3O_9$ sample. A nonlinear fit algorithm in Mathematica was used to fit a mono-exponential decay to each peak found in the line shape analysis the exception being the peak at -35.8 ppm, which was

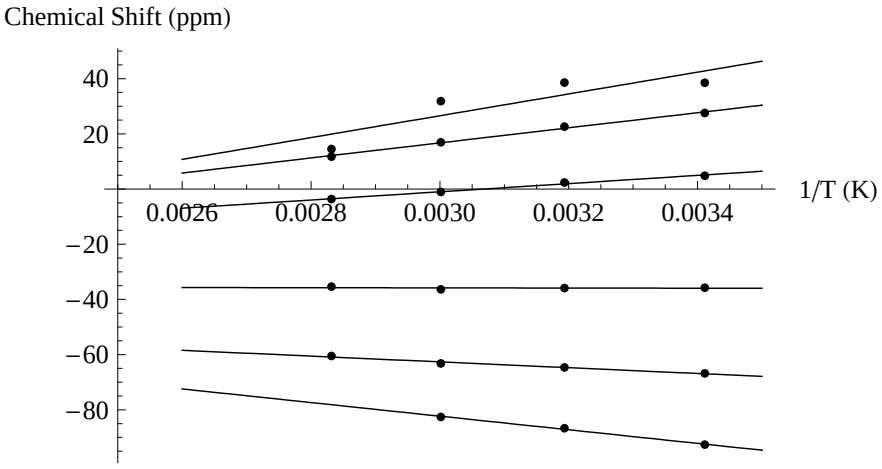


Figure 4.7: Infinite temperature extrapolation of ^{31}P MAS NMR chemical shifts of the $Sr_{0.16}Ce_{0.84}P_3O_9$ glass-ceramic.

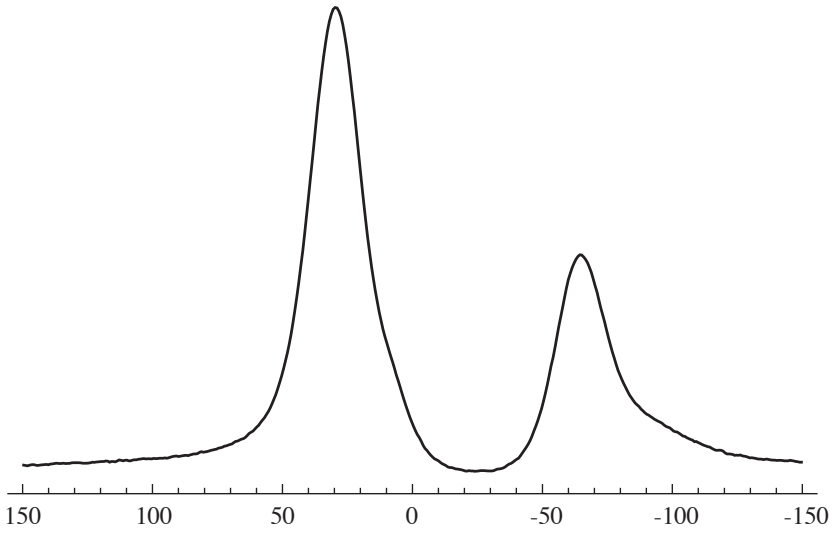


Figure 4.8: Direct excitation ^{31}P MAS NMR of the CeP_3O_9 glass-ceramic material at 25.6 MHz, 11kHz MAS speed and 20°C.

Table 4.3: Chemical shift data for direct excitation ^{31}P MAS NMR study of the $Sr_{0.16}Ce_{0.84}P_3O_9$ sample at 20°C, 40°C, 60°C and 80°C at 26.6 MHz. The phosphate environments are grouped A-D as described in the text

Group	**Chemical Shift 20°C**	**CS 40°C**	**CS 60°C**	**CS 80°C**
	(ppm)	(ppm)	(ppm)	(ppm)
A	38.5	38.6	31.9	14.5
A	27.5	22.6	17.0	11.8
B	4.8	2.4	-1.1	-3.6
C	-35.8	-35.9	-36.3	-35.4
D	-66.8	-64.7	-63.2	-60.5
D	-92.6	-86.6	-82.5	-58.3

Table 4.4: Infinite temperature extrapolations of chemical shift data for direct excitation ^{31}P MAS NMR study of the $Sr_{0.16}Ce_{0.84}P_3O_9$ sample at 20°C, 40°C, 60°C and 80°C at 26.6 MHz. The phosphate environments are grouped A-D as described in the text

Group	**Chemical Shift 20°C**	**CS Infinite Temperature**
	(ppm)	(ppm)
A	38.5	-92.0
A	27.5	-65.2
B	4.8	-45.6
C	-35.8	-34.0
D	-66.8	-31.2
D	-92.6	-8.3

better fit by a bi-exponential function, resulting in two T_1s for this region. The results of this T_1 study is also are given in Table 4.2. As can be seen, the two T_1s of the peak centered at -35.8 are more than three orders of magnitude longer than all other T_1s. It should be noted that the shorter T_1s are on the same order of magnitude of those measured for cerium orthophosphate[37] and are consistent with the presence of paramagnetic ions, indicating that these peaks result from phosphorus nuclei proximate to Ce^{3+}. These relaxation analyses, therefore, further indicate that the peak at -35.8 ppm is not is not proximate to Ce^{3+}.

^{1}H MAS NMR Studies

Figure 4.9 shows the result of direct excitation ^{1}H MAS NMR on the $Sr_{0.16}Ce_{0.84}P_3O_9$ sample at 20°C with sample spinning at approximately 11 kHz. The spectrum consists of a single, broad Gaussian peak without further distinguishing features. Because the peak is so broad, we are unable to easily assign the peak to any one resonance. Because the ^{1}H NMR signal is very weak in this and other cerium phosphate materials, it is possible that water could make up some part of this ^{1}H NMR spectrum. To confirm that the protons seen here are present in the phosphate sample

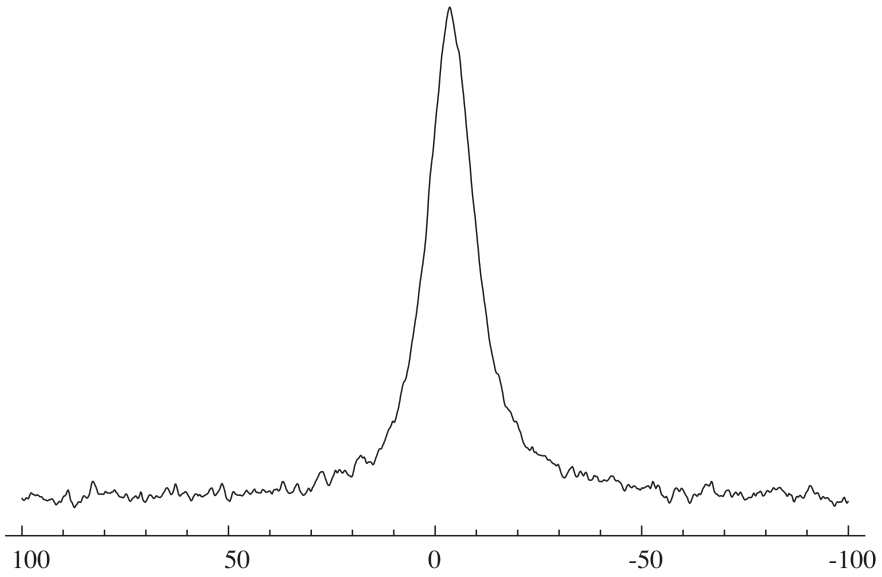


Figure 4.9: Direct excitation ^{1}H MAS NMR of the $Sr_{0.16}Ce_{0.84}P_3O_9$ glass-ceramic material at 25.6 MHz, 11kHz MAS speed and 20°C.

and to determine relationship with the material structure, multinuclear NMR techniques are used.

^{1}H -^{31}P CPMAS and ^{1}H -^{31}P HETCOR Studies

Figure 4.10 shows the comparison between a direct excitation ^{31}P MAS NMR spectrum and a ^{1}H -^{31}P CPMAS NMR spectrum of the $Sr_{0.16}Ce_{0.84}P_3O_9$ sample, both taken at 7.05 T and 14 kHz MAS. Because phosphorus NMR spin-lattice relaxations are so short in this system, a direct-excitation suppression phase cycling is used to ensure that no directly excited ^{31}P signal is present. Additionally, the CPMAS experiment was repeated with the proton channel turned off during the cross polarization step to ensure proper function of the direct excitation suppression; no signal was seen. The single phosphorus resonance seen in the CPMAS spectrum corresponds to peak B (4.8 ppm) in the ^{31}P line shape analysis at 20°C described previously. This suggests that this peak in the phosphorus NMR spectrum corresponds to a phosphate group with a P-O-H bond.

Figure 4.11 shows the two-dimensional ^{1}H -^{31}P CP HETCOR MAS NMR spectrum of the $Ce_{0.84}Sr_{0.16}P_3O_9$ sample with vertical and horizontal projections of the two-dimensional spectrum. The spectrum indicates the presence of a single dipolar-coupled ^{1}H -^{31}P system. The ^{31}P environment is the same that was observed in the ^{1}H -^{31}P CPMAS described above. The ^{1}H environment is centered at roughly -15 ppm (thus is likely paramagnetically shifted) and is of a peak width expected for a P-O-H proton. It is hypothesized that this is the mobile proton in this proton-conducting material.

Table 4.2 gives a summary of the ^{31}P isotropic chemical shifts of the material under investigation, identified by their respective isotropic chemical shifts at 20°C. Two of the peak regions (A and D) are identified by their similarity to a strontium-free cerium metaphosphate sample. The variable temperature and spin-lattice relaxation analysis of the spectrum suggest that

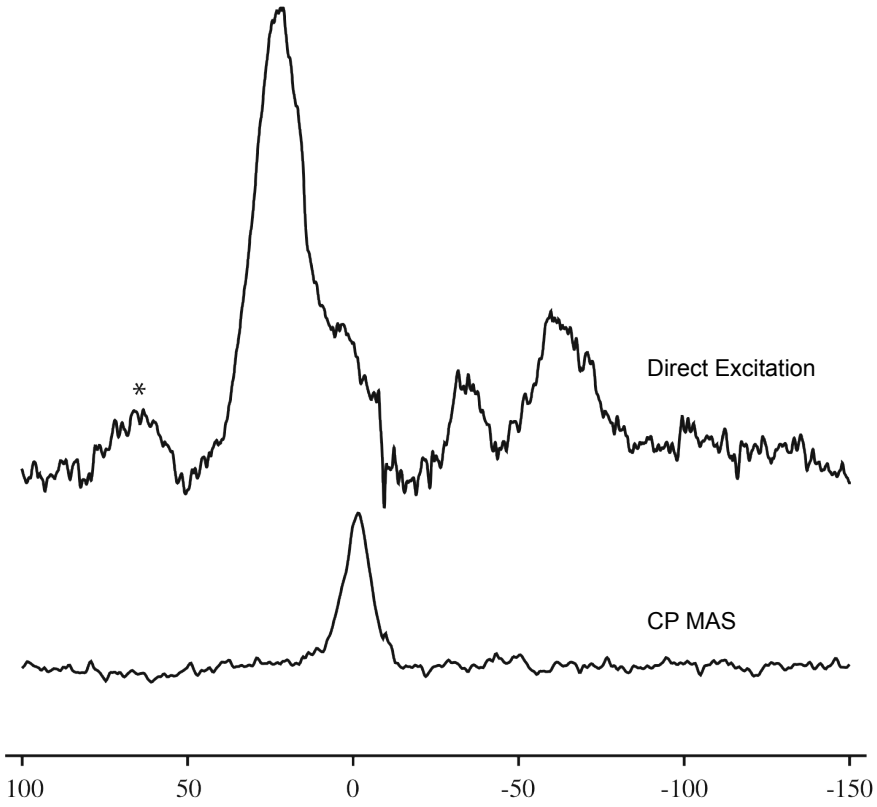


Figure 4.10: Comparison of direct excitation ^{31}P MAS NMR and ^{1}H -^{31}P CPMAS NMR spectra of $Sr_{0.16}Ce_{0.84}P_3O_9$ glass-ceramic sample taken at 121.4 MHz, 14 kHz MAS and 20°C. The only resonance present in the CP MAS spectrum corresponds to peak B.

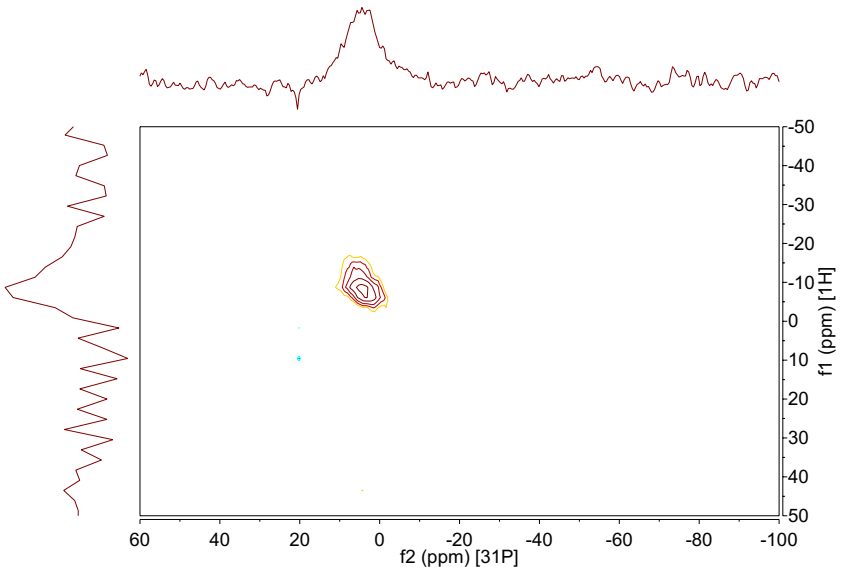


Figure 4.11: Two-dimensional ^{1}H -^{31}P ramp CP HETCOR study at 7.05 T, 14 kHz MAS and 20°C. A single cross peak is shown at the resonance corresponding to peak B in the ^{31}P MAS NMR spectrum and the peak observed in the ^{1}H MAS NMR spectrum (Figure 4.9).

peak C (-35.8 ppm) is a low concentration Ce^{3+} phosphate environment in this material, and likely corresponds to the Sr-rich region observed in the TEM and EDX study. Peak B (4.8 ppm) is a P-O-H phosphate environment and likely corresponds to the Ce-rich crystalline region described in the TEM study, as suggested by the variable temperature and spin-lattice relaxation analysis of the ^{31}P NMR spectrum. As the ^{1}H -^{31}P CPMAS and ^{1}H -^{31}P HETCOR studies illustrate, this Ce-rich region hosts the only P-O-H protons observed in the material, and is likely responsible for proton conduction.

^{31}P -^{31}P Exchange Studies

^{31}P -^{31}P 2D exchange NMR spectra were obtained to determine the spatial proximity between phosphorus sites with distinct chemical shifts and to provide further insight into the structural features of the $Ce_{0.84}Sr_{0.16}P_3O_9$ sample. The diagonal components of the 2D contour plot (Figure 10), contain chemical shift information, of which the projection patterns on both dimensions are qualitatively identical to the ^{31}P direct excitation MAS NMR spectra in terms of peak positions. Off-diagonal resonances correlate the diagonal peaks arising from phosphate tetrahedra in close proximity, typically on the order of 0.1-0.5 nanometers. The build-up rate for the off-diagonal correlation peaks depends directly on the corresponding ^{31}P -^{31}P distance, with shorter distances yielding a faster build-up of cross peaks. Figure 4.12 shows the ^{31}P -^{31}P 2D exchange NMR spectrum acquired with 5.5 ms mixing time, which contains strong cross peaks for diagonal signals projected at peaks A and D, and relatively weak cross peaks for signals projected at peak A and B, indicating these three ^{31}P resonances are proximate. ^{31}P -^{31}P 2D exchange NMR

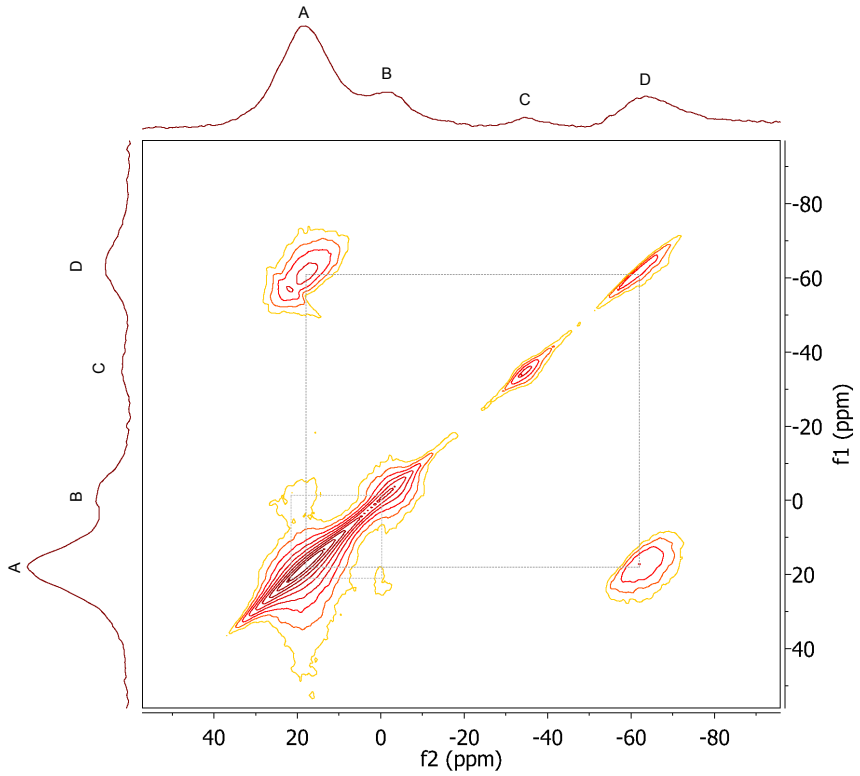


Figure 4.12: ^{31}P -^{31}P 2D exchange NMR spectrum obtained with 5.5 ms mixing time, during which RFDR recoupling sequence was applied. Dotted lines denote the correlation between diagonal and cross peaks for clarity.

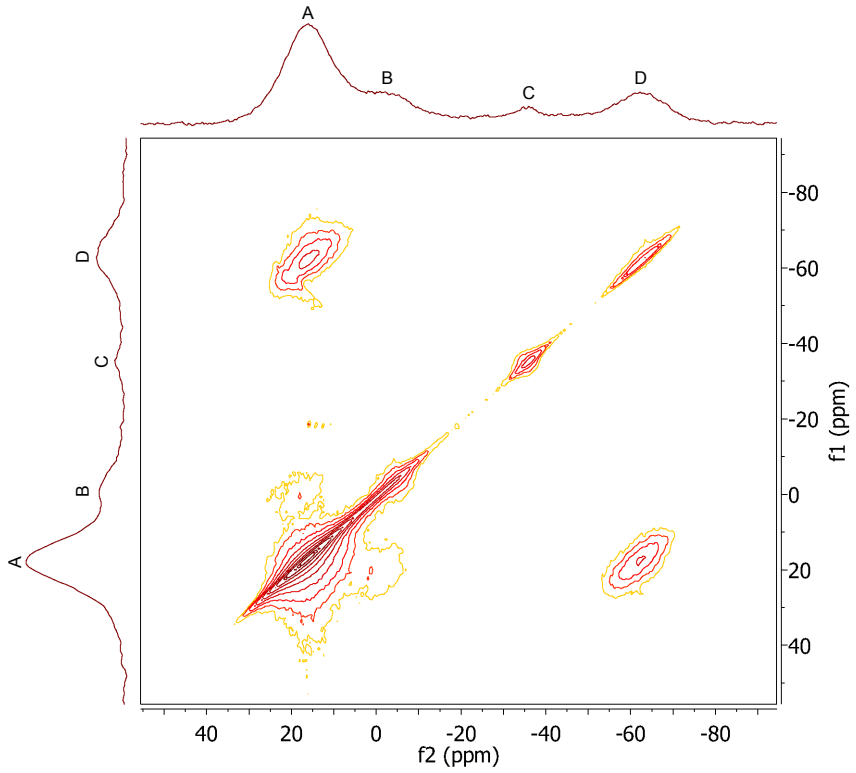


Figure 4.13: ^{31}P -^{31}P 2D exchange NMR spectrum obtained with 8.4 ms mixing time, during which RFDR recoupling sequence was applied.

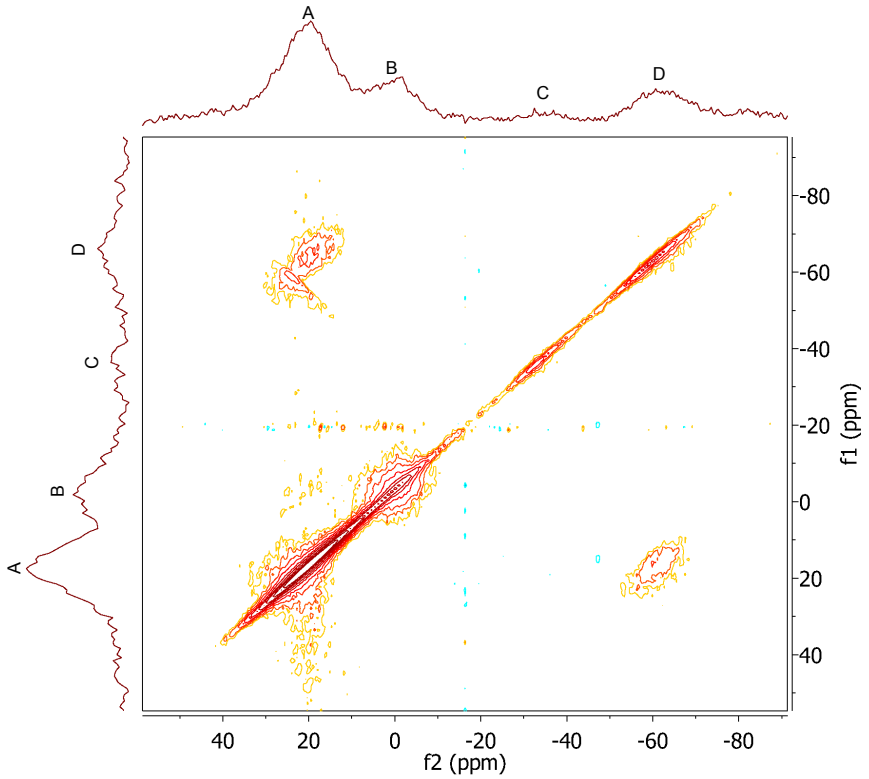


Figure 4.14: ^{31}P -^{31}P 2D exchange NMR spectrum obtained with 2.8 ms mixing time, during which RFDR recoupling sequence was applied.

spectra with longer mixing time (up to 8.4 ms in Figure 4.13) were also obtained, but the 2D spectral patterns show no substantial difference from that acquired with 5.5 ms mixing time (Fig. 4.12), and no cross peak was observed at any mixing time for the diagonal signal assigned to the phosphates in the Sr-rich phase (peak C). Comparison with the 2D exchange NMR spectra at short mixing time (e.g., τ mix = 2.8 ms in Figure 4.14) shows that the self-correlation signals for the P-O-H group (i.e. shoulders around diagonal of the peak projected to B) build up faster than the correlation between peaks A and B, suggesting clustering of the P-O-H groups. Because ^{31}P NMR peaks A and D are present in Ce-rich phase of the $Ce_{0.84}Sr_{0.16}P_3O_9$ sample as demonstrated previously, the result that peaks A and B are spatially proximate reaffirms that the proton-hosting phosphate (Peak B) is in the crystalline phase.

4.6 Conclusions

$Ce_{1-x}Sr_xP_3O_9$ glass-ceramic proton conductors were synthesized via crystallization of glass samples. After the crystallization, the total proton conductivity of the crystallized sample is nearly $10^{-4.2}$ $Scm^{-}1$ at 430°C in air, having increased by over two orders of magnitude when compared to the glass and cerium orthophosphate samples in a similar environment. This improvement results from the synergistic effect of crystallization and aliovalent cation introduction. TEM and EDX chemical characterization revealed that the crystallized domains are mainly CeP_3O_9, while the glass network is composed of Sr-rich phosphate. NMR studies indicate the proton-hosting sites are exclusively in the Ce-rich crystalline phase of the material. The presence of Sr ions in the crystallized CeP_3O_9 phase (as observed by EDX analysis and Z-contrast imaging) provides evidence of successful aliovalent Sr^2+ substitution. The inclusion of these Sr^2+ ions and the presence of proton-hosting sites exclusively in the Ce-rich crystallized phase provide strong evidence for negative defect sites (Sr_{Ce}), which accommodate the mobile positive protons and are beneficial to proton conduction an observation may be confirmed by future double resonance ^{1}H -^{87}Sr NMR studies. However, it is also clear that crystallization results in a significant phase separation of Ce-rich domain with Sr-rich matrix. The richness of variables in controlling compositional and structural order, as well as aliovalent substitution for enhancing proton content, portends further improvements in proton conductivity.

Chapter 5

Self Diffusion

5.1 Acknowledgement

The author gratefully acknowledges the contributions of Dr. Gabriel Harley, a material science researcher in the group of Professor Lutgard De Jonghe at Lawrence Berkeley National Laboratory, to this work.

5.2 Introduction

The stochastic phenomena that relax nuclear magnetic resonance signals are often correlated to macroscopic transport processes, such as diffusion, and can be studied by a range of relaxation, field gradient and imaging techniques to yield useful dynamic information. In the case of the materials being studied, the self-diffusion of protons in the proposed proton conducting membrane is of interest in order to better understand the dynamics of proton movement through the material. Furthermore, the activation energy of this self-diffusion process is of interest in light of theoretical work that has been done to predict how protons move from phosphate group to phosphate group[14], and is useful as a comparison to activation energies determined from AC impedance spectroscopy measurements.

In this work, field gradient NMR diffusometry techniques are adapted to measure the self diffusion coefficients of protons in rare earth phosphate materials.

5.3 Theory

Field gradient NMR diffusometry is the primary NMR method used to measure self-diffusion. These field gradients can be made in either the main magnetic field, B_0, or in the applied magnetic field, B_1. Furthermore, methods can employ either a pulsed or a time independent gradient (also referred to as a "steady gradient"). There is a wealth of literature on the subject of field gradient NMR diffusometry studies[4, 41].

Diffusion experiments of this sort are usually discussed in terms of spin echos, the amplitude of which is attenuated by the translational displacement of the spin-bearing moieties in the

course of the pulse sequence[45]. In these experiments, coherences are first dephased by field gradients and then rephased in the form of a Hahn or stimulated echo. Displacements in the presence of field gradients prevent the superposition of coherences, entirely constructive at the time when the spin echo is to appear, so that the echo amplitude is irreversibly reduced. If the diffusion behavior can be described mathematically (and if the solution is possible), the diffusion behavior can be characterized through a series of experiments that observes how the echo amplitude decays as the effect of diffusion is allowed to dominate the echo.

Diffusion behavior is usually described by a diffusion propagator, which characterizes such translational displacements of distance **r** during an interval t through the use of a probability density function, p(**r**,t), which gives the probability that a particle is found in the region x to x+dx, y to y+dy, and z to z+dz during this interval. For ordinary, isotropic diffusion, this diffusion propagator obeys the diffusion equation

$$\frac{\delta p}{\delta t} = D\nabla^2 p$$

where ∇ is the Laplace operator, usually expressed in Cartesian coordinates for these experiments. For the case of ordinary isotropic unrestricted diffusion, the self diffusion coefficient is a scalar quantity and with the additional assumptions that the material itself is isotropic and homogeneous, the solution to the above equation can be shown[4] to be the normalized Gaussian function

$$p(r,t) = \frac{1}{(4\pi Dt)^{\frac{\psi}{2}}} Exp(-\frac{r^2}{4Dt})$$

where $\psi = 1, 2, 3$ is the dimensionality of the Euclidian space. This distribution function depends solely on the net displacement of the particle during time period t, and not on the initial position. Although isotropic unrestricted diffusion will take place in three dimensions, it is important to note that such measurements generally take place only in one dimension for practical purposes described later. Under these conditions, the width of the displacement distribution function is described by the second moment, which is the mean squared displacement

$$< r^2(t) >= \int_{-\infty}^{\infty}\int_{-\infty}^{\infty}\int_{-\infty}^{\infty}(x^2+y^2+z^2)p(r,t)dxdydz = 6Dt$$

Deviations from Gaussian distribution functions occur when one of the above constraints are violated (e.g., if the diffusion is not ordinary, unrestricted and isotropic or if the material is not homogeneous, which is common) or if the translational displacements are restricted by geometrical constraints. This is generally referred to as *anomalous diffusion* in which the mean squared displacement follows a power law[4]

$$< r^2(t) >= \alpha t^{\kappa}$$

Ordinary unrestricted diffusion is described by $\kappa = 1$ and $\alpha = 2\psi D$. Subdiffusive behavior is characterized by κ given by $0 < \kappa < 1$ and is used to describe diffusion on random-percolation clusters[4]. Superdiffusive behavior is characterized by $\kappa > 1$. Such anomalous diffusion can be

used to determine the distribution function that is then used to model the results of a self diffusion experiment.

Although one never needs to know the diffusion propagator in order to perform the NMR experiments described below, it is important to realize that the diffusion propagator that is used in the model to describe the self diffusion will have a dramatic effect on the calculated self diffusion coefficients. Others[4, 41, 42] have published very elegant derivations of model equations that describe self diffusion in various more complicated media.

5.4 Fundamental Pulse Sequences and Practical Concerns

The most fundamental pulse sequences used to study self diffusion are the spin echo and the stimulated echo - all other pulse sequences will simply be variants or extensions of these two pulse sequences. In all of these experiments, a magnetic field gradient in the z-direction allows one to probe diffusion in a single dimension. The graphical form of these pulse sequences is displayed in Figure 5.1. The corresponding equations describing the relaxation due to diffusion and relaxation are in Table 5.1.

Table 5.1: Equations describing signal attenuation due to diffusion and relaxation during field gradient NMR experiments. The total attenuation observed during a particular field gradient NMR experiment will be the product of the Diffusion Equation attenuation, the Relaxation Equation attenuation, and the resulting Magnetization. γ_n is the magnetogyric ratio of the nucleus under investigation, G is the magnetic field gradient used in the experiment, D is the self diffusion coefficient, T_1 is the spin-lattice relaxation time, and T_2 is the spin-spin relaxation time. The other parameters are as described in Figure 5.1. This table is based upon a very similar figure in [4].

Sequence	**Echo Time**	**Diffusion Equation**	**Relaxation Equation**	**Magnetization**
Ia	2τ	$Exp(-\gamma_n^2 G^2 D\delta^3(\frac{\Delta}{\delta}-\frac{1}{3}))$	$Exp(-\frac{2\tau}{T_2})$	1
Ib	$2\tau_1+\tau_2$	$Exp(-\gamma_n^2 G^2 D\delta^3(\frac{\Delta}{\delta}-\frac{1}{3}))$	$Exp(-\frac{2\tau_1}{T_2}-\frac{\tau_2}{T_1})$	$\frac{1}{2}$
IIa	2τ	$Exp(-\frac{2}{3}\gamma_n^2 G^2 D\tau^3)$	$Exp(\frac{2\tau}{T_2})$	1
IIb	$2\tau_1+\tau_2$	$Exp(-\gamma_n^2 G^2 D\tau_1^3(\frac{2}{3}+\frac{\tau_2}{\tau_1}))$	$Exp(-\frac{2\tau_1}{T_2}-\frac{\tau_2}{T_1})$	$\frac{1}{2}$

The four pulse sequences described above provide a great deal of flexibility when making diffusion measurements, especially in more challenging systems. The two most straightforward experiment (and most ideal) experiments are the pulsed gradient spin echo (PGSE) experiment, shown in Ia, and the pulsed gradient stimulated echo experiment (PGStE), shown in Ib. Both of these experiments use pulsed gradients, which are time dependent and (ideally) linear distortions of the homogeneous magnetic field. The great benefit of these experiments is that the second dimension of the experiment being performed is the strength of the gradient applied to the system. Because the timing of the pulses in the experiment does not change as the gradient strength is changed, the amount of relaxation that has occurred during the course of this experiment does not

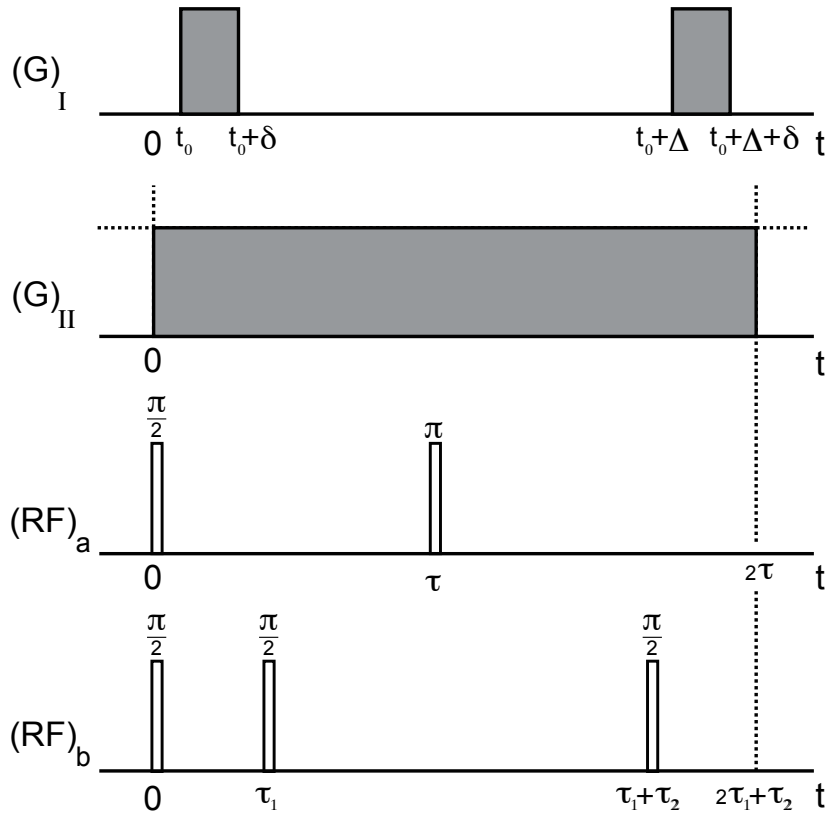


Figure 5.1: Gradient and RF pulse sequences used for diffusion studies. Gradient setting I demonstrates pulsed magnetic field gradients. Gradient setting II demonstrates a steady magnetic field gradient. RF pulse sequence (a) demonstrates the ordinary two pulse spin echo experiment. RF pulse sequence (b) demonstrates the three pulse stimulated echo experiment. The theoretical signal attenuation for ordinary isotropic unrestricted diffusion is shown in Table 5.1. This figure is based upon a very similar figure in [4].

change, and there is no need to include T_1 or T_2 relaxation in the fit equation for the self diffusion coefficient, D.

Another benefit to the PGSE and PGStE experiments is that both experiments have a single, well-defined diffusion time, Δ. This Δ corresponds to the time variable, t, in the diffusion propagator and allows the researcher to characterized the mean squared displacement of the diffusing spin. Thus, by knowing the dimensionality of the experiment (that is, the number of dimensions in which a field gradient is being applied, ψ), the self diffusion coefficient (which is measured by these experiments) and the diffusion time Δ (which is set by the experimenter), one can calculated the root mean squared displacement of the diffusing spin or molecule during the course of the experiment:

$$\sqrt{< r^2(t) >} = \sqrt{2\psi D\Delta}$$

For a standard field gradient experiment in which the field gradient is applied only in the Z-direction, $\psi = 1$. Such information is very useful when studying diffusion in restricted or possibly restricted systems, because the change in self diffusion coefficient with diffusion time allows one to quantify both local and macroscopic diffusion in the sample. Additionally, careful study of the self diffusion coefficient with root mean squared displacement will provide a measurement of the length scale of the restrictions present in the sample.

The PGSE experiment is perhaps the simplest pulse sequence to set up, but the PGStE experiment has several advantages in many cases. First, the stimulated echo pulse sequence reduces the limitation of the spin-spin relaxation constant (T_2, which appears in the Relaxation Equation column in Table 5.1) by storing the coherences along the axis of the magnetic field and thus causing the time limitation to be set by the longitudinal relaxation rate (T_1), and allowing much more time for diffusion in the case where $T_1 >> T_2$. Because T_2 is often short in experimental systems, the use of the PGStE experiment may be necessary for slowly diffusing molecules (or in molecules in which the ratio of attenuation of NMR signal due to diffusion over T_2 relaxation is very low) or in cases where the experimenter wishes to probe longer diffusion time scales (long Δs). In theory, slow diffusion can always be observed when one goes to higher and higher magnetic field gradients (G in the Diffusion Equations in Table 5.1). In practice, however, pulsed magnetic field gradients are created by passing current through anti-parallel Helmholtz coils, and the inductance of these coils will resist short pulses of current through them, resulting in gradient ringing. In order to avoid attenuation that is due to gradient ringing rather than diffusion, the minimum delay following the gradient pulse will grow as the magnitude of the pulse increases, and at some point this delay will exceed the T_2 of the system under investigation. The PGStE experiment, on the other hand, allows the experimenter to use smaller gradients and longer diffusion times for situations in which the diffusion is very slow. The price of the PGStE experiment is a theoretical decrease in the signal-to-noise by one half as a result of the *rf* pulse sequence (see Magnetization column in Table 5.1). Imperfect pulses can further decrease the signal to noise.

The steady gradient spin echo and stimulated echo experiments are less ideal experiments to be used for several reasons. First, during the course of these experiments, the parameter being changed is generally the time delay between *rf* pulses, rather than the magnitude of the gradient. (As an aside: In principle, the magnitude of the magnetic field gradient could be changed, but

this is challenging to do in practice, as will be discussed in more detail in the Methods section below. It is indeed possible to perform a pulsed field gradient experiment in which the pulsed gradients are simply on during the entire experiment. Unfortunately, the amount of current going through the gradient coils during this time is often so large that the experimenter risks melting the gradient coils, which is an expensive mistake in a commercial NMR probe.) This variation of time parameters in the pulse sequence requires the experimenter to include a relationship for all relevant relaxation parameters. Furthermore, because the steady gradient is typically also present during acquisition, chemical shift resolution is lost during acquisition. This is not generally a problem if all signal observed is due to a single mobile component, but if there are multiple diffusing species in the system, the model equation will grow to have a great number of parameters that have to be fit. It is usually possible to measure the relaxation parameters separately, which allows one to fix these parameters and simplify the model equation by one or two parameters.

A second unfortunate consequence of the steady gradient experiment is that neither experiment as displayed above has a single, well-defined diffusion time, Δ . This is not a problem if one is measuring diffusion of a molecule in a liquid, where the diffusing medium is homogeneous, but in materials that are expected to have restrictions, the measurement of the self diffusion coefficient will be made over a range of length scales, rather than over a single root mean squared distance. Pulse sequences have been developed to correct for this[4], but they are more challenging to execute in a pulse programmer and result in some loss of NMR signal, which may be a challenge in dilute systems.

A third and final disadvantage to the steady gradient experiment is observed when one uses very large magnetic field gradients. If the experimenter uses very high magnetic field gradients (as is often the case, for reasons described below), the line width of the NMR spectrum will become broad and is generally much wider than the excitation bandwidth of the NMR probe being used. The consequence of these experimental conditions is that only those spins within the bandwidth of the *rf* pulses will be observed, which can generally be quite small. This can make experiments on samples with a small number of diffusing molecules very time consuming, as the experiment probes only a small part of the sample. There are some ways in which one can make up for this problem by quickly varying the frequency of the experiment to probe more of the sample (especially during the recycle delay for long-T_1 systems), but this is unlikely to make up for the significant drop in signal to noise that will occur.

There are some advantages to the steady gradient pulse sequences, however. The first is that it removes the practical issue of gradient ring down seen in PGSE and PGStE experiments that make slowly diffusing systems with a short T_2 impossible with these methods. Depending on the relative values of T_1 and T_2, steady gradient PGSE or PGStE experiments may be the only way to characterize diffusion in slowly diffusing, short T_2 systems. The second great advantage of these experimental approaches is relates to variable temperature experiments. It turns out to be surprisingly difficult to create a pulsed gradient NMR probe that can reliably withstand temperatures above 260°C. The root of this problem is the fact that there are very few materials that can both act as insulators for gradient coils at high temperature and be shaped into coils with very small dimensions. Thermal management of the gradient coil temperature becomes even more complicated for such a system at high temperature. Lastly, the presence of very large, steady magnetic field gradients in every superconducting NMR magnet provides the experimenter with

access to these experiments without any specialized equipment. The method by which one goes about characterizing and performing such experiments will be discussed in great detail.

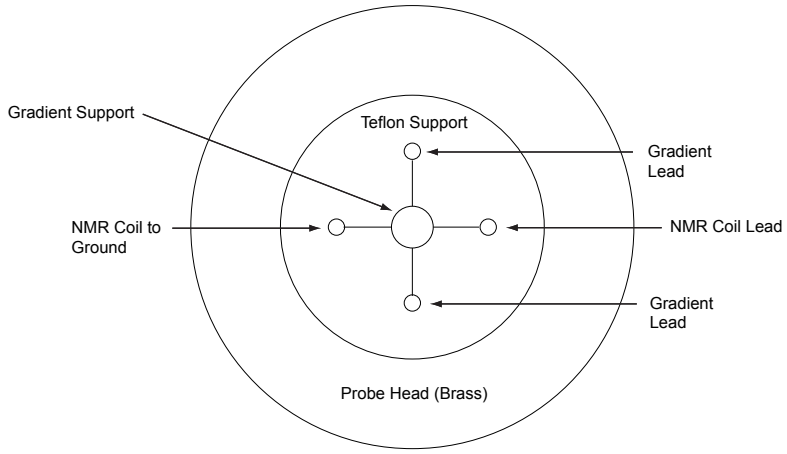
5.5 Methods

Two methods were explored for the measurement of proton self diffusion coefficients in rare earth phosphates at elevated temperatures. The first was the development of a ^{1}H NMR probe with the ability to create very high pulsed field gradients similar to a design by Zhang and Cory[47]. The second more successful method was to modify an existing NMR probe to be able to operate at high temperatures (up to 300°C) and in the frequency range of 288-300 MHz to perform STRAy FIeld (STRAFI) NMR measurements of self diffusion in rare earth phosphate samples.

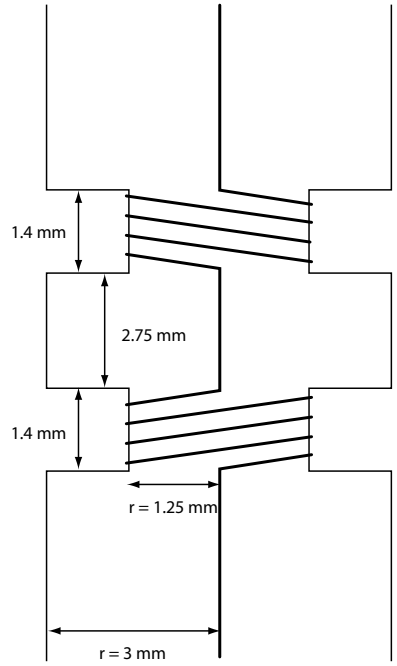
5.5.1 Development of a High Pulsed Field Gradient NMR Probe

Zhang and Cory[47] proposed several probe designs based on the observation that it is relatively easy to generate very large pulsed (magnetic) field gradients over very short distances with a relatively small amount of current. The probe designs that they investigated involved a single-, 4- and 31-turn gradient set of varying size in order to generate magnetic field gradients from from 100-600 T/m. (For comparison, even specially-designed commercial PFG NMR probes have upper limits of approximately 15 T/m and require elaborate water cooling devices to keep the probe from melting.) Because the self diffusion of protons is expected to be slow in rare earth phosphates, and because T_2's at room temperature were very low, a modified 4-turn pulsed field gradient probe was designed and constructed to understand the feasibility of further adapting such a design for high temperature PFG NMR studies in rare earth phosphates. The probe was constructed as depicted in Figure 5.2. The gradient support was constructed from a 6 mm diameter rod of Teflon that was machined to the dimensions shown in the figure. The gradient coils consist of 34 AWG magnet wire with four turns for each of the anti-parallel Helmholtz coils which were held in place with epoxy. The ends of the gradient wires were connected to wires that exited the bottom of the probe where they were connected to the Techron DC amplifier for diffusion studies (The nontrivial spectrometer setup from the Tecmag LapNMR to the Techron DC amplifiers is discussed in the Appendix). The magnet wire is covered with a polymeric coating that was sanded off prior to being soldered to the wires that led to the Techron DC amp-to-probe cables. The *rf* coil was also constructed from 34 AWG magnet wire by wrapping several coils around a capillary tube that was cut 2mm longer than the diameter of the Teflon rod. A small *rf* coil was used both to ensure that the sample was present in the linear region of the pulsed field gradient generated by this gradient coil design, and to take advantage of the useful properties of microcoils[48] that have been seen by other researchers. The *rf* coils were held to the capillary tube using epoxy, and then the *rf* coil and capillary tube were placed into the hole in the Teflon rod and fasted with epoxy to ensure that no movement took place during experiments. The coil was then connected to variable capacitors in a standard tank circuit layout with a match and tune capacitor. Fixed capacitors were then added to the variable capacitors to tune the circuit to 65.6 MHz and 50Ω impedance.

Calibration experiments were performed using the pulsed gradient spin echo (PGSE) experiment on glycerol at 25°C. These experiments were performed at a frequency of 65.58 MHz. The



(a) The top view of the PFG probe



(b) The side view of the gradient support of the PFG probe

Figure 5.2: The top view (a) and side view (b) of the homebuilt PFG NMR probe based on the design of Zhang and Cory[47]. The NMR coil is a standard solenoid connected to a Tank circuit that has leads entering and leaving the gradient support perpendicular to the gradient coil leads, as can be seen in (a). The gradient support is made of Teflon, and is connected to a Teflon support that is connected to the brass head of the probe. In (b), the anitparallel Helmholtz gradient coils are shown, which are necessary for creating a linear magnetic field gradient in the sample volume of the probe. The dimensions of the gradient support are provided. The axis of the *rf* coil (not shown) goes from left to right parallel to the plane of the picture in the 2.75 mm region between the gradient coils.

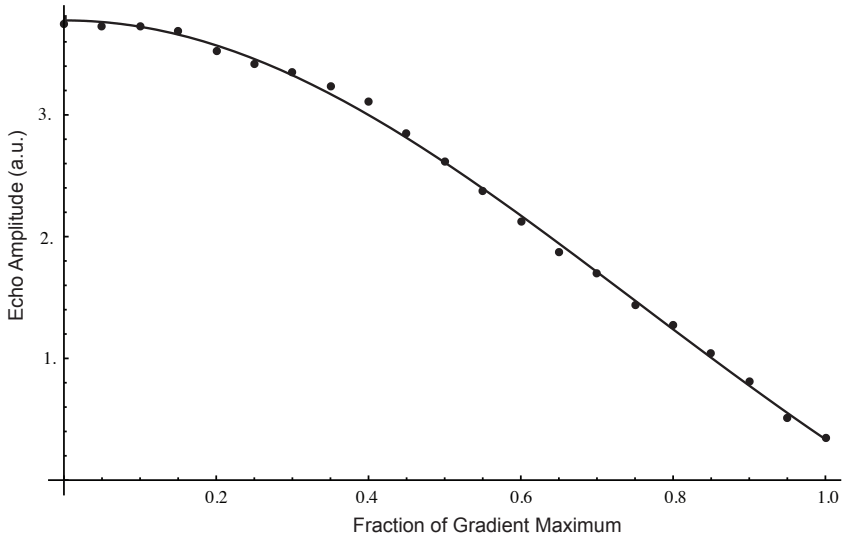


Figure 5.3: The experimental results of a pulsed gradient spin echo experiment at 65.58 MHz. Glycerol was used as a diffusion standard at room temperature. The line is a nonlinear regression best fit to the data and indicates a field gradient of 27.9 T/m.

experiments were run with a standard 8-step spin echo phase cycle, with $frac\pi 2$ and π rf pulses of 1.3 and 2.6μs, respectively. Gradient pulses were approximately square and were applied for durations (δ) ranging from 0.9-4 ms. A delay of 10 ms was allowed after each gradient pulse to allow for gradient ring down to cease, and the total diffusion time (Δ) for the experiments ranged from 12-15 ms and was changed as the gradient pulse duration was changed. Because glycerol is an ordinary, isotropic, homogeneous liquid, no dependence upon diffusion time was expected or observed.

Figure 5.3 shows the result of a field gradient calibration on glycerol using equation Ia from Table 5.1. The computed magnetic field gradient was 27.9 T/m. To calculate the magnitude of the magnetic field gradient, the self diffusion coefficient of glycerol was taken to be[49] $1.37{\cdot}10^{-12}$ m^2s^{-1} at 20°C. The results of multiple experiments demonstrated that the gradient could be adjusted from 12 to 50 T/m using the gradient control settings on the Tecmag LapNMR spectrometer. Unfortunately, higher field gradient settings required gradient ring down times in excess of 10 ms, which is much longer than the expected T_2 relaxation time in most rare earth phosphates at elevated temperatures. In order to circumvent these ring down problems, steady gradient techniques were pursued.

5.5.2 STRAy FIeld (STRAFI) NMR for High Temperature Self Diffusion Measurements

In order to perform stray field nmr self diffusion studies on a 7.05 T superconducting magnet, a Chemagnetics CMP200SNRS-2196 static NMR probe was adjusted so that it tuned in

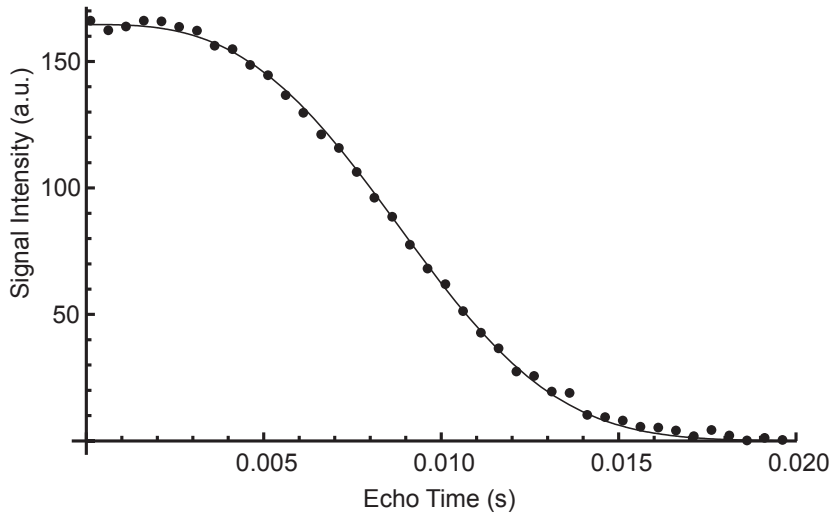


Figure 5.4: The experimental results of a steady gradient spin echo experiment in the stray magnetic field of a 7.05 T (300 MHz) NMR magnet as a distance of 0.054 m from the sweet spot of the magnet. Water was used as a diffusion standard at room temperature. The line is a nonlinear regression best fit to the data and indicates a field gradient of 0.094 T/m.

the range of 288-300 MHz. In order to characterize the magnetic field and the magnetic field gradient as a function of height, a sample of known self diffusion coefficient was placed in the NMR probe and a spin echo experiment was performed as the NMR coil was moved increasingly below the center of field on the magnet. Deionized water was used as a diffusion standard. A typical calibration experiment is shown in Figure 5.4 where water was used as a diffusion standard and the magnetic field gradient was found to be 0.94 T/m. These experiments were then repeated at multiple heights below the sweet spot of the magnet, and Figure 5.5 shows the magnetic field strength (in T) and the magnetic field gradient (in T/m) as a function of distance below the sweet spot of the magnet.

In order to confirm the consistency of the magnetic field gradients, the gradient was calculated using water to be 9.9T at 0.12 m below the sweet spot. The literature value[49] for the self diffusion coefficient of glycerol at 20°C is $1.37*10^{-12}$ m^2s^{-1}. The stray field steady gradient spin echo experiment shown below in Figure 5.6 indicates a self diffusion coefficient of $1.25+/-0.02*10^{-12}$ m^2s^{-1}, which is acceptably close since no temperature control was used during this experiment.

In order to control over the temperature of the sample in the *rf*, homemade connections were made between a Chemagnetics VT stack (VTPH-131) and Chemagnetics VT control box (ARBS A-050) so that gas entering the VT stack was heated to a temperature entered on the VT control box. Homemade connections were also made between the VT control box and a MAS control box in order to shut down the heater in the event of a loss of supply gas pressure. (Because there was no user manual for this equipment, the interfaces among the VT stack, the VT controller, and the MAS box have been documented in the Appendix). The Chemagnetics VT stack is both

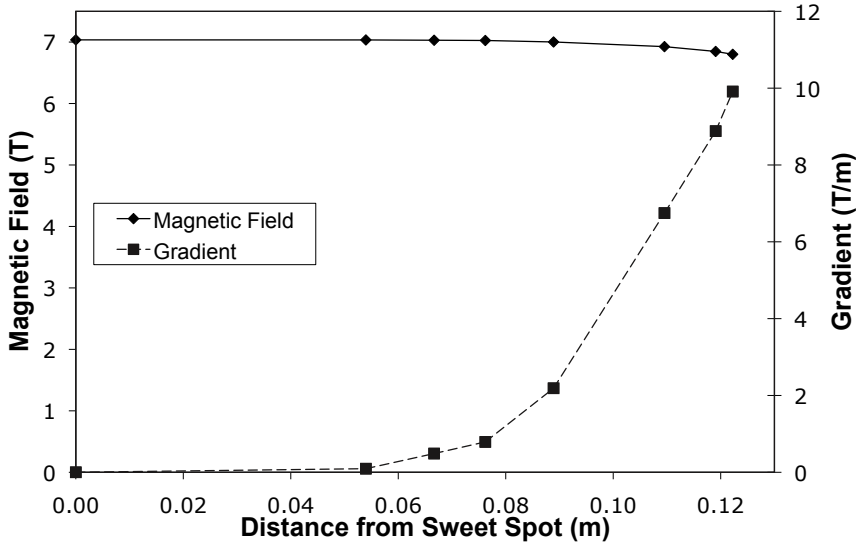


Figure 5.5: The magnetic field (T) and the magnetic field gradient (T/m) of a 7.05 T NMR magnet as a function of distance from the sweet spot of the magnet. Water was used as a diffusion standard at room temperature.

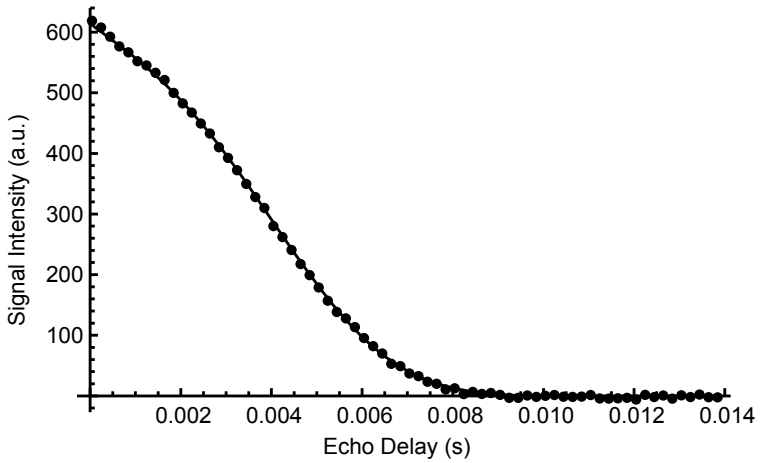


Figure 5.6: The experimental results of a steady gradient spin echo experiment in the stray magnetic field of a 7.05 T (300 MHz) NMR magnet as a distance of 0.12 m from the sweet spot of the magnet. The self diffusion coefficient of glycerol was measured after using water as a diffusion standard at room temperature. The line is a nonlinear regression best fit to the data and indicates a self diffusion coefficient of 1.25+/-0.02*10^{-12} m^2s^{-1}.

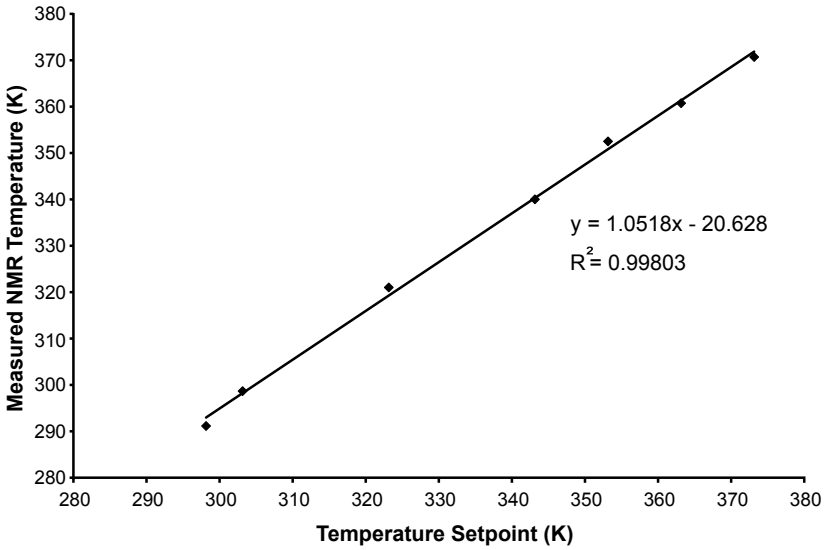


Figure 5.7: The experimental results of a variable temperature experiment in the stray field NMR probe. The temperature setup on the Chemagnetics VT control is compared to the temperature calculated by the chemical shift difference in a glycerol spectrum. The linear regression best fit line provides a transfer function from temperature set point to actual temperature.

able to fit in the magnet (which is a 7.05 T Chemagnetics magnet) and interface with the top of the Chemagnetics NMR probe. All samples being run with temperature control were run sealed in a silicon nitride rotor with short glass reinforced Torlon caps that are far outside the NMR coil. Shims made of Teflon tape were used to ensure that the rotor does not move in the NMR coil during experiments. A temperature calibration was done with ethylene glycol, a standard ^{1}H NMR reference compound for calibrating temperature[50]. Figure 5.7 shows the temperature calibration over a limited range and provides a transfer function from temperature set point to actual temperature in absolute temperature (K). The variable temperature stack has a temperature range of up to 300°C. The probe, which is made of vespel, does not have a temperature rating posted on it, but is likely functional up to 300°C (the maximum temperature that most NMR manufacturers list for non-MAS parts on high temperature NMR probes). For all experiments above 150°C, nitrogen gas was used as the VT gas to avoid any oxidation of VT stack or NMR probe parts during experiments.

Two high temperature experiments were done to confirm that (a) the variable temperature was operating roughly as intended, (b) the gradient that measured by glycerol was reliable, and (c) to ensure no mechanical vibrations were occurring as a result of the variable temperature operation during high temperature experiments. The pulse sequence for these experiments was a modified steady gradient spin echo experiment in which the initial spin echo acquired is followed by a CPMG[51, 52] pulse sequence and is identical to what is done in magnetic resonance imaging in which steady magnetic field gradients are used[53, 56]. The pulse sequence is shown in Figure

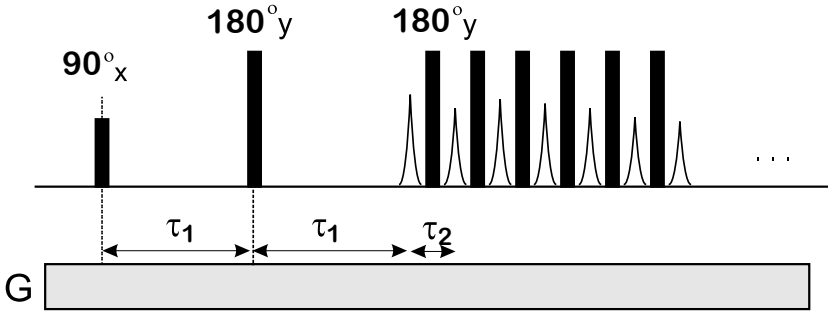


Figure 5.8: The STRAFI CPMG pulse sequence is used to acquire more signal for every time setting of the STRAFI pulse sequence. The pulse sequence begins as in IIa in Figure 5.1 but is then followed by a series of 180°(π) pulses, resulting in a long string of echos. During the course of the pulse sequence, only the time parameter τ_1 is changed. The parameter τ_2 is optimized based on the echo width before the experiment is started and remains the same throughout the experiment.

5.8. $\frac{\pi}{2}$ pulses of 6μs and π pulses of 12μs were used, 40 two dimensional points were acquire and 64 echos were acquired for each scan.

Figures 5.9 and 5.10 show the results of these two proof of principle experiments. Both experiments were performed on a 50-50 ionic liquid mixture consisting of imidazole and HTFSI. Because there are currently no literature values of the self diffusion coefficients of this ionic liquid mixture, self diffusion coefficients were extrapolated from unpublished data from Megan Hoarfrost, who has characterized these materials at lower temperatures. Assuming constant activation energy in this sample, the predicted self diffusion coefficient at 150°C is 3.6*10^{-10} m^2s^{-1} and at 250°C is 1.85*10^{-9} m^2s^{-1}. The values measured using the STRAFI CPMG pulse sequence with single diffusion fit that simultaneously fit T2 gave self diffusion coefficients of 5.4+/-0.2*10^{-10} m^2s^{-1} at 150°C and 1.81+/-0.06*10^{-9} m^2s^{-1} at 250°C. The agreement of the data is surprisingly good, especially at high temperature. This is very important as experiments above 250°C are most interesting for proton motion in rare earth phosphates.

The STRAFI CPMG experiments described below are on the B1 sample that was synthesized as given in Harley and De Jonghe[58]. As noted in this reference, this sample is approximately a 20% barium-doped lanthanum metaphosphate glass. The sample was stored in a glove box until loaded in a 5mm silicon nitride rotor with glass reinforced Torlon caps. $\frac{\pi}{2}$ pulses of 6μs and π pulses of 12μs were used. Each experiment used 40 two-dimensional time delays ranging from 0.1 ms to 4ms in order to quantify the attenuation due to self diffusion taking place. For each two dimensional time setting, 64 echos were acquired. For each experiment, a T_2 was calculated from the CPMG echo train in order to ensure that the T_2 was not changing during the course of the experiment. The T_1 did not change significantly over the course of the temperature range investigated and remained approximately 400 ms. A recycle delay of at least 2 s was used for all experiments.

A single self diffusion coefficient was not sufficient to fit the resulting STRAFI CPMG

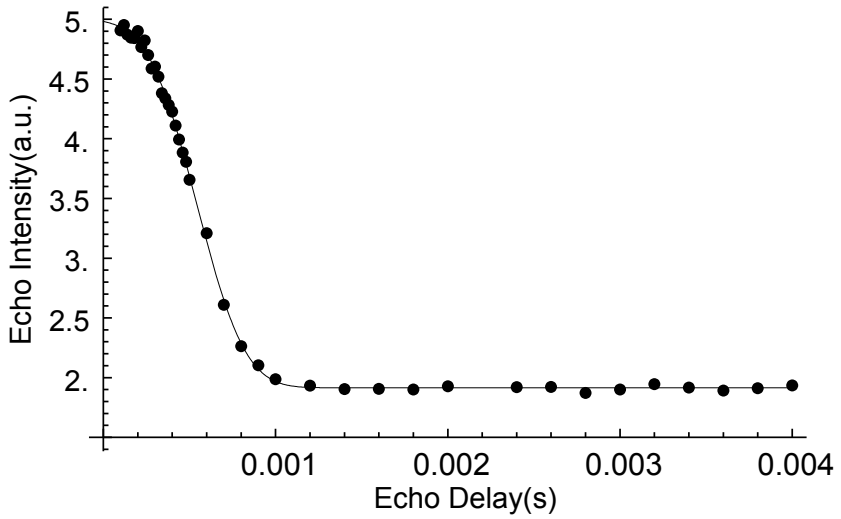


Figure 5.9: The experimental results of a STRAFI CPMG experiment at 150°C using the stray field NMR probe. The nonlinear regression analysis gives a result of 5.4+/-0.2*10^{-10} m^2s^{-1}. Because there is no literature value, an expected self diffusion coefficient was extrapolated from unpublished data by Megan Hoarfrost. The prediction was 3.6*10^{-10} m^2s^{-1}.

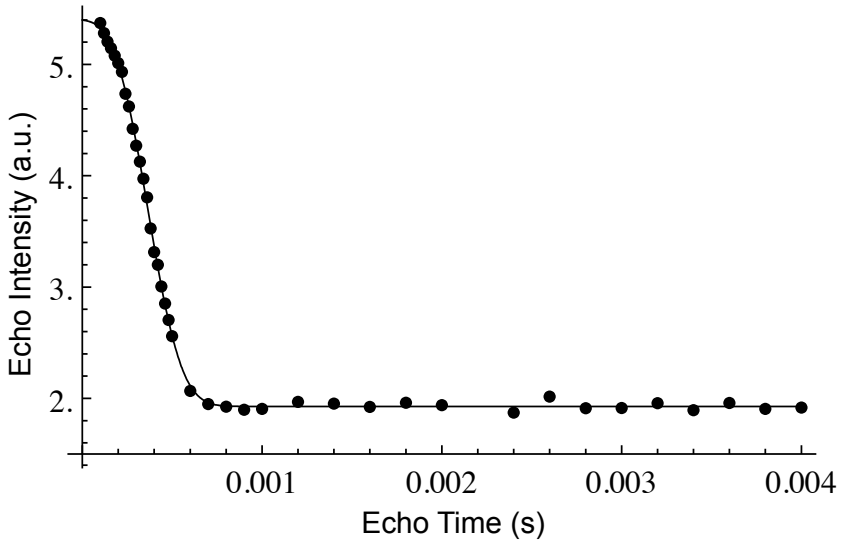


Figure 5.10: The experimental results of a STRAFI CPMG experiment at 250°C using the stray field NMR probe. The nonlinear regression analysis gives a result of 1.81+/-0.06*10^{-9} m^2s^{-1}. Because there is no literature value, an expected self diffusion coefficient was extrapolated from unpublished data by Megan Hoarfrost. The prediction was 1.85*10^{-9} m^2s^{-1}.

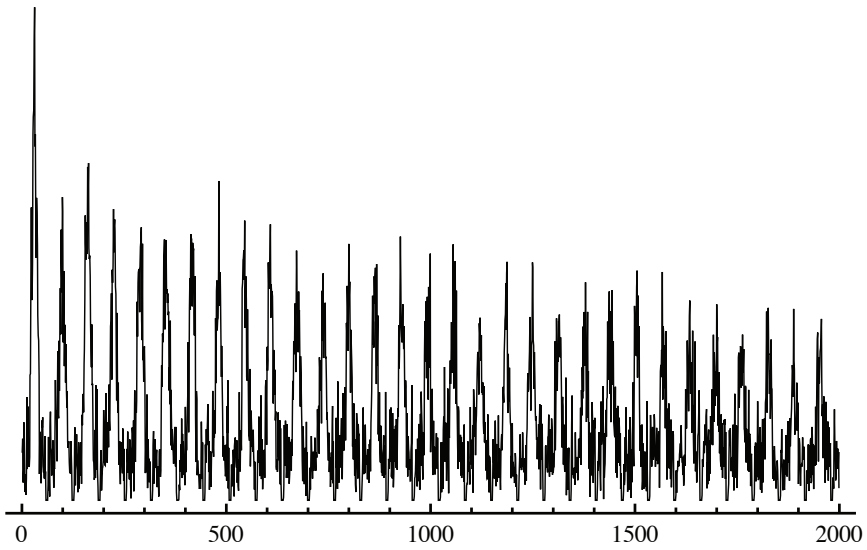


Figure 5.11: The first acquisition in the STRAFI CPMG experiment on the B1 barium lanthanum phosphate glass sample at 200°C using the stray field NMR probe. The magnitude of the signal provides information on the self diffusion coefficient of the protons in the sample, and the decay of the echos with time can provide the T_2 of the sample.

experiment, and so the data was fit with a two-diffusion component model with T_2 (which was measured separately) fixed. Data was acquired using the sample pulse sequence and settings from 140-280°C. The model use for all of these fits was,

$$S(G) = A * (x * Exp(-\frac{2}{3}\gamma_n^2 G^2 D_1 \tau^3) + (1-x) * Exp(-\frac{2}{3}\gamma_n^2 G^2 D_2 \tau^3)) * Exp(\frac{2\tau}{T_2}) + B$$

When compared to the model equations provided in Table 5.1, this model assumes that there is only one T_2 present in the system (which is all that was seen for this sample) but two self diffusion coefficients. The parameter x provides a relative fraction of species with self diffusion coefficient D_1 versus D_2. The parameters A and B are used to describe the total signal intensity and any data baseline offsets, respectively.

5.6 Results and Discussion

Figure 5.11 one shows the first 2000 μs of the acquisition of the first time setting in a STRAFI CPMG experiment performed at 200°C. In order to determine the self diffusion coefficient of the protons in the sample, all of the echos can be added together for each two dimensional time setting, and then the summations of each two dimensional point can be plotted versus the time parameter of the second dimension to allow for a fit to extract self diffusion coefficients from the data. In order to simplify the fit parameters, however, first the decay in the amplitude of the

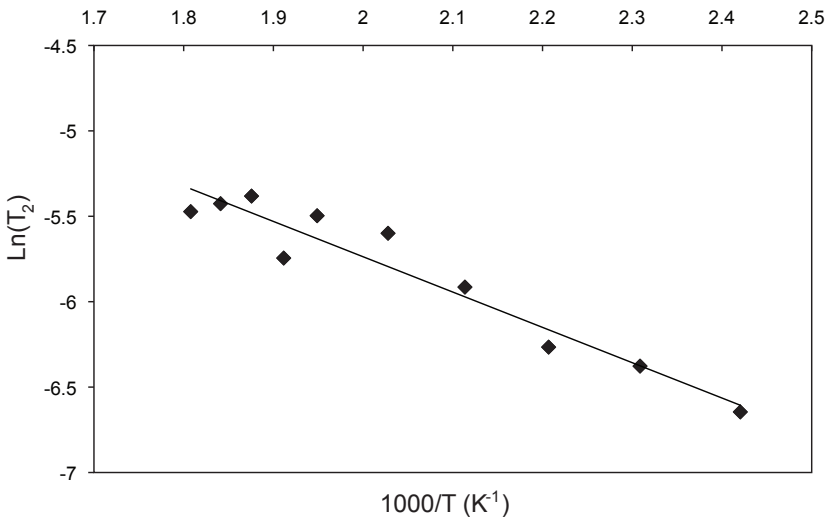


Figure 5.12: Natural logarithm of T_2 as a function of 1000/T for the B1 sample. The linear best fit of all of the data is displayed on the plot. The slope corresponds to an activation energy of 0.17 eV.

echos with time can be used to determine the T_2 of the protons in the sample. This is done using standard nonlinear regression techniques for a single exponential decay. The T_2 was also measured using a Hahn echo at the center of field in the magnet, and only one T_2 was observed.

Figure 5.12 shows the T_2 measured from the CPMG data present in the first two dimensional acquisition at each temperature, plotted in a Ln(T_2) versus 1000/T fashion. A linear regression of this data provides an activation energy of 0.17 eV. This activation energy is much lower than that calculated from conductivity measurements of this sample[58]. A study of proton transfer mechanisms in lanthanum orthophosphate[14] suggested that rotations about a phosphate group (which does not directly contribute to proton conduction but may facilitate other transfer processes) would have an activation energy of approximately 0.14 eV, and oscillatory proton transfer (which also does not directly contribute to proton conduction but may facilitate other transfer processes) would have an activation energy of approximately 0.1 eV. Although the structure of the lanthanum orthophosphate is different to that of this barium lanthanum metaphosphate glass, it is possible that the energetic barriers are similar for the two systems.

A summary of the calculated self diffusion coefficients is given in Table 5.2. Figure 5.13 shows the results of the two-self diffusion coefficient with a fixed T_2 fits performed on all of the data, also plotted as in a Ln(D) versus 1000/T fashion. In this data, it is seen that there is a consistent fast and slow diffusion coefficient. The fast diffusion coefficient is on the order of 10^{-9} m^2s^{-1}, which is much faster than would be expected of a material with such low conductivity measurements in this temperature range. Unfortunately, the spin echo experiment does not have a well defined diffusion time (or diffusion length) under steady gradient conditions, but using the echo delay times to approximate a diffusion time provides a range of diffusion distances from 630-4000

Table 5.2: The calculated self diffusion coefficients are displayed as a function of temperature. The uncertainties of the self diffusion coefficients measured in the 140°C experiment are both as large or larger than the calculated values themselves.

Temperature, °C	**D_1, 10^{-9} m^2s^{-1}**	**D_2, 10^{-11} m^2s^{-1}**
140	4. +/- 4.	0.5 +/- 2
160	1.2 +/- 0.6	1. +/- 1.
180	1.1 +/- 0.6	1. +/- 1.
200	1.5 +/- 0.5	1.1 +/- 0.3
220	1.1 +/- 0.3	0.96 +/- 0.2
240	1.2 +/- 0.3	1.0+/- 0.2
250	0.97 +/- 0.2	2. +/- 1.
260	1.9 +/- 0.9	4. +/- 2.
270	2.8 +/- 0.8	8. +/- 3.
280	2.3 +/- 0.6	8. +/- 3.

nm. Such self diffusion of mobile protons over these large length scale would be expected to observed in the conductivity measurements. This quickly diffusing component also does not appear to have a temperature dependence, which is unexpected. The absence of a high conductivity suggests that this mobile species may be some quickly diffusing species that contributes to the proton diffusivity but not the proton conductivity, such as some sort of confined water.

The slowly diffusing proton is characterized by a diffusion coefficient on the order of 10^{-11} m^2s^{-1} in this temperature range. This motion is also somewhat fast for a material with such a low conductivity at these temperatures. The length scales probed in these experiments range from 63-400 nm, which is much smaller than the region probed by the quickly diffusing species. It is possible that these protons are probing only local domains of the material and are not moving at this speed over larger distances in the materials. No crystalline regions were found in this material using X-ray diffraction in the structural characterization of this material[59], and there is no evidence of sample heterogeneity. Unpublished work by Jian Feng used a ^{1}H -^{137}Ba TRAPDOR experiment to show that protons in this material are proximate to the barium cations in the material (on the order of 0.3 nm), but these experiments gave no indication of whether or not these proton-barium couples resided in a separate phase of the material or not.

A close inspection of the slowly diffusing proton data in Figure 5.14 suggests that a transition in proton motion takes place at approximately 240°C. A linear regression on the data up to 240°C and on the data from 240-280°C suggests provides two activation energies. The activation energy calculated below 240°C is 0.11 eV, which is relatively close to that observed from the T_2 data. The activation energy calculated above 240°C is 1.4 eV. In both cases, the uncertainty of the activation energy calculation is very large due to the small sample size and the propagated uncertainty from the self diffusion fits. The B1 barium lanthanum phosphate sample synthesized and studied by Harley and De Jonghe[58] demonstrated an activation energy from conductivity measurements (performed in dry argon) of 0.977 eV, while the larger range of barium

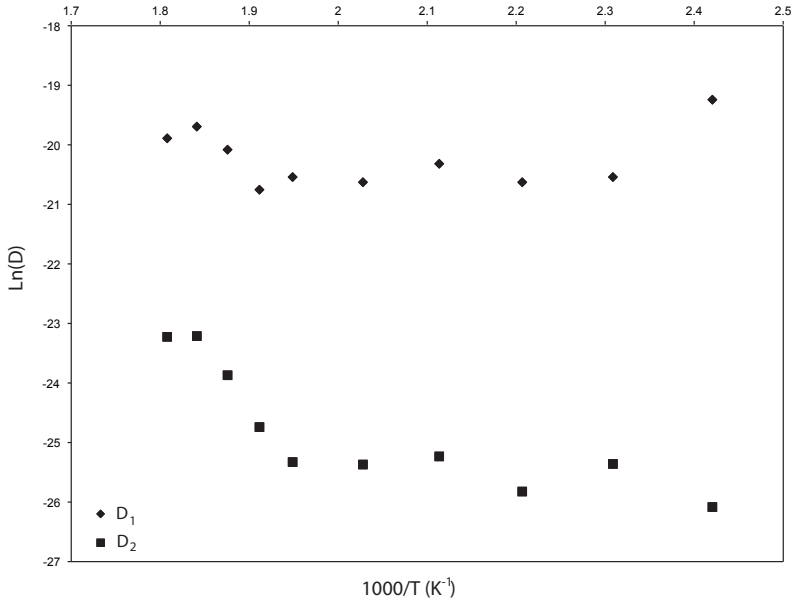


Figure 5.13: Natural logarithm of the two self diffusion coefficients as a function of 1000/T for the B1 sample.

lanthanum phosphates demonstrated activation energies of 0.9-1.02 eV. The study of proton transfer mechanisms in lanthanum orthophosphate by Yu and De Jonghe[14] suggested an activation energy of approximately 0.9 eV for intertetrahedral proton transfer, which is the dominant mode of long-range proton transport in lanthanum orthophosphate. The experimental observation of a similar activation energy in this barium lanthanum metaphosphate suggests that the proton transport mechanism is similar, and the observation of a 1.4 eV activation energy for proton self diffusion in this material at temperatures above 240°C suggests that the self diffusion measurement is also accessing such intertetrahedra proton transport.

An alternative explanation for the multiple self diffusion coefficients observed by this system could be the observation of a localized (fast) and more long-range (slow) self diffusion coefficients. Such a system could be described using the Kaerger model[60] or the modified Kaerger model given by Price[41]. Unfortunately, the number of free parameters in these models (terms that describe both types of self diffusion, exchange timescales between the two groups, etc) that they are very difficult to fit with certainty. One possible solution would be to execute the more sophisticated pulse sequences described by Kimmich[4] that remove relaxation from the experimental results. The equations in the Kaerger and Price models would have to be modified to reflect the more complicated nature of diffusion under these conditions.

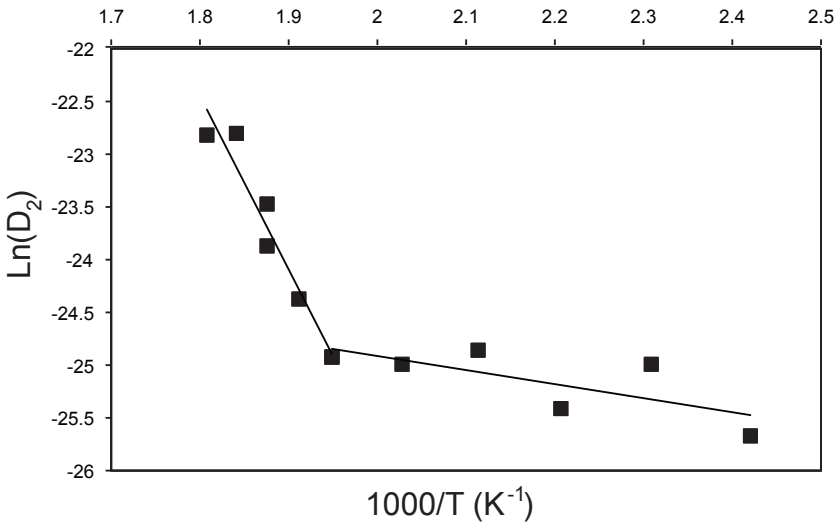


Figure 5.14: Natural logarithm of the slower self diffusion coefficient as a function of 1000/T for the B1 sample. A transition in the slope of the self diffusion behavior is seen at 240°C, which corresponds to a change in the activation energy from 0.11 eV to 1.4 eV.

5.7 Conclusions

In this work, field gradient nuclear magnetic resonance techniques have been adapted to probe proton self diffusion in rare earth phosphates. Two approaches to measure self diffusion were pursued. The first approach, that of a small-dimensioned PFG NMR probe, produced the necessary high magnetic field gradients, but the gradient coils required gradient ring down times far in excess of proton T_2s (the limiting time parameter) in these systems. The stray field of a superconducting magnet was used to perform stray field steady gradient NMR experiments which, when coupled to a modified variable temperature ^{1}H NMR probe, were able to measure two proton self diffusion coefficients as a function of temperature. The faster proton self diffusion coefficient was much higher than that anticipated for a proton conductor of relatively low conductivity measurements. At temperatures below 240°C, the slower proton self diffusion coefficient showed an activation energy consistent with oscillatory or rotational proton motion in a rare earth phosphate. At temperatures above 240°C, the slower proton self diffusion coefficient showed an activation energy more consistent with the activation energy determined from conductivity measurements and in agreement with the theoretical activation energy of longer range motion in a rare earth phosphate material.

5.8 Future Work

The STRAFI CPMG experiment quantified the self diffusion coefficients of two types of protons in the barium lanthanum phosphate sample: one fast diffusing and the other slow

diffusing. In order to understand the relationship between phosphate structure and proton dynamics in this material, it is necessary to unambiguously identify these mobile species. ^{1}H -^{31}P cross polarization (CP) and heteronuclear correlation spectroscopy (HETCOR) experiments will be used to understand which of the proton chemical shifts are associated with the phosphate groups present in this sample. The sample will also be studied carefully to determine whether or not a significant fraction of the proton NMR signal is due to the presence of water. Assignment of the proton chemical shift(s) and correlation with the phosphate structure combined with the quantified proton self diffusion coefficients is expected to provide a useful picture of how protons move through the barium lanthanum phosphate glass material that can aid future material science efforts.

More generally, the STRAFI CPMG method should be modified so proton self diffusion measurements could be made under conditions in which relaxation effects are minimized (which would greatly simplify data analysis) and under experimental conditions providing a well-defined diffusion time. Modified three-pulse and five-pulse STRAFI experiments (so called "superconfringe field" (SFF) experiments) have been proposed by Kimmich [4], but have only been applied to model systems. These experiments are very helpful in that they do not require any knowledge of the relaxation parameters. Both experiments also have a well defined diffusion time, which will allow exploration of variable diffusion time experiments that allow the NMR experiment to probe larger and larger length scales of proton transport in the material. The disadvantage of these experiments is that the analysis is complicated by the presence of residual dipolar or quadrupolar coupling. A further modification of these pulse sequences, referred to as the constant time steady gradient (CTSG) experiment in the literature [61], involves the application of a five-pulse stimulated echo experiment. This experiment compensates for both relaxation and residual dipolar interaction effects while maintaining a well-defined diffusion time. These experiments have only been used as proof-of-principle experiments on poly(ethylene oxide) melts at modest temperatures but can be easily adapted for high temperature experiments in more complicated materials. Furthermore, a CPMG echo train can be added to the end of the five-pulse SFF experiment and the five-pulse CTSG experiment to improve the signal-to-noise of these experiments for systems in which the concentration of mobile species is low.

These experimental approaches are ideally suited for rare earth phosphate systems with longer T_1s, such as lanthanum phosphate materials. With the addition of variable diffusion time experiments, the behavior of the self diffusion coefficient over longer and longer length scales can be probed to compare the local and more macroscopic self diffusion behavior of protons in these materials. This would help to answer two of the interesting questions that arose in the case of the barium lanthanum phosphate sample: First, what is the nature of the fast diffusing proton? That is, why is there a proton that is diffusing so quickly (nearly as fast as a liquid at room temperature) in a system that has a very low conductivity? Variable diffusion time experiments in parallel with the aforementioned ^{1}H -^{31}P CP experiments should help to determine if this is a very mobile but trapped proton species or if it is simply water that has not left the sample system even at high temperatures. The second question that arose in the barium lanthanum phosphate material is related to the slower diffusing proton species. What is the nature of that proton? The variable temperature self diffusion behavior suggest that this is more likely to be the proton observed during variable temperature conductivity measurements. The behavior of this proton as it crosses various micro-structural domains in these rare earth phosphates will be of great interest in the effort to

increase the proton conductivity of these materials.

Finally, with these more sophisticated pulse sequences, more sophisticated diffusion models, such as those proposed by Kaerger [60] and Price [41], can be adapted for use in steady gradient experiments to provide insight into the mechanism of proton transport in rare earth phosphate systems. In the case of the barium lanthanum phosphate glass, self diffusion coefficients are the only NMR-acquired parameter that distinguishes the fast and slow diffusing protons in the material - there is currently no spectroscopic (due to experimental reasons) or relaxation ^{1}H NMR parameter that distinguishes these protons from one another. One possible explanation, as has been assumed above for the time being, is that these are two unique types of protons in the material that have very similar relaxation parameters. Another possibility is that these are the same protons, some of whom are diffusing locally and some of whom are mobile over a larger length scale. The Kaerger and Price models have been developed to address these and other similar situations. The outcome of such experiments will provide a substantial amount of information on phosphate domains that assist and/or hinder proton motion in rare earth phosphates. Such information will be of great utility in developing improved proton conducting materials.

Bibliography

[1] T. Norby, "Solid-state protonic conductors: principles, properties, progress and prospects," *Solid State Ionics*, 125 (1999) 1-11

[2] K. Amezawa, S. Kjelstrup, T. Norby, Y. Ito, "Protonic and native conduction in Sr-substituted $LaPO_4$ studied by thermoelectric power measurements," *J. Electrochemical Soc.*, 145 (1998) 3313-3319

[3] N. Kitamura, K. Amezawa, Y. Tomii, N. Yamamoto, "Protonic conduction in rare earth orthophosphates with the monazite structure," *Solid State Ionics*, 162-163 (2003) 161-165

[4] R. Kimmich, *NMR Tomography, Diffusometry, Relaxometry*, Springer, (1997).

[5] S. Malhotra, R. Datta, "Membrane-supported nonvolatile acidic electryolytes allow higher temperature operation of proton-exchange membrane fuel cells," *J. Electrochemical Soc.*, 144(2) (1997) L23-L26.

[6] G.J. Zhang, R. Yu, S. Vyas, J. Stettler, J.A. Reimer, G. Harley, L.C. De Jonghe, "Proton conduction and characterization of an La(PO3)3-Ca(PO3)2 glass-ceramic," *Solid State Ionics*, 178(35-36) (2008) 1811-1816

[7] S. Cadars, B.J. Smith, J.D. Epping, S. Acharya, N. Belman, Y. Golan, B.F. Chmelka, "Atomic positional versus electronic order in semiconducting ZnSe nanoparticles," *Physical Review Letters*, 103 (2009) 136802.

[8] A. G. Dias, M. A. Lopes, K. Tsuru, S. Hayakawa, J.D. Santos, A. Osaka, "^{31}P MAS-NMR studies of CaO-P_2O_5 Glass Ceramics," *Key Engineering Materials*, 309-311 (2006) 301-304.

[9] J. P. Fletcher, R. J. Kirkpatrick, D. Howell, S. H. Risbud,"^{31}P Magic-angle spinning nuclear magnetic resonance spectroscopy of calcium phosphate glasses," *J. Chem. Soc. Faraday. Trans.*, 89(17) (1993) 3297.

[10] N.E. Rashid, B.L. Philips, S.H. Risbud, "Solid-state nuclear magnetic resonance study of the structure of lanthanum phosphate crystals and glasses," *J. Mater. Res.*, 15(11) (2000) 2463.

[11] R. K. Brow, C. C. Phifer, G. L. Turner, and R. J. Kirkpatrick, "Cation effects on ^{31}P MAS NMR chemical shifts of metaphosphate glasses" *J. Am. Ceram. Soc.*, 74(6) (1991) 1287-1290.

[12] H.L. Ray, L.C. De Jonghe, "Identification of charge carriers in cerium phosphate ceramics," *ECS Transitions*, 28(11) (2010) 243-249.

[13] H.L. Ray, L.C. De Jonghe, R. Wang, "Rare Earth Phosphate Glass and Glass-Ceramic Proton Conductors, *ECS Transactions*, 16(51) (2009) 389-393

[14] R. Yu, L.C. De Jonghe, "Proton-transfer mechanism in $LaPO_4$", *J. Phys. Chem. C*, 111 (2007) 11003.

[15] S. Gallini, J.R. Jurado, M.T. Colomer, "Synthesis and characterization of manazite-type Sr:$LaPO_4$ prepared through coprecipitation," *Journal of the European Ceramic Society*,25 (2005), 20032007.

[16] N. Kitamura, K. Amezawa, Y. Tomii, T. Hanada, Y. Yamamoto, T. Omata, S. Otsuka-Yao-Matsuo, "Electrical conduction properties of Sr-doped $LaPO_4$ and $CePO_4$ under oxidizing and reducing conditions," *Journal of The Electrochemical Society*, 4 (2005) A658-A663.

[17] K. Amezawa, H. Maekawa, Y. Tomii, N. Yamamoto, "Protonic conduction and defect structures in Sr-doped $LaPO_4$," *Solid State Ionics*, 145 (2001) 233 240.

[18] K. Amezawa, Y. Kitamura, Y. Tomii, N. Yamamoto, M. Wideroe, T. Norby, "Protonic conduction in acceptor-doped LaP_3O_9," *Solid State Ionics*, 176 (2005) 2867 2870.

[19] R. Colvin, S. Arajs, J.M. Peck, "Paramagnetic behavior of metallic cerium and europium," *Physical Review*, 122(1) (1961) 14-18.

[20] I. Bertini, C. Luchinat, G. Parigi, R. Pierattelli, "NMR spectroscopy of paramagnetic metalloproteins," *ChemBioChem*, 6 (2005) 1536 1549.

[21] G. Harley, R. Yu, L.C. De Jonghe, "Proton transport paths in lanthanum phosphate electrolyte," *Solid State Ionics*, 178 (2007) 769-773

[22] Y. Abe, M. Hayashi, T. Iwamoto, H. Sumi, L.L. Hench, "Superprotonic conducting phosphate glasses containing water," *J. Non-Crystalline Solids*, 351 (2005) 2138-2141

[23] E. Metwalli, M. Karabulut, D.L. Sidebottom, M.M. Morsi, R.K. Brow, "Properties and structure of copper ultraphosphate glasses," *Journal of Non-Crystalline Solids*, 344(3), (2004) 128-134

[24] S.J. Pennycook, D.E. Jesson, "High-resolution Z-contrast imaging of crystals," *Ultramicroscopy*, 37 (1991) 14-38

[25] G. Metz, X. Wu, S.O. Smith, "Ramped-Amplitude Cross Polarization in Magic-Angle-Spinning NMR," *Journal of Magnetic Resonance, Series A*, 110 (1994), 219-227

[26] N. Zumbulyadis, "Hydrogen-silicon nuclear spin correlations in α-Si:H: A two-dimensional NMR Study," *Physical Review B*, 33 (1986) 6495-6496

[27] A.J. Vega, "Heteronuclear chemical-shift correlations of silanol groups studied by two-dimensional cross-polarization magic angle spinning NMR," *Journal of the American Chemical Society*, 110 (1988) 1049-1054

[28] K. Schmidt-Rohr, J. Clauss, and H.W. Spiess, "Correlation of structure, mobility, and morphological information in heterogeneous polymer materials by two-dimensional wideline-separation NMR spectroscopy," *Macromolecules*, 25 (1992) 3273-3277

[29] A.E. Bennett, R.G. Griffin, J.H. Ok, S. Vega, "Chemical shift correlation spectroscopy in rotating solids: Radio frequency-driven dipolar recoupling and longitudinal exchange," *Journal of Chemical Physics*, 1992, 96, 8624-8627

[30] T. Gullion, D.B. Baker, M.S. Conradi, "New, compensated Carr-Purcell sequences," *Journal of Magnetic Resonance*, 1990, 89, 479-484

[31] N. Kitamura, K. Amezawa, Y. Tomii, T. Hanada, N. Yamamoto, T. Omata, S. Otsuka-Yao-Matsuo, "Electrical conduction properties of Sr-doped $LaPO_4$ and $CePO_4$ under oxidizing and reducing conditions," *J. Electrochemical Soc.*, 152 (2005) A658-663

[32] N. Machida, Y. Shinkuma, T. Minami, "Structure and electrical properties of Cu^+ ion-conducting oxyhalide glasses in the system CuI-$CuPO_3$-Cu_2MoO_4," *Solid State Ionics*, 45 (1991) 123-129

[33] M. Watanabe, D.B. Williams, "The quantitative analysis of thin specimens: a review of progress from the Cliff-Lorimer to the new ζ-factor methods," *J. Microscopy*, 221 (2006) 89-109

[34] L.A.J. Garvie, P.R. Buseck, "Determination of Ce^{4+}/Ce^{3+} in electron-beam-damaged CeO_2 by electron energy-loss spectroscopy," *Journal of Physics and Chemistry of Solids,* 60 (1990) 1943-1947

[35] D. Zhu, W. Zhou, H. Zhao, "Composition analysis of glasses in the $PbBr_2$-$PbCl_2$-PbF_2-PbO-P_2O_5 system," *J. Non-Crystalline Solids*, 279 (2001) 204-208

[36] R.K. Brow, "Review: the structure of simple phosphate glasses," *Journal of Non-Crystalline Solids*, 263 & 264 (2000) 1-28

[37] L. Karpowich, S. Wilcke, R. Yu, G. Harley, J.A. Reimer, L.C. De Jonghe, "Synthesis and characterization of mixed-morphology $CePO_4$ particles," *Journal of Solid State Chemistry*, 180, (2007) 840-846

[38] M. Lopez Granados, F. Cabello Gallsteo, P.S. Lambrou, R. Mariscal, J. Sanz, I. Sobrados, J.L.G. Fierro, A.M. Efstathiou, "Role of P-containing species in phosphated CeO_2 in the deterioration of its oxygen storage and release properties," *Journal of Catalysis*, 239 (2006) 410-421

[39] B. Gee, C.R. Horne, E.J. Cairnes, J.A. Reimer, "Supertransferred hyperfine interactions at ^{7}Li: Variable temperature ^{7}Li NMR studies of $LiMn_2O_4$-based spinels," *Journal of Physical Chemistry B.*, 102, (1998) 10142-10149

[40] S.B. Adler, J.A. Reimer, "High-temperature ^{17}O NMR as a probe of electron localization and structure in transition metal oxides," *Solid State Ionics*, 91, (1996) 175-181

[41] W. S. Price, *NMR Studies of Translational Motion*, Cambridge Molecular Science, (2009).

[42] P. Callaghan, *Principles of nuclear magnetic resonance microscopy*, Oxford University Press, (1994).

[43] W. S. Price, "Pulsed-field gradient NMR as a tool for studying translational diffusion. Part I. Basic Theory," *Concepts in Magnetic Resonance*, 9, (1997), 299.

[44] W. S. Price, "Pulsed-field gradient NMR as a tool for studying translational diffusion. Part II. Experimental Aspects," *Concepts in Magnetic Resonance*, 10, (1998), 197.

[45] E. O. Stejskal, J. E. Tanner, "Spin diffusion measurements: Spin echoes in the presence of a time-dependent field gradient", *Journal of Chemical Physics*, 42(1), (1965), 288.

[46] W. S. Price, P. W. Kuchel, "Effect of Nonrectangular Field Gradient Pulses in the Stejskal and Tanner (Diffusion) Pulse Sequence," *Journal of Magnetic Resonance*, 94, (1991), 133.

[47] W. Zhang, D.G. Cory, "Pulsed gradient NMR probes for solid state studies," *Journal of Magnetic Resonance*, 132, (1998), 144-149.

[48] V. Demas, J. Herberg, V. Malba, A. Bernhardt, L. Evans, C. Harvey, S. Chinn, R. Maxwell, J. Reimer, "Portable, low-cost NMR with laser-lathe lithography produced microcoils," *Journal of Magnetic Resonance*, 189, (2007), 121-129.

[49] D.J. Tomlinson, "Temperature dependent self-diffusion coefficient of glycerol by the pulsed N.M.R. technique," *Molecular Physics*, 25(3), (1972), 735-738.

[50] D.S. Raiford, C.L. Fisk, E.D. Becker, "Calibration of methanol and ethylene glycol nuclear magnetic resonance thermometers," *Analytical Chemistry*, 51(12) (1979), 2050-2051.

[51] H. Carr, E. Purcell, "Effects of Diffusion on Free Precession in Nuclear Magnetic Resonance Experiements," *Phys.Rev.*, 94 (1954) 630.

[52] S. Meiboom, D. Gill, "Modified Spin-Echo Method for Measuring Nuclear Relaxation Times," *Rev.Sci.Ins.*, 29 (1958) 688.

[53] D.G. Rata, F. Casanova, J. Perlo, D. E. Demco, B. Bluemich, "Self-diffusion measurement by a mobile single-sided NMR sensor with improved magnetic field gradient," *Journal of Magnetic Resonance*, 180, (2006), 229

[54] R. Kimmich, E. Fischer, "One- and two-dimensional pulse sequences for diffusion experiments in the fringe field of superconducting magnets," *Journal of Magnetic Resonance*,106(2), (1994), 229.

[55] J. E. Tanner, "Use of the stimulated echo in NMR diffusion studies," *Journal of Chemical Physics*, 52, (1970), 2523.

[56] P.J. McDonald, "Stray field magnetic resonance imaging," *Progress in Nuclear Magnetic Resonance Spectroscopy*, 30, (1998), 69.

[57] G. Farrher, I. Ardelean, R. Kimmich, "Probing four orders of magnitude of the diffusion time in porous silica glass with unconventional NMR techniques," *Journal of Magnetic Resonance*, 182(2), (2006), 215.

[58] G. Harley, L.C. De Jonghe, "Proton transport in doped La-metaphosphate glasses," *Solid State Ionics*, 181(8-10), (2010), 424-429.

[59] G. Harley, K.D. Kreuer, J. Maier, L.C. De Jonghe, "Structural investigation of ternary La/alkaline earth phosphate ($La_{1-x}M_xP_3O_y$) (M = Ba, Ca, Sr) glasses," *Journal of Non-Crystalline Solids*, 355(16-17), (2009), 932-937.

[60] J. Kaerger, "NMR self-diffusion studies in heterogeneous systems," *Advances in Colloid and Interface Science*, 23, (1985), 129-148.

[61] E. Fischer, R. Kimmich, "Constant time steady gradient NMR diffusometery using the secondary stimulated echo," *Journal of Magnetic Resonance*, 166, (2004), 273-279.

[62] S.A. Mullin, G.M. Stone, A. Panday, N.P. Balsara, "Salt diffusion coefficients in block copolymer electrolytes," *J. Electrochemical Soc., 158(5), (2011), 1-9.*

[63] M. Singh, O. Odusanya, G.M. Wilmes, H.B. Eitouni, E.D. Gomez, A.J. Patel, V.L. Chen, M.J. Park, P. Fragouli, H. Iatrou, N. Hadjichristidis, D. Cookson, N.P. Balsara, "Effect of molecular weight on the mechanical and electrical properties of block copolymer electrolytes," Macromolecules, 40, (2007), 4578-4585.

[64] A. Panday, S. Mullin, E.D. Gomez, N. Wanakule, V. Chen, A. Hexemer, J. Pople, N.P. Balsara, "Effect of molecular weight and salt concentration on conductivity of block copolymer electrolytes," Macromolecules, 42, (2009), 4632-4637.

[65] N.S. Wanakule, J.M. Virgili, A.A. Teran, Z.G. Wang, N.P. Balsara, "Thermodynamic properties of block copolymer electrolytes containing imidazolium and lithium salts," Macromolecules, 43, (2010), 8282-8289.

[66] N.S. Wanakule, A. Panday, S.A. Mullin, E. Gann, A. Hexemer, N.P. Balsara, "Ionic conductivity of block copolymer electrolytes in the vicinity of order-disorder and order-order transitions," Macromolecules, 42, (2009), 5642-5651.

[67] E.D. Gomez, A. Panday, E.H. Feng, V. Chen, G.M. Stone, A.M. Minor, C. Kisielowski, K.H. Downing, O. Borodin, G.D. Smith, N.P. Balsara, "Effect of ion distribution on conductivity of block copolymer electrolytes," Nano Letters, 9(3), (2009), 1212-1216.

Appendix A

Mathematical Analysis of Typical Experimental NMR Data

This section describes the techniques used for fitting experimental nuclear magnetic resonance data.

A.1 Fitting Longitudinal Relaxation Data, T_1

A.1.1 Fitting Data from Inversion Recovery Data

There are two typical experiments used to measure T_1 in materials: The inversion recovery experiment and the saturation recovery experiment. From a mathematical fitting standpoint, the inversion recovery experiment is the more ideal, since the magnitude of the real signal passes through zero in a very well-defined way. The expected equation for an inversion recovery experiment in which a single T_1 is observed is

$$M(t) = M_0(1 - 2Exp(\frac{-t}{T_1})) \tag{A.1}$$

Such pulse sequences can be often be fit using the software that comes with the spectrometer (Tecmag's NTNMR, etc), but these programs often hide the underlying fitting process from the user in an effort to simplify the process of analysis for the user. To fit the data using a nonlinear regression package, generally the area of the peak can be integrated for analysis in order to improve the signal to noise, which is often a more serious constraint when performing experiments on solid state samples versus liquids. The model to be used when fitting is

$$S(t) = M_0(1 - 2Exp(\frac{-t}{T_1})) + \epsilon$$

This is identical to the expected equation above, except that it includes a term ϵ for any experimental artifacts introduced during the acquisition of NMR signal by the instrument. The inclusion of ϵ is almost always necessary when a baseline offset is present in the acquired NMR data, and even slight baseline offsets can be magnified when integrating peaks in solid state spectra. ϵ is generally

assumed to be time independent, although this may not be the case. Distributing the product in the above model equation gives

$$S(t) = M_0(1 - 2Exp(\frac{-t}{T_1})) + \epsilon \tag{A.2}$$

$$= M_0 - 2M_0Exp(\frac{-t}{T_1}) + \epsilon \tag{A.3}$$

One could try to use a nonlinear regression package to fit this model equation to the data, but the software package will often have a harder time fitting the three parameters (M_0, T_1, and ϵ) than two, so the model can be simplified to

$$M(t) = A - B \cdot Exp(\frac{-t}{T_1}) \tag{A.4}$$

where A = (M_0+ϵ) and B = 2M_0. Generally the researcher is only interested in T_1. In cases in which the researcher is interested in T_1 as a means of understanding the underlying processes taking place in the system (and not just determining 5T_1 for experimental recycle delays), nearly every nonlinear regression program can generate a confidence interval for the fitted T_1 value.

For fitting a two-T_1 system, a second population and T_1 can be added to the equations given above. The expected equation for such a system is

$$M(t) = M_{0,1}(1 - 2Exp(\frac{-t}{T_{1,1}})) + M_{0,2}(1 - 2Exp(\frac{-t}{T_{1,2}})) \tag{A.5}$$

To this equation, we can add an error term to again account for any experimental artifacts in our data:

$$M(t) = M_{0,1}(1 - 2Exp(\frac{-t}{T_{1,1}})) + M_{0,2}(1 - 2Exp(\frac{-t}{T_{1,2}})) + \epsilon$$

And we can again distribute the terms in this equation and then simplify for the nonlinear regression model:

$$S(t) = M_{0,1}(1 - 2Exp(\frac{-t}{T_{1,1}})) + M_{0,2}(1 - 2Exp(\frac{-t}{T_{1,2}})) + \epsilon \tag{A.6}$$

$$= M_{0,1} - 2M_{0,1}Exp(\frac{-t}{T_{1,1}}) + M_{0,2} - 2M_{0,2}Exp(\frac{-t}{T_{1,2}}) + \epsilon \tag{A.7}$$

$$= A - BExp(\frac{-t}{T_{1,1}}) - CExp(\frac{-t}{T_{1,2}}) \tag{A.8}$$

where A = ($M_{0,1}$+$M_{0,2}$+ϵ), B = 2$M_{0,1}$ and C = 2$M_{0,2}$, reducing a five-parameter fit to four. Systems with more T_1 populations can be fit as well, but each additional population requires an additional 2 parameters which can decrease confidence in all fit values. Because the researcher often has spectroscopic resolution to assist in separation of the fitting, this often is not the problem. In cases where there is little or no spectroscopic resolution and a large number of T_1s are present, Laplacian Inversion is probably a more useful tool for characterizing the longitudinal relaxation parameters of the system.

An example of a single and double T_1 fit from an inversion recovery experiment performed in Mathematica is given at the end of this appendix.

A.1.2 Fitting Saturation Recovery Data

In cases in which T_1 is too long to complete an inversion recovery pulse sequence in a reasonable timeframe, the saturation recovery experiment can be used because it does not required a 5*T_1 delay at the end of each cycle in the pulse sequence. The saturation recovery experiment has experimental subtleties that complicate matters - ensuring complete saturation often being the most difficult - that complicate the mathematical analysis if not done properly. Furthermore, because the magnitude of the real peak does not pass through zero, small amounts of noise from the NMR spectrometer can have a large effect on the calculated T_1. Assuming the experiment is done properly, the expected equation for an saturation recovery experiment in which a single T_1 is observed is

$$M(t) = M_0(1 - Exp(\frac{-t}{T_1})) \tag{A.9}$$

The saturation recovery pulse sequence is less common and it is less likely that a commercial NMR spectrometer software will include a process to automatically fit the data for the user. To fit the data using a nonlinear regression package, generally the area of the peak can be integrated for analysis in order to improve the signal to noise, which is often a more serious constraint when performing experiments on solid state samples versus liquids. The model to be used when fitting is

$$S(t) = M_0(1 - Exp(\frac{-t}{T_1})) + \epsilon$$

This is identical to the expected equation above, except that it includes a term ϵ for any experimental artifacts introduced during the acquisition of NMR signal by the instrument. The inclusion of ϵ is almost always necessary when a baseline offset is present in the acquired NMR data, and even slight baseline offsets can be magnified when integrating peaks in solid state spectra. ϵ is generally assumed to be time independent, although this may not be the case. Distributing the product in the above model equation gives

$$S(t) = M_0(1 - Exp(\frac{-t}{T_1})) + \epsilon \tag{A.10}$$

$$= M_0 - M_0 Exp(\frac{-t}{T_1}) + \epsilon \tag{A.11}$$

One could try to use a nonlinear regression package to fit this model equation to the data, but the software package will often have a harder time fitting the three parameters (M_0, T_1, and ϵ) than two, so the model can be simplified to

$$M(t) = A - BExp(\frac{-t}{T_1}) \tag{A.12}$$

where A = (M_0+ϵ) and B = M_0. (Interestingly, the model equation used for fits in both the inversion recovery and saturation recovery experiments is identical, even though the governing equation of the system is different. The value of $\frac{A}{B}$ should be rather close to 1 in the case of the saturation recovery and close to 1/2 in the inversion recovery.) Generally the researcher is only interested in T_1. In cases in which the researcher is interested in T_1 as a means of understanding the

underlying processes taking place in the system (and not just determining 5*T_1 for experimental recycle delays), nearly every nonlinear regression program can generate a confidence interval for the fitted T_1 value.

For fitting a two-T_1 system, a second population and T_1 can be added to the equations given above. The expected equation for such a system is

$$M(t) = M_{0,1}(1 - Exp(\frac{-t}{T_{1,1}})) + M_{0,2}(1 - Exp(\frac{-t}{T_{1,2}})) \tag{A.13}$$

To this equation, we can add an error term to again account for any experimental artifacts in our data:

$$M(t) = M_{0,1}(1 - Exp(\frac{-t}{T_{1,1}})) + M_{0,2}(1 - Exp(\frac{-t}{T_{1,2}})) + \epsilon$$

And we can again distribute the terms in this equation and then simplify for the nonlinear regression model:

$$S(t) = M_{0,1}(1 - Exp(\frac{-t}{T_{1,1}})) + M_{0,2}(1 - Exp(\frac{-t}{T_{1,2}})) + \epsilon \tag{A.14}$$

$$= M_{0,1} - M_{0,1}Exp(\frac{-t}{T_{1,1}}) + M_{0,2} - M_{0,2}Exp(\frac{-t}{T_{1,2}}) + \epsilon \tag{A.15}$$

$$= A - BExp(\frac{-t}{T_{1,1}}) - CExp(\frac{-t}{T_{1,2}}) \tag{A.16}$$

where A = ($M_{0,1}$+$M_{0,2}$+ϵ), B = $M_{0,1}$ and C = $M_{0,2}$, reducing a five-parameter fit to four. Systems with more T_1 populations can be fit as well, but each additional population requires an additional 2 parameters which can decrease confidence in all fit values. Because the researcher often has spectroscopic resolution to assist in separation of the fitting, this often is not the problem. In cases where there is little or no spectroscopic resolution and a large number of T_1s are present, Laplacian Inversion is probably a more useful tool for characterizing the longitudinal relaxation parameters of the system.

An example of a single and double T_1 fit from a saturation recovery experiment performed in Mathematica is given at the end of this appendix.

A.2 Fitting Spin-Spin Relaxation Data, T_2

The spin-spin relaxation constant, T_2, is generally measured by a variable delay spin echo experiment or a Carr-Purcell-Meiboom-Gill (CPMG) experiment. The fit equation for the two experiments is the same, but careful attention must be payed to how the delays are inserted into the fit algorithm. Most NMR spectrometer software allows one to calculate a T_2 based on the results of a variable delay spin echo experiment, but they often have program-specific requirements for how the data is entered (e.g., all time values must have the same units in NTNMR, etc.). In order to emphasis the care one should take when developing the correlation between signal intensity and time, the two experiments will be discussed separately.

A.2.1 Fitting Spin Echo Data

For a spin echo experiment (90-τ-180-τ-acquire) with a variable τ and a single T_2, the expected equation for the system is

$$M(t) = M_0 Exp(\frac{-2 * \tau}{T_2})) \tag{A.17}$$

To fit the data using a nonlinear regression package, generally the area of the peak can be integrated for analysis in order to improve the signal to noise, which is often a more serious constraint when performing experiments on solid state samples versus liquid samples. The model to be used when fitting is

$$S(t) = M_0 Exp(\frac{-2\tau}{T_2}) + \epsilon$$

or equivalently

$$S(t) = AExp(\frac{-2\tau}{T_2}) + B$$

Thus three parameters should generally be used to fit the data using a nonlinear regression package. In cases where it is known that experimental artifacts (ϵ or B in the two equations above) is nearly zero, T_2 can be fit using ordinary linear regression by plotting the data on a semi-log plot with only two parameters. Is it usually wise to confirm that a semi-log plot is appropriate by comparing the results with a three parameter nonlinear fit. If the results are statistically different, the baseline offset found by the three parameter nonlinear fit can be subtracted from the signal data and then the semi-log plot and fit can be applied.

For a system in which two T_2s are expected, the expected equation for the system

$$M(t) = M_{0,1} Exp(\frac{-2\tau}{T_{2,1}})) + M_{0,2} Exp(\frac{-2\tau}{T_{2,2}})) \tag{A.18}$$

To fit the data using a nonlinear regression package, generally the area of the peak can be integrated for analysis in order to improve the signal to noise, which is often a more serious constraint when performing experiments on solid state samples versus liquid samples. The model to be used when fitting is

$$S(t) = M_{0,1} Exp(\frac{-2\tau}{T_{2,1}})) + M_{0,2} Exp(\frac{-2\tau}{T_{2,2}})) + \epsilon$$

or equivalently

$$S(t) = AExp(\frac{-2\tau}{T_{2,1}})) + BExp(\frac{-2\tau}{T_{2,2}})) + C$$

This five parameter model can be used to fit the data in a nonlinear regression package. Systems with more T_2 populations can be fit as well, but each additional population requires an additional 2 parameters which can decrease confidence in all fit values. Because the researcher often has spectroscopic resolution to assist in separation of the fitting, this often is not the problem. In cases where there is little or no spectroscopic resolution and a large number of T_2s are present, Laplacian Inversion is probably a more useful tool for characterizing the longitudinal relaxation parameters of the system.

An example of a single and double T_2 fit from spin echo experiments performed in Mathematica is given at the end of this appendix.

A.3 Fitting NMR Spectra for Line Shape Analysis

Finding the chemical shifts and peak peak intensities for high resolution liquid state NMR spectra is generally sufficiently straightforward that it can be done in the acquisition window of the spectrometer. Extracting the same information for fitting solid state NMR spectra can be much more difficult. While in principle the NMR spectrum of a solid sample provides a wealth of information, it is often the case that there is simply far too much information for simples in which multiple nuclear spin environments or - also common - a distribution of nuclear spin environments are present. A common first step to understanding the nuclear spin environments is to perform a direct excitation experiment in hopes of observing and assigning chemical shift environments in the sample. In order to simplify this task, magic angle spinning (MAS) NMR is often used to remove (sufficiently weak) dipolar interactions and chemical shift anisotropy, allowing the typically broad lines to narrow so that only isotropic chemical shifts are observed. Once these chemical shifts are observed, other parts of the nuclear spin Hamiltonian may be selectively reintroduced to understand the relationship between the spins observed in the direct excitation MAS NMR experiment and their environment. Even when direct excitation MAS NMR is being used, understanding the isotropic chemical shifts is often no easy task. This section describes one methodology - the one used elsewhere in this work - to perform a line shape analysis on the resulting MAS NMR spectrum.

There are several line shapes that can be used to describe NMR peaks observed in MAS NMR spectra. The most common are Lorentzian line shapes, which are used to describe liquids and some crystalline solids, and Gaussian line shapes, which are used to describe disordered solids and some crystalline solids. These line shapes are generally used in the frequency domain, where the center of the peak will describe the chemical shift of that peak, the width of the peak will be related to the peak width (often reported as full width at half height, FWHH), and the peak area will be related to the number of nuclei that that experience that chemical shift environment. The absorption Lorentzian line shape is

$$S[\omega] = \frac{\lambda}{\lambda^2 + (\omega - \omega_0)^2}$$

The FWHH for this line shape is 2λ, the peak center is at Ω_0, and the integrated area of this equation is π. Because the relative population of different peaks is of interest, an additional variable corresponding to peak area will be of interest in the peak. The modified equation will then be:

$$S[\omega] = A\frac{\lambda}{\lambda^2 + (\omega - \omega_0)^2}$$

We will introduce a second variable, B, to account for any baseline offsets in the NMR spectrum:

$$S[\omega] = A\frac{\lambda}{\lambda^2 + (\omega - \omega_0)^2} + B$$

When a line shape analysis is to be performed using a nonlinear regression algorithm on a peak with a Lorentzian line shape, the data will be entered as a function of ω, and the parameters A, B, ω_0 and λ will be fit.

The absorption Gaussian line shape is

$$S[\omega] = Exp(-\frac{(\omega - C)^2}{2W^2})$$

The FWHH for this line shape is $2\mathrm{W}\sqrt{2\ln 2}$ which is approximately equal to $2.3548W$. The center of the Gaussian is C and the integrated area of this equation is $\frac{1}{\sqrt{2\pi W^2}}$. Because the relative population of different peaks is of interest, an additional variable corresponding to peak area will be of interest in the peak. The modified equation will then be:

$$S[\omega] = AExp(-\frac{(\omega - C)^2}{2W^2})$$

When reporting populations, it is important to realize that A will need to be divided by $\frac{1}{\sqrt{2\pi W^2}}$ in order to accurately reflect the relative populations in the sample. Alternatively, the area under the fitted peak can be determined and compared to a standard in order to provide a quantitative detection of the number of spins. We will introduce a second variable, B, to account for any baseline offsets in the NMR spectrum:

$$S[\omega] = AExp(-\frac{(\omega - C)^2}{2W^2}) + B$$

When a line shape analysis is to be performed using a nonlinear regression algorithm on a peak with a Gaussian line shape, the data will be entered as a function of ω, and the parameters A, B, C and W will be fit.

To fit spectra when more than one peak, the model equation will be a sum of line shapes, each of which represent one of the peaks in the spectrum to be fit. It is more common to observe that all peaks in a spectrum have the same line shape form. From a line shape analysis perspective, it is just as easy to fit a mix of Gaussian and Lorentzian peaks as it is to fit multiple peaks of the same line shape form. To fit a spectrum with n peaks, the model equation that describes the system will be

$$S[\omega] = \sum_{i=1}^{n} S_i[\omega] + B$$

where $S[\omega]$ is the NMR spectrum observed by the NMR experiment with n peaks and each $S_i[\omega]$ for i = 1, 2, 3... n is one of the n peaks in the spectrum. So if one is interested in fitting a spectrum with three peaks that each are best described by a Gaussian, the model equation that describes the system will be

$$S[\omega] = A_1Exp(-\frac{(\omega - C_1)^2}{2W_1^2}) + A_2Exp(-\frac{(\omega - C_2)^2}{2W_2^2}) + A_3Exp(-\frac{(\omega - C_3)^2}{2W_3^2}) + B$$

One the nonlinear regression is performed on the NMR data, peak one will be best described by (A_1, C_1, W_1), peak two will be best described by (A_2, C_2, W_2) and peak three will be best described by (A_3, C_3, W_3). This example illustrates that the number of parameters to fit for a spectrum with n peaks will be 3n+1 when one is using this approach to line shape analyses.

Although it is generally straightforward to identify the approximate center and line width of a NMR peak when peaks are isolated, the usefulness of a line shape analysis quickly becomes apparent in cases with significantly overlapping lines or when one wishes to measure small changes in chemical shift of broad lines. The example of a line shape analysis performed in Mathematica given at the end of this appendix demonstrates a particularly challenging case in which one is working to fit six overlapping peaks in which the center of each peak (i.e., the chemical shift) is of importance.

A.4 Fitting Field Gradient Diffusion Data

There are numerous field gradient NMR pulse sequences that can be used to measure self diffusion in experimental systems on a variety of time scales. There are two general categories of field gradient experiments: Those in which the field gradient is time dependent and those in which the field gradient does not change with time during the course of the NMR experiment. Time dependent field gradient experiments generally are applied as pulses, and so-called Pulsed Gradient NMR experiments are very straightforward because the magnitude of the pulsed gradient is changed during the course of the experiment to probe the self-diffusion of the mobile species. Because the only experimental parameter changing during the experiment, NMR relaxation can generally be ignored during the data analysis of the experimental data, provided the experiment has been setup properly. Time independent field gradient experiments, which consist of steady gradient, STRAy FIeld (STRAFI) and Fringe Field NMR experiments, are generally more challenging because a time delay is the variable that is changing during the course of the experiment. As a result, there is not always a well-defined diffusion time during the experiment (rather, there is a diffusion time range) and one must carefully consider relaxation going on during the course of the experiment. There are some pulse sequences that attempt to create a well-defined diffusion time[4], which can be very useful for understanding the medium through which mobile or conducting moieties are moving. The most typical pulse sequences and fit equations for diffusion and relaxation are shown in Figure 5.1 and in Table 5.1.

A.4.1 Pulsed Gradient Spin Echo Experiment with Square Pulses

The most typical of pulse sequences that is used is the Pulsed Gradient Spin Echo experiment (Experiment I-a in Figure 5.1). If the experiment is set up properly (one decade of signal attenuation is seen, the timescale of self diffusion is shorter than T_2 for all peaks under investigation, and a recycle delay of $5T_1$ is used for the experiment), then the expected signal attenuation as a function of gradient strength is

$$S(G)/S(G=0) = Exp(-\gamma_n^2 G^2 D\delta^3(\frac{\Delta}{\delta} - \frac{1}{3})) \tag{A.19}$$

In cases where a the system under investigation is a liquid with very good signal to noise and minimal experimental artifacts, this data can be simply fit as a linear regression of Ln[S(G)/S(G=0)] (that is, the natural log of normalized signal intensity) versus $-\gamma_n^2 G^2 \delta^3(\frac{\Delta}{\delta} - \frac{1}{3})$. If there is only one self-diffusion coefficient present in the system under investigation, the resulting data will be linear with

a slope of -D. In systems that may have poor signal to noise (because the mobile component under investigation is dilute), or if experimental artifacts are significant, the resulting peaks will likely need to be integrated or fit using a line shape analysis in order to minimize the noise introduced by the experimental apparatus itself. In these cases, the model equation to be used is

$$S(G) = S(G=0)Exp(-\gamma_n^2 G^2 D\delta^3(\frac{\Delta}{\delta} - \frac{1}{3})) + \epsilon$$

which can be simplified to

$$S(G) = AExp(-\gamma_n^2 G^2 D\delta^3(\frac{\Delta}{\delta} - \frac{1}{3})) + B$$

This fit can easily be performed using nonlinear regression package, and the magnitude of B can indicate the degree to which baseline offset errors are contributing to the signal intensity. In cases where one would prefer to report the attenuation profile on a plot of Ln[S(G)/S(G=0)] versus $-\gamma_n^2 G^2 \delta^3(\frac{\Delta}{\delta} - \frac{1}{3})$, one can simply subtract B from each of the S(G) data, and process the data as above.

An example of a self diffusion coefficient fit from a pulsed gradient spin echo experiment with square gradient pulses performed in Mathematica is given at the end of this appendix.

A.4.2 Pulsed Gradient Spin Echo Experiment with Sinusoidal Pulses

In cases where gradient ring down is a significant problem, shaped gradient pulses can be used [46]. Because the gradient coils generally have a fair amount of inductance, the gradient ring down can be minimized by minimizing dI/dt at the end of the gradient pulse. Square pulses are generally the worst pulse shapes for gradient ring down, but they still are used frequently because of the mathematical simplicity of the relationship between experimental parameters and the resulting experimental data. The use of sine-shaped gradient pulses greatly reduce dI/dt compared to the square pulse at the beginning of the gradient pulse (minimize gradient shape issues) and at the end of the pulse, where gradient ring down takes place. (Other gradient shapes, such as exponential and Sin^2 shapes can also be used **??**, although the fit equations presented here will be different). The fit equation for a pulsed gradient spin echo experiment with sine gradient pulses (essentially Experiment I-a in Figure 5.1 but with the square pulses replaced with a sine pulse) will be

$$S(G)/S(G=0) = Exp(-\gamma_n^2 G^2 D\delta^2[3\delta Cos^2(\frac{N\pi}{2}) + (4\Delta - \delta)Sin^2(\frac{N\pi}{2})]/(N\pi)^2 \qquad \text{(A.20)}$$

In practice, one would only use one half of a period of a sine pulse. For this situation this equation simplifies to

$$S(G)/S(G=0) = Exp(-\gamma_n^2 G^2 D\delta^2[3\delta Cos^2(\frac{\pi}{2}) + (4\Delta - \delta)Sin^2(\frac{\pi}{2})]/(\pi)^2 \qquad \text{(A.21)}$$

As in the case of the pulses gradient spin echo experiment with square pulses, if the system under investigation is a liquid with very good signal-to-noise and minimal experimental artifacts, this data can be simply fit as a linear regression with a semi-log plot. If there is only one self-diffusion

coefficient present in the system under investigation, the data can be plotted so the resulting fit will be linear with a slope of -D. In systems that may have poor signal to noise (because the mobile component under investigation is dilute), or if experimental artifacts are significant, the resulting peaks will likely need to be integrated or fit using a line shape analysis in order to minimize the noise introduced by the experimental apparatus itself. In these cases, the model equation to be used is

$$S(G) = S(G=0)Exp(-\gamma_n^2 G^2 D\delta^2[3\delta Cos^2(\frac{\pi}{2}) + (4\Delta - \delta)Sin^2(\frac{\pi}{2})]/(\pi)^2 + \epsilon$$

which can be simplified to

$$S(G) = AExp(-\gamma_n^2 G^2 D\delta^2[3\delta Cos^2(\frac{\pi}{2}) + (4\Delta - \delta)Sin^2(\frac{\pi}{2})]/(\pi)^2 + B$$

This fit can easily be performed using nonlinear regression package, and the magnitude of B can indicate the degree to which baseline offset errors are contributing to the signal intensity. In cases where one would prefer to report the attenuation profile on a plot of Ln[S(G)/S(G=0)] versus $-\gamma_n^2 G^2 \delta^3(\frac{\Delta}{\delta} - \frac{1}{3})$, one can simply subtract B from each of the S(G) data, and process the data as above.

An example of a self diffusion coefficient fit from a pulsed gradient spin echo experiment with sinusoidal gradient pulses performed in Mathematica is given at the end of this appendix.

A.4.3 Steady Gradient Spin Echo Experiment

The typical experiment done for systems in which the relative timescales of diffusion and relaxation requires a very large gradient is the Steady Gradient Spin Echo Experiment (also referred to as STRAFI or Fringe Field NMR). These experiments all have the same basic pulse sequence described by IIa in Figure 5.1 and in Table 5.1 and differ only in how the gradient is created. Because the magnetic field is intentionally inhomogeneous, there will generally be no spectroscopic resolution for these experiments which will complicate matters if more than one diffusion coefficient is present. Furthermore, because the gradient is not changing with time during the experiment, the variable parameter in this experiment is time, which mean that relaxation will also be an important factor in the fitting of this data. The expected equation describing the resulting data from this experiment will be

$$S(G)/S(G=0) = Exp(-\frac{2}{3}\gamma_n^2 G^2 D\tau^3)Exp(\frac{2\tau}{T_2}) \tag{A.22}$$

The T_2 in this equation can usually measured separately and thus entered as a constant in this equation, or it can be left as a variable if it is not yet known or in some cases where there is concern that it is changing with time. The T_2 of the mobile component in these systems is often related to the self diffusion of this component, so if T_2 is to be fixed during the fitting of the data, it must be measured for each temperature at which a steady gradient spin echo experiment is to be performed and analyzed. Performing the analysis with a fixed T_2 reduces one degree of freedom in the calculation, which is usually not necessary for systems with a single self diffusion coefficient, but becomes much more useful when there are at least two self diffusion coefficients.

To fit the data from a steady gradient spin echo experiment, the model equation will be

$$S(G) = S(G=0)Exp(-\frac{2}{3}\gamma_n^2 G^2 D\tau^3)Exp(\frac{2\tau}{T_2}) + \epsilon$$

which can be simplified to

$$S(G) = AExp(-\frac{2}{3}\gamma_n^2 G^2 D\tau^3)Exp(\frac{2\tau}{T_2}) + B$$

This fit can easily be performed using nonlinear regression package provided that the field gradient used in the experiment, G, is selected such that the timescale of diffusion is shorter than that of T_2 relaxation. If the timescales are too close to one another, then the fit program will have a difficult time determining the self diffusion coefficient and the uncertainty will be large.

To extend this analysis to systems with additional self-diffusion coefficients, the model equation can be changed to reflect the particulars of the system. In some cases, the T_2 of the components can be close enough to lump all of the T_2s into a single T_2 for the entire system. In other cases, each component will have a separate T_2, and each additional component will have a parameter reflecting population, self diffusion coefficient, and T_2 (if unknown). Only one parameter in the equation is needed to account for baseline artifacts.

An example of a single self diffusion coefficient fit from a steady gradient spin echo experiment and an example of a two self diffusion coefficient fit with a single T_2 from a steady gradient spin echo experiment performed in Mathematica is given at the end of this appendix.

Appendix B

Diffusion Studies in Polymer Systems

This appendix describes preliminary pulsed field gradient experiments performed on a polymer-LiTFSI system. This system provided an interesting investigation into the self diffusion coefficients of the Li^+ cation and TFSI anion in differing molecular weight polymer systems while also providing an opportunity to develop reliable pulse sequences, such as the pulsed gradient stimulated echo (PGStE) experiment and the application of sinusoidal gradients for gradient ring down suppression, for the study of self diffusion on a homebuilt NMR system.

B.1 Methods

Samples were prepared by Scott Mullin in the group of Professor Nitash Balsara in the Chemical Engineering Department at UC Berkeley. The samples consist of a polystyrene block and a polyethylene oxide block; the samples are summarized in Table B.1, and discussed extensively in [62, 63, 64, 65, 66, 67]. All of the SEO samples are lamellar. The PEO sample is unstructured and is used as a reference. For all studies, a sample was prepared in a 5 mm NMR tube in a glove box that was well sealed for the duration of the experiments. The samples are all non-crystalline at 90°C, the primary temperature of interest for these samples. The lithium bis(trifluoromethansulfone)imide (LiTFSI) salt concentration used was r = [Li]/[EO] = 0.085.

Table B.1: A summary of the co-block polymers studied in this work with the molecular weights of the polystyrene and polyethylene oxide blocks. All of the SEO samples are lamellar. The PEO sample, used as a reference compound, is unstructured.

Sample Name	**MW PS Block (kg/mol)**	**MW PEO Block (kg/mol)**
SEO4	40	54
SEO5	74	98
SEO6	16	16
SEO2	1.7	1.4
PEO	0	27

All diffusion experiments were performed using a Doty DSI-1302 PFG/Diffusion Z Gradient NMR Probe with H/X/lock channels. ^{7}Li NMR experiments were performed on the X channel at a field of 7.05 T at a frequency of 116 MHz. $\frac{\pi}{2}$ and π *rf* pulses of 12 and 24μs were used in all experiments. ^{19}F NMR experiments were performed on a 65.6 MHz magnet at a frequency of 62 MHz. $\frac{\pi}{2}$ and π *rf* pulses of 12 and 24μs were used in all experiments. All gradient calibrations were performed using glycerol at 25°C at the relevant proton frequency for the magnet being used.

Pulsed gradient spin echo (PGSE) experiments with square gradient pulses were used for short diffusion time studies, and the resulting data were fit with the following model equation:

$$S(G)/S(0) = Exp(-\gamma_n^2 G^2 D\delta^3(\frac{\Delta}{\delta} - \frac{1}{3})) + \epsilon$$

Pulsed gradient spin echo experiments with sinusoidal gradient pulses were used to minimize gradient ring down for short diffusion time studies in which the T_2 was a limiting factor in the experiment, and the resulting data were fit with the following model equation:

$$S(G)/S(0) = Exp(\frac{-\gamma_n^2 G^2 D\delta^2 3\delta(Cos^2(\frac{\pi}{2}) + (4\Delta - \delta)Sin^2(\frac{\pi}{2})}{\pi^2}) + \epsilon$$

Pulsed gradient stimulated echo (PGStE) experiments with sinusoidal gradient pulses were used to minimize gradient ring down time (so the amount of T_2 relaxation could be minimized) while probing longer diffusion times during the experiment, and the resulting data was fit with same modeling equation above. Although the governing equations for self diffusion are the same, the relaxation parameters and signal to noise in the stimulated echo experiment are different than in the spin echo experiment. This is primarily an issue when optimizing the parameters for a diffusion experiment.

B.2 Results of ^{7}Li Experiments in Annealed and Non-Annealed SEO4

To probe the effects of polymer annealing on the mobility of the lithium cation, variable temperature T_1, T_2 and self diffusion experiments were performed on a annealed and non-annealed SEO4 sample from 60 to 130°C. Over this range, no statistical change in the T_2 was observed. The T_1 of both the annealed and non-annealed sample had a strong but statistically identical dependence upon temperature, depicted in Figure B.1.

Pulsed gradient spin echo experiments (PGSE) with square pulses and a diffusion time of 18 ms were performed with a recycle delay of $5T_1$ as measured at each temperature. Tables B.3 and B.4 depicts the self diffusion coefficient of the lithium ion in both the annealed and the non-annealed samples as a function of temperature. As expected for these samples, the self diffusion coefficient increases as a function of temperature. If this data is plotted as a function of natural log of the self diffusion coefficient versus 1000/T in absolute temperature units, the data can be fit to an Arrhenius model of temperature-dependent self diffusion, and the activation energy of lithium ion motion can be extracted. As can be seen in Figure B.2, the activation energy of the lithium motion is statistically the same for both samples, although the self diffusion mobility of the non-annealed

Table B.2: The ^{7}Li T_1 in the annealed and non-annealed SEO4 polymer sample is displayed as a function of temperature.

Temperature (°C)	**Annealed T_1 (s)**	**Non-Annealed T_1 (s)**
60	0.27 +/- 0.01	0.253 +/- 0.009
70	0.28 +/- 0.01	0.283 +/- 0.008
80	0.32 +/- 0.02	0.32 +/- 0.02
90	0.36 +/- 0.02	0.37 +/- 0.02
100	0.40 +/- 0.02	0.41 +/- 0.03
110	0.52 +/- 0.02	0.52 +/- 0.02
120	0.60 +/- 0.03	0.60 +/- 0.03
130	0.61 +/- 0.03	0.70 +/- 0.03

Table B.3: The self diffusion coefficient of the $^7Li^+$ cation in the annealed SEO4 polymer is displayed as a function of temperature for a single diffusion time, $\Delta = 0.018124$ ms. The root mean squared displacement, or diffusion distance, is also reported.

Temperature (°C)	**^{7}Li Self Diffusion Coefficient,** $10^{-12}m^2s^{-1}$	**Diffusion Distance, nm**
60	0.69 +/- 0.04	158.
70	0.94 +/- 0.04	184.
80	1.29 +/- 0.04	215.
90	2.06 +/- 0.06	273.
100	2.12 +/- 0.06	277.
110	2.8 +/- 0.1	317.
120	3.1 +/- 0.1	338.
130	4.2 +/- 0.1	390.

SEO4 sample is consistently higher than that of the annealed sample. This is strongly suggestive of an entropic difference between the two samples, which is expected, since the annealing process serves to introduce order to the polymer sample. The activation energy calculated in the Annealed sample is 28 +/- 2 kJ/mol and that calculated from the Non-Annealed sample is 27 +/-3 kJ/mol.

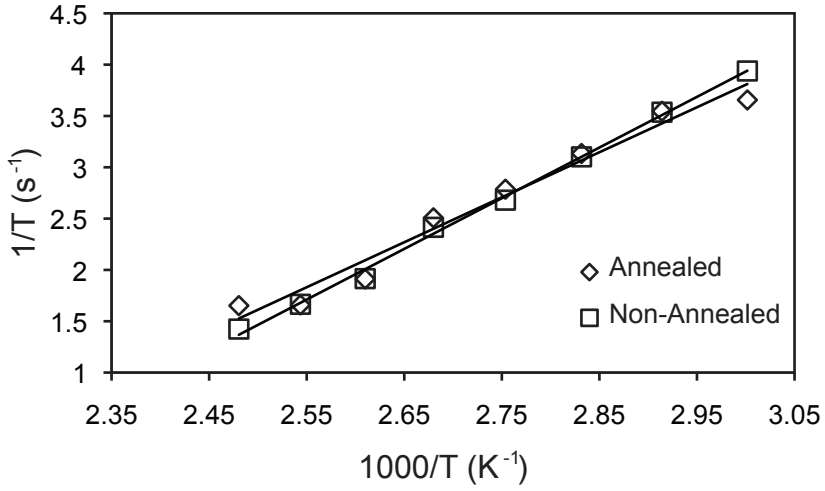


Figure B.1: The inverse of T_1 of ^{7}Li in the Annealed and Non-Annealed SEO4 polymer is displayed as a function of 1000/T in absolute temperature units. The slopes of the linear regression best fits through the data - that of the Annealed data is 4.6 +/- 0.6 and the slope of the Non-Annealed sample is 4.9 +/- 0.3 - are statistically the same, indicating that there is no difference in T_1 behavior for the two samples.

Table B.4: The self diffusion coefficient of the $^7Li^+$ cation in the non-annealed SEO4 polymer is displayed as a function of temperature for a single diffusion time, $\Delta = 0.018124$ ms. The root mean squared displacement, or diffusion distance, is also reported.

Temperature (°C)	**^{7}Li Self Diffusion Coefficient,** $10^{-12}m^2s^{-1}$	**Diffusion Distance, nm**
60	0.84 +/- 0.05	174.
70	1.13 +/- 0.04	203.
80	1.60 +/- 0.06	241.
90	2.2 +/- 0.1	284.
100	3.10 +/- 0.08	335.
110	3.15 +/- 0.09	338.
120	3.9 +/- 0.1	377.
130	4.6 +/- 0.1	409.

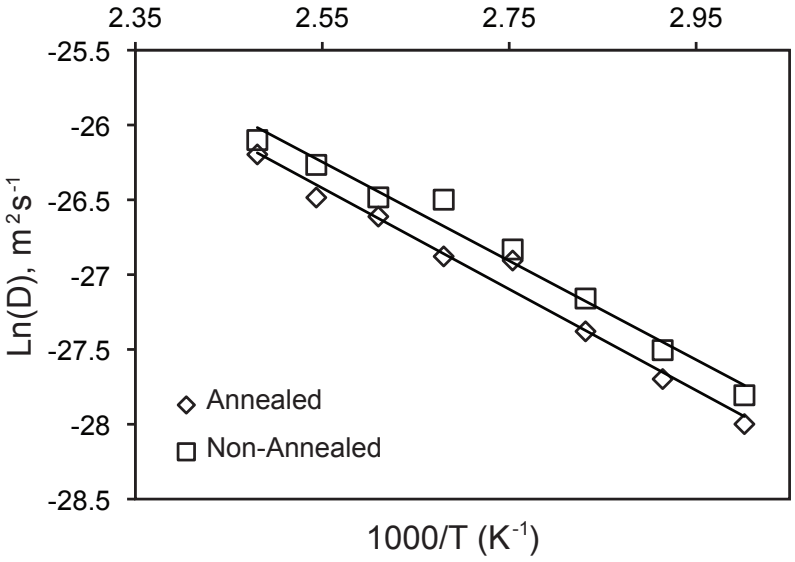


Figure B.2: The natural logarithm of the ^{7}Li self diffusion coefficientin the Annealed and Non-Annealed SEO4 polymer is displayed as a function of 1000/T in absolute temperature units. The slopes of the linear regression best fits through the data are statistically the same, indicating that they have the same activation energy associated with lithium transport through the materials, but a step offset in the self diffusion coefficients between the two samples indicates that the Non-Annealed sample has a higher self diffusion coefficient at any given temperature than does the Annealed sample. The slope of the Annealed data is 3.4 +/- 0.2 and that of the Non-Annealed data is 3.3 +/- 0.4, which correspond to activations of 28 +/- 2 and 27+/- 3 kJ/mol, respectively.

B.3 Results of Variable Diffusion Time ^{7}Li Self Diffusion Experiments

Variable diffusion time experiments provide an opportunity to measure the effective self diffusion coefficient over different time scales. As the diffusion time of the experiment increases, the mobile species is allowed more time to probe more of the local environment. The range of diffusion times is limited by the relaxation parameters of the NMR experiment and generally is less than one second. For simple systems, such as liquids, no change in self diffusion coefficient will be observed during the time scales allowed by NMR because the length scale of the sample container (e.g., an NMR tube) is much greater than the length scales being probed by the molecules. In samples that contain restrictions, the self diffusion coefficient will generally be faster at shorter diffusion times, when the mobile species has very little time to interact with any restrictions, and will gradually decrease at longer times as a higher and higher percentage of the mobile species must interact with the restrictions. As a result, these variable diffusion time experiments provide a diffusing species-perspective of the restrictions or interactions that must be overcome when diffusing through the sample.

In this section, variable diffusion time self diffusion experiments are performed on the ^{7}Li cation in each of the polymer-salt samples. ^{7}Li PGSE and PGStE pulse sequences were used over a range of diffusion times (and corresponding diffusion distances) to probe the probe the dependence of the lithium cation self diffusion coefficient upon the relative length scales of the polymer morphology.

B.3.1 SEO6 Sample

The SEO6 sample was studied using a single PGSE experiment with diffusion time of approximately 42 ms and eleven PGStE experiments with diffusion times ranging from 34 to 283 ms. Table B.5 displays the measured self diffusion coefficient from each of these experiments. As the diffusion time in increased and the root mean squared displacement increases from 396 to 856 nm, the self diffusion coefficient decreases, but only modestly. Figure B.3 illustrates this decrease in the self diffusion coefficient as a function of diffusion time and Figure B.4 illustrates this decrease in self diffusion coefficient as a function of the root mean squared displacement (also referred to as the Diffusion Distance).

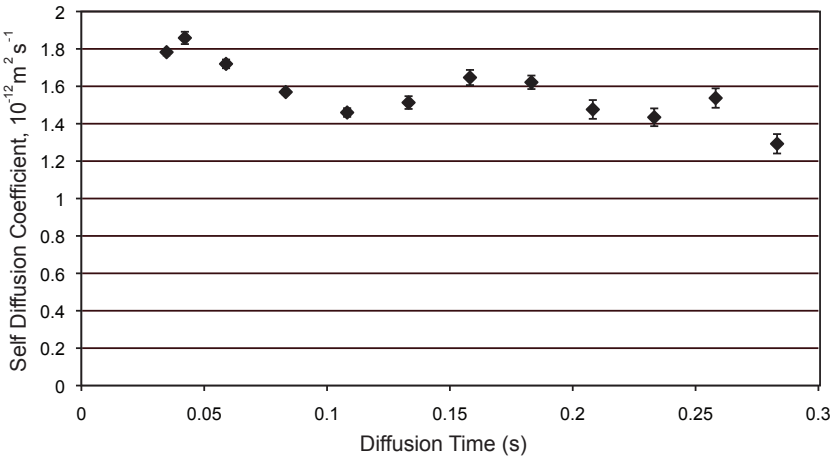


Figure B.3: The self diffusion coefficient of the $^7Li^+$ cation in the SEO6 polymer is displayed as a function of diffusion time, Δ.

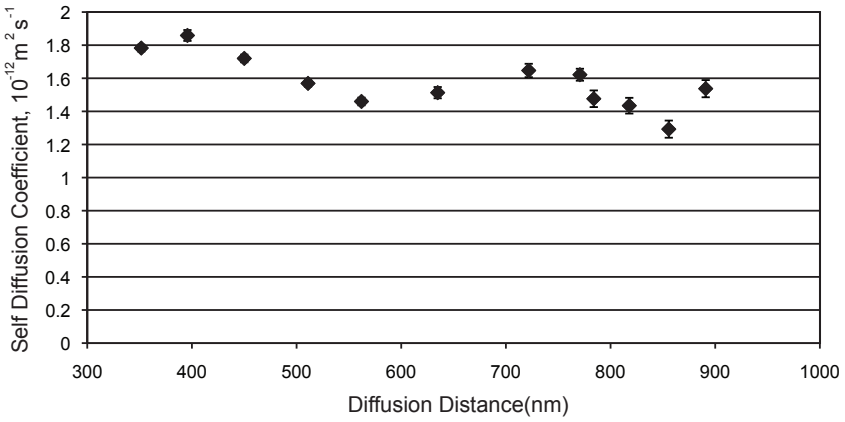


Figure B.4: The self diffusion coefficient of the $^7Li^+$ cation in the SEO6 polymer is displayed as a function of root mean square displacement or diffusion distance, in nanometers.

Table B.5: The self diffusion coefficient of the $^{7}Li^{+}$ cation in the SEO6 polymer is displayed as a function of diffusion time, Δ. The root mean squared displacement, or diffusion distance, is also reported.

Diffusion Time (s)	**^{7}Li Self Diffusion Coefficient,** $10^{-12}m^{2}s^{-1}$	**Diffusion Distance, nm**
0.042126	1.86 +/- 0.03	396.
0.034676	1.78 +/- 0.02	352.
0.058876	1.72 +/- 0.02	450.
0.083176	1.57 +/- 0.02	511.
0.108176	1.46 +/- 0.02	562.
0.133176	1.51 +/- 0.03	635.
0.158176	1.65 +/- 0.04	722.
0.183176	1.62 +/- 0.04	771.
0.208176	1.48 +/- 0.05	784.
0.233176	1.43 +/- 0.05	818.
0.258176	1.54 +/- 0.05	891.
0.283176	1.29 +/- 0.05	856.

B.3.2 PEO Sample

The PEO sample was studied using a single PGSE experiment with sinusoidal gradient pulses with diffusion time of approximately 16 ms, a single PGSE experiment with square gradient pulses with diffusion time of approximately 15 ms and two PGStE experiments with diffusion times of 57 and 205 ms. The T_1 of ^{7}Li in the PEO sample was 0.309 s and the T_2 was 0.084 s. Table B.6 displays the measured self diffusion coefficient from each of these experiments along with the corresponding root mean squared displacement. As the diffusion time is increased and the root mean squared displacement increases from 413 to 1603 nm, the self diffusion coefficient does not display any obvious trend.

Table B.6: The^{7}Li self diffusion coefficient of the lithium ion in the PEO polymer is displayed as a function of diffusion time, Δ. The root mean squared displacement, or diffusion distance, is also reported.

Diffusion Time (s)	**^{19}F Self Diffusion Coefficient, $10^{-12}m^2s^{-1}$**	**Diffusion Distance, nm**
0.016074	5.3 +/- 0.3	413
0.015074	7.0 +/- 0.3	458
0.057174	4.8 +/- 0.5	742
0.205174	6.3 +/- 0.7	1603

B.3.3 SEO5 Sample

The SEO5 sample was studied using a single PGSE experiment with sinusoidal gradient pulses with diffusion time of approximately 16 ms, a single PGSE experiment with square gradient pulses with diffusion time of approximately 15 ms and two PGStE experiments with diffusion times of 57 and 205 ms. The T_1 of ^{7}Li in the SEO5 sample was 0.333 s and the T_2 was 0.084 s. Table B.7 displays the measured self diffusion coefficient from each of these experiments along with the corresponding root mean squared displacement. As the diffusion time is increased and the root mean squared displacement increases from 413 to 1603 nm, the self diffusion coefficient decreases to nearly half its value compared to short diffusion times.

B.3.4 SEO2 Sample

The SEO2 sample was studied using a single PGSE experiment with sinusoidal gradient pulses with diffusion time of approximately 16 ms, a single PGSE experiment with square gradient pulses with diffusion time of approximately 15 ms and two PGStE experiments with diffusion times of 57 and 205 ms. The T_1 of ^{7}Li in the SEO2 sample was 0.311 s and the T_2 was 0.175 s. Table B.8 displays the measured self diffusion coefficient from each of these experiments along with the corresponding root mean squared displacement. As the diffusion time is increased and the root mean squared displacement increases from 413 to 1603 nm, the self diffusion coefficient decreases

Table B.7: The ^{7}Li self diffusion coefficient of the lithium ion in the SEO5 polymer is displayed as a function of diffusion time, Δ. The root mean squared displacement, or diffusion distance, is also reported.

Diffusion Time (s)	**^{19}F Self Diffusion Coefficient,** $10^{-12}m^2s^{-1}$	**Diffusion Distance, nm**
0.016074	5.4 +/- 0.1	415
0.015074	4.9 +/- 0.2	386
0.057174	3.2 +/- 0.2	600
0.205174	2.3 +/- 0.2	967

modestly between approximately 16 ms of diffusion time and 57 ms of diffusion time. No significant change is seen between 57 and 205 ms.

Table B.8: The self diffusion coefficient of the lithium ion in the SEO2 polymer is displayed as a function of diffusion time, Δ. The root mean squared displacement, or diffusion distance, is also reported.

Diffusion Time (s)	**^{19}F Self Diffusion Coefficient,** $10^{-12}m^2s^{-1}$	**Diffusion Distance, nm**
0.016074	2.7 +/- 0.4	297
0.015074	2.7 +/- 0.2	285
0.057174	1.9 +/- 0.4	466
0.205174	2.0 +/- 0.7	899

B.4 Results of Variable Diffusion Time ^{19}F Self Diffusion Experiments

The self diffusion coefficient of the TFSI anion in these polymer-LiTFSI systems can be easily probed using ^{19}F NMR. In this section, variable diffusion time ^{19}F self diffusion experiments are performed on the TFSI anion in each of the polymer-salt samples. ^{19}F PGSE and PGStE pulse sequences were used over a range of diffusion times (and corresponding diffusion distances) to probe the probe the dependence of the TFSI anion self diffusion coefficient upon the relative length scales of the polymer morphology. All experiments were performed at 90°C with diffusion times ranging from 15 to 504 ms.

B.4.1 PEO Sample

The PEO sample was studied using a single PGSE experiment with sinusoidal gradient pulses with diffusion time of approximately 15 ms, a single PGSE experiment with square gradient pulses with diffusion time of approximately 15 ms and two PGStE experiments with diffusion times of 57 and 504 ms. The T_1 of ^{19}F in the PEO sample was 0.853 s and the T_2 was 0.084 s. Table B.9 displays the measured ^{19}F self diffusion coefficient from each of these experiments along with the corresponding root mean squared displacement. As the diffusion time is increased and the root mean squared displacement increases from 997 to 2660 nm, the self diffusion appears to decrease only modestly.

Table B.9: The ^{19}F self diffusion coefficient of TFSI in the PEO polymer is displayed as a function of diffusion time, Δ. The root mean squared displacement, or diffusion distance, is also reported.

Diffusion Time (s)	**^{19}F Self Diffusion Coefficient,** $10^{-11}m^2s^{-1}$	**Diffusion Distance, nm**
0.015075	3.30 +/- 0.05	997
0.015075	3.49 +/- 0.05	1025
0.057175	3.4 +/- 0.1	1986
0.504175	3.0 +/- 0.2	2660

B.4.2 SEO5 Sample

The SEO5 sample was studied using a single PGSE experiment with sinusoidal gradient pulses with diffusion time of approximately 15 ms, a single PGSE experiment with square gradient pulses with diffusion time of approximately 15 ms and two PGStE experiments with diffusion times of 57 and 504 ms. The T_1 of ^{19}F in the SEO5 sample was 0.944 s and the T_2 was 0.731 s. Table B.10 displays the measured ^{19}F self diffusion coefficient from each of these experiments along with the corresponding root mean squared displacement. As the diffusion time is increased and the root mean squared displacement increases from 792 to 2290 nm, the self diffusion does not appear to change.

Table B.10: The ^{19}F self diffusion coefficient of TFSI in the SEO5 polymer is displayed as a function of diffusion time, Δ. The root mean squared displacement, or diffusion distance, is also reported.

Diffusion Time (s)	**^{19}F Self Diffusion Coefficient,** $10^{-11}m^2s^{-1}$	**Diffusion Distance, nm**
0.015075	2.08 +/- 0.03	792
0.015075	1.65 +/- 0.03	705
0.057175	2.00 +/- 0.06	1524
0.504175	2.00 +/- 0.06	2290

B.4.3 SEO6 Sample

The SEO6 sample was studied using a single PGSE experiment with sinusoidal gradient pulses with diffusion time of approximately 15 ms, a single PGSE experiment with square gradient pulses with diffusion time of approximately 15 ms and three PGStE experiments with diffusion times of 32, 57 and 504 ms. The T_1 of ^{19}F in the SEO6 sample was 0.921 s and the T_2 was 0.023 s. Table B.11 displays the measured ^{19}F self diffusion coefficient from each of these experiments along with the corresponding root mean squared displacement. As the diffusion time is increased and the root mean squared displacement increases from 767 to 3889 nm, the self diffusion appears to decrease by approximately 25% (if the square pulsed gradient spin echo experiment is neglected).

Table B.11: The ^{19}F self diffusion coefficient of TFSI in the SEO6 polymer is displayed as a function of diffusion time, Δ. The root mean squared displacement, or diffusion distance, is also reported.

Diffusion Time (s)	**^{19}F Self Diffusion Coefficient,** $10^{-11}m^2s^{-1}$	**Diffusion Distance, nm**
0.015075	1.95 +/- 0.03	767
0.015075	1.5 +/- 0.04	672
0.032175	1.97 +/- 0.05	1126
0.057175	1.83 +/- 0.04	1447
0.504175	1.5 +/- 0.04	3889

B.4.4 SEO2 Sample

The SEO2 sample was studied using a single PGSE experiment with sinusoidal gradient pulses with diffusion time of approximately 15 ms and two PGStE experiments with diffusion times of 57 and 504 ms. The T_1 of ^{19}F in the SEO2 sample was 0.694 s and the T_2 was 0.345 s. Table B.12 displays the measured ^{19}F self diffusion coefficient from each of these experiments along with the corresponding root mean squared displacement. As the diffusion time is increased and the root mean squared displacement increases from 790 to 2840 nm, the self diffusion appears to decrease by approximately 25% (if the square pulsed gradient spin echo experiment is neglected).

Table B.12: The ^{19}F self diffusion coefficient of TFSI in the SEO2 polymer is displayed as a function of diffusion time, Δ. The root mean squared displacement, or diffusion distance, is also reported.

Diffusion Time (s)	**^{19}F Self Diffusion Coefficient,** $10^{-11}m^2s^{-1}$	**Diffusion Distance, nm**
0.015075	2.1 +/- 0.2	790
0.057175	0.605 +/- 0.04	832
0.504175	0.80 +/- 0.05	2840

Appendix C

Single T_1 Inversion Recovery Fit: Example Mathematica Code

This notebook demonstrates how to import and fit T1 data from an Inversion Recovery Experiment. The data in this case comes from a study of the 19F T1 in a PEO and LiTFSI sample that was done on the 65.6 MHz instrument at 61.7015 MHz and 90 C.

T1 PEO Data

The following commands import the data and provide the time delays for the Inversion Recovery experiment. The data was processed (NDFT) in NTNMR on the spectrometer computer and exported as a text file. The text file is being important below, and the Drop[] command removes the column headers so *Mathematica* doesn't get confused.

```
num2D = 11;
numPoints = 2048;
delayList = {10, 20, 50, 100, 200, 500, 1000, 2000, 4000, 5000, 6000} / 1000;
data = Import[
   "/Users/Shared/Data/19F NMR Data/110408 PEO Data/19F InvRec T1 PEO 90 C.txt", "Data"];
data = Drop[data, 4];
```

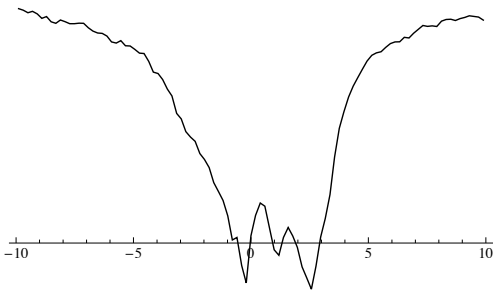
The following command partitions the imported data into a {ppm, real signal} format so the real data from the NMR spectrum can be used.

```
totalData = Table[{}, {i, 1, num2D}];
For[i = 0, i < num2D,
  (
   For[j = 0, j < numPoints,
     (
      totalData[[i]] =
        Append[totalData[[i]], {data[[j + (i - 1) * numPoints, 3]], data[[j + (i - 1) * numPoints, 1]]}];
     ), j++];
  ), i++];
```

The following commands allow one to select the window for display (below) and ultimately for numerican integration (found by just adding up all of the points in the given ppm range). The peak is simply integrated in this case because it is known that there should only be one type of 19F in the system. The broad line shape of the peak is due to magnetic field inhomogeneity. plot1 below shows the first data point in the Inversion Recovery experiment, which is negatively phased, as it should be.

```
startValue = -10;
endValue = 10;
finalData = Table[{}, {i, 1, num2D}];
For[i = 0, i < num2D,
  (
   For[j = 0, j < numPoints, If[totalData[[i, j, 1]] > startValue && totalData[[i, j, 1]] < endValue,
      finalData[[i]] = Append[finalData[[i]], totalData[[i, j]]]], j++];
  ),
  i++];

plot1 = ListPlot[finalData[[1]], Joined → True, PlotRange → All,
  Axes → {True, False}, PlotStyle → {RGBColor[0, 0, 0], Thickness[0.003`]}]
```



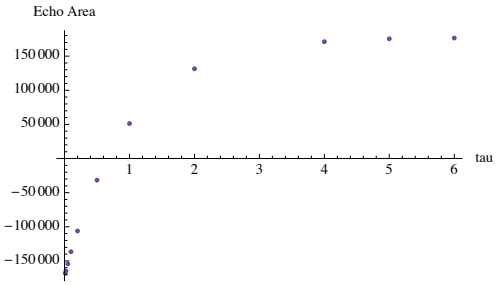
The following command performs the numerical integration from startValue to endValue, provided above.

```
tempSum = 0;
areaList = {};
For[i = 0, i < num2D,
  (
   tempSum = 0;
   For[j = 0, j < Length[finalData[[i]]], tempSum = tempSum + finalData[[i, j, 2]], j++];
   areaList = Append[areaList, tempSum];
  ), i++];
```

The Transpose function is used to merge the list of delays to the areas computed from the numerical integration above.

```
expData = Transpose[{delayList, areaList}];

plot1 = ListPlot[expData, PlotRange → All,
  AxesOrigin → {0, 0}, AxesLabel → {"tau", "Echo Area"}]
```



Single T1 Fit

The NonlinearRegression package is needed if the user would like to generate confidence intervals.

```
Needs["NonlinearRegression`"]
```

The parameters to be fit must be cleared before performing the fit. The model equation for a single T1 Inversion Recovery experiment is provided below.

```
Clear[A, B, T1];
model = A - B * Exp[-t / T1];

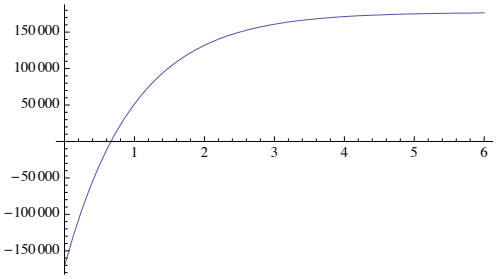
dataFit = NonlinearRegress[expData, model, {{A, 40 000.}, {B, 80 000.}, {T1, 0.5}},
   t, RegressionReport → {BestFitParameters, ParameterCITable}];
fit = BestFitParameters /. dataFit;
CITable = ParameterCITable /. dataFit;
```

Displaying the CI Table provides the nonlinear regression best fit values of A, B, and T1. It also provides the 95 % confidence intervals for each variable. In this case, those of T1 are of interest. Although the fit is quite good, the confidence interval is still quite large (on the order of 10 ms or so). In this case, the T1 was of interest to set the recycle delay, so this level of confidence is sufficient. For a narrower confidence interval, more 2D data points should be used.

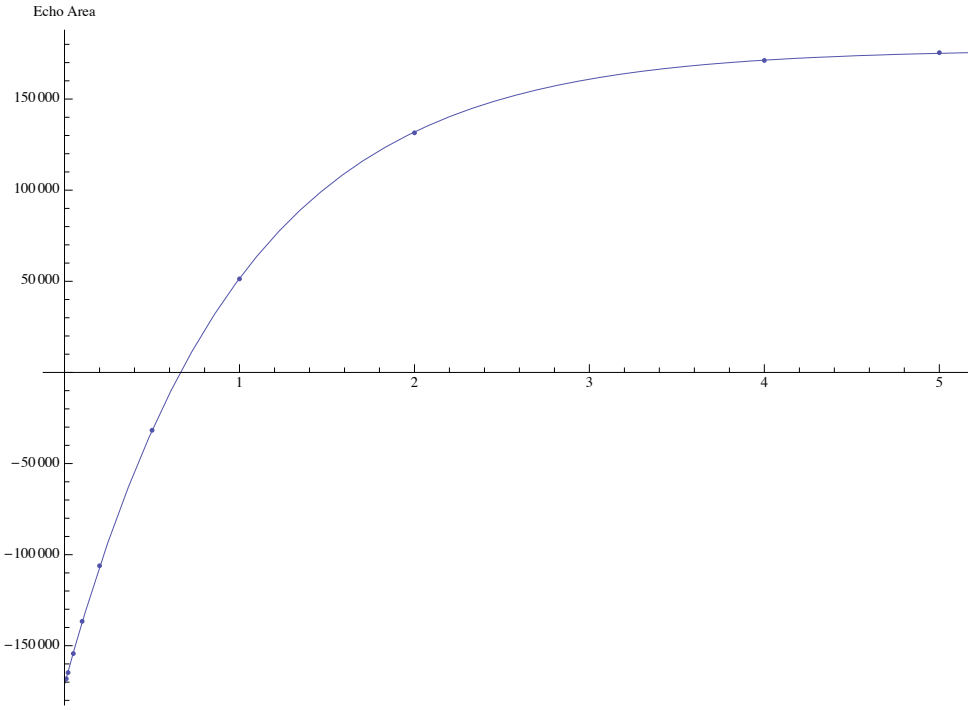
```
CITable
```

	Estimate	Asymptotic SE	CI
A	177 208.	341.825	{176 419., 177 996.}
B	348 442.	417.416	{347 480., 349 405.}
T1	0.979857	0.00385549	{0.970966, 0.988747}

```
A = A /. fit;
B = B /. fit;
T1 = T1 /. fit;
plot2 = Plot[model, {t, 0, 6}, PlotRange → All]
```




```
plot3 = Show[plot1, plot2]
```



Appendix D

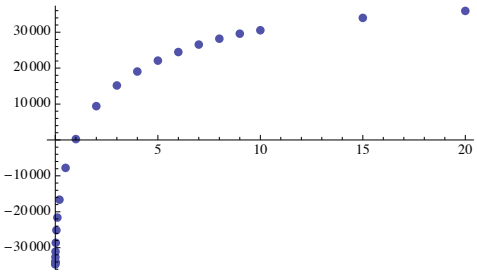
Multiple T_1 Inversion Recovery Fit: Example Mathematica Code

This notebook demonstrates how to fit a two - T1 model to the results of an Inversion Recovery experiment. In this example, a LaPO4 sample is being studied using 31P MAS NMR. The peak heights of the LaPO4 peak are entered directly into the ampList variable, rather than importing the text file directly (which is more common).

Input T1 Data

First, the time delay data (timeList) and peak height data (ampList) are entered into *Mathematica*. The data is plotted, and it shows the typical form of an Inversion Recovery experiment.

```
timeList = {0.0909, 0.1818, 0.4545, 1, 2, 5, 10, 20, 50, 100, 200, 500, 1000,
    2000, 3000, 4000, 5000, 6000, 7000, 8000, 9000, 10 000, 15 000, 20 000} / 1000;
ampList = {-34 640, -34 540, -34 110, -34 100, -33 900, -32 640, -31 100,
   -28 650, -25 130, -21 620, -16 650, -7772, 251.7`, 9413, 15 170,
   19 050, 22 080, 24 490, 26 550, 28 210, 29 580, 30 560, 33 980, 35 920};
data = N[Transpose[{timeList, ampList}]];
ListPlot[data, PlotStyle → {PointSize[0.02]}]
```



Fit T1 Data

■ Fit with a Single T1

First we will try to fit the experimental data with a single T1, as has been demonstrated in another example.

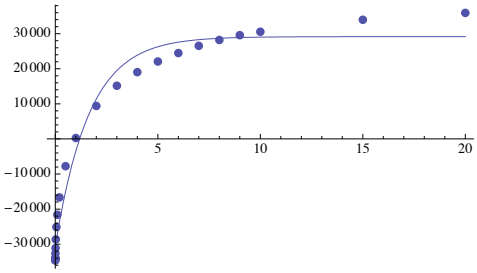
```
Needs["NonlinearRegression`"]

Clear[A, B, τ, model]
model = A * (1 - 2 * Exp[-t / τ]) + B;
temp = NonlinearRegress[data, model, {{A, 3 * 10^4}, {B, 300.}, {τ, 1.}}, t,
   RegressionReport → {BestFitParameters, ParameterCITable}, MaxIterations → 1000];
{fit, CITable} = {BestFitParameters /. temp, ParameterCITable /. temp};
Print[CITable];
```

	Estimate	Asymptotic SE	CI
A	29 876.	1014.95	{27 765.3, 31 986.7}
B	-718.381	1116.74	{-3040.77, 1604.}
τ	1.64915	0.222472	{1.18649, 2.1118}

```
{A, B, τ} = {A /. fit, B /. fit, τ /. fit};
```

```
dataPlot = ListPlot[data, PlotStyle → {PointSize[0.02]}];
dataFit = Plot[model, {t, 0, timeList[[Length[timeList]]]}, PlotRange → All];
Show[dataFit, dataPlot, AxesOrigin → {0, 0}]
```



As can be seen, the fit does not describe the data well - the fit overestimates the T1 at short times and does not come to the same equilibrium value as the data at long times. We will now modify the model equation to perform a two-T1 fit.

■ Fit with Two T1s

The same procedure as for the single T1 fit is performed, but now the model equation has been changed to account for a second T1.

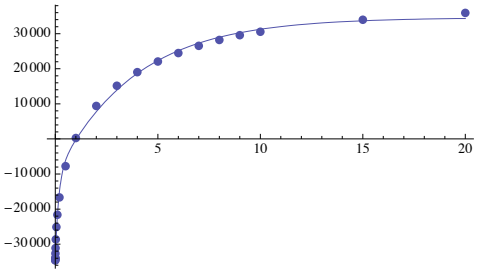
```
Clear[A1, A2, B, τ1, τ2, model]
model = A1 * (1 - 2 * Exp[-t / τ1]) + A2 * (1 - 2 * Exp[-t / τ2]) + B;
temp = NonlinearRegress[data, model,
   {{A1, 15000.}, {A2, 15000.}, {B, -700.}, {τ1, 0.5}, {τ2, 5.}}, t,
   RegressionReport → {BestFitParameters, ParameterCITable}, MaxIterations → 1000];
{fit, CITable} = {BestFitParameters /. temp, ParameterCITable /. temp};
Print[CITable];
```

	Estimate	Asymptotic SE	CI
A1	11519.7	770.284	{9907.5, 13131.9}
A2	22562.4	706.044	{21084.6, 24040.2}
B	506.515	494.803	{-529.119, 1542.15}
τ1	0.165122	0.0242775	{0.114308, 0.215935}
τ2	3.83579	0.285793	{3.23762, 4.43396}

The best fit parameter list and confidence intervals are displayed above. As can be seen, the best fit parameters present one T1 that is shorter and one that is longer than was found above in the single-T1 case. We can now compare the fit to the raw data:

```
{A1, A2, B, τ1, τ2} = {A1 /. fit, A2 /. fit, B /. fit, τ1 /. fit, τ2 /. fit};
```

```
dataPlot = ListPlot[data, PlotStyle → {PointSize[0.02]}];
dataFit = Plot[model, {t, 0, timeList[[Length[timeList]]]}, PlotRange → All];
Show[dataFit, dataPlot, AxesOrigin → {0, 0}]
```



The fit describes the data much better than the single - T1 model case. If narrower confidence intervals are required for the two T1s found here, an additional experiment with more delays - especially ones at longer delay times - will improve the uncertainty of the fits displayed above.

Appendix E

Single and Multiple T_1 Saturation Recovery Fit: Example Mathematica Code

This notebook illustrates how to fit MAS NMR Saturation Recovery experiment data and then how to extract the T1 of each peak using a nonlinear regression package in *Mathematica*. In this example, a 32% SrCeP3O9 sample is being studied using 31P MAS NMR. (In this case, a different synthetic route was taken than that discussed in the study of (Ce,Sr) metaphosphate glass-ceramic materials discussed previously.) 6.593 pppm is added to all chemical shifts when the data is imported in order to correctly reference the peaks to H3PO4.

```
Needs["NonlinearRegression`"]
```

Import T1 Data

First, the data is imported from a NTNMR data file. The data has been previously processed using the NDFT command in NTNMR.

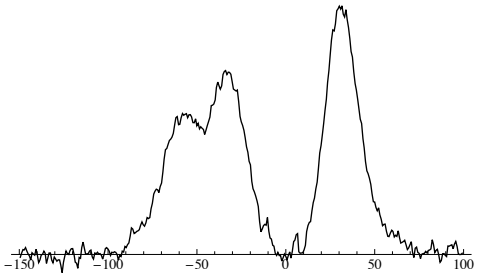
```
num2D = 16;
numPoints = 2048;
timeList =
  15 * {0.0002, 0.0005, 0.001, 0.002, 0.005, 0.01, 0.02, 0.05, 0.5, 1, 2, 5, 10, 20, 50, 60};
data = Import["/Users/Shared/Data/31P 1D NMR/65 MHz
     Data/100726 31P SrCeP3O9/31P SatRecT1 SrCeP3O9.txt", "Data"];
data =
  Drop[
   data,
   4];

totalData = Table[{}, {i, 1, num2D}];
For[i = 0, i < num2D,
  (
   For[j = 0, j < numPoints,
     (
      totalData[[i]] = Append[totalData[[i]],
         {data[[j + (i - 1) * numPoints, 3]] + 6.593, data[[j + (i - 1) * numPoints, 1]]}];
     ), j++];
  ), i++];

startValue = -150;
endValue = 100;
finalData = Table[{}, {i, 1, num2D}];
For[i = 0, i < num2D,
  (
   For[j = 0, j < numPoints, If[totalData[[i, j, 1]] > startValue && totalData[[i, j, 1]] < endValue,
      finalData[[i]] = Append[finalData[[i]], totalData[[i, j]]]], j++];
  ),
  i++];
```

To ensure that the data looks correct, we check the last 2D point in the experiment, because this spectrum is should be identical to a 90-acquire experiment.

```
plotT1 = ListPlot[finalData[[16]], Joined → True, PlotRange → All,
  Axes → {True, False}, PlotStyle → {RGBColor[0, 0, 0], Thickness[0.003`]}]
```

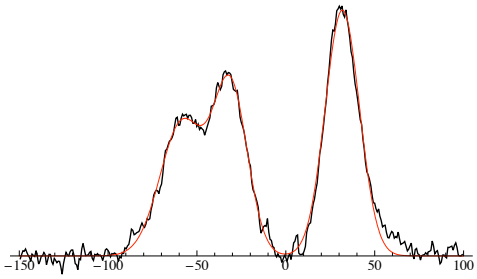


■ Fit Final Data Set

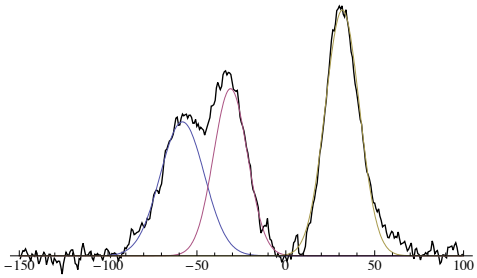
We now fit the final spectrum of the experiment to find the peak centers and widths. Once the centers and widths are known, all data from the entire 2D experiment can be fit with fixed centers and widths, allowing only the peak amplitude to change. It is the amplitude data that will be fit to find the T1 of each peak.

```
Clear[A1, A2, A3, C1, C2, C3, W1, W2, W3, model,
  test1, peakOne, peakTwo, peakThree, function, modelPlot];
A1guess = 40000.;
A2guess = 195000.;
A3guess = 180000.;
C1guess = -72.;
C2guess = -35.;
C3guess = 30.;
W1guess = 25.;
W2guess = 9.;
W3guess = 18.;
model = A1 * Exp[-(x - C1)^2 / (2 * W1^2)] + A2 * Exp[-(x - C2)^2 / (2 * W2^2)] +
   A3 * Exp[-(x - C3)^2 / (2 * W3^2)];
temp = NonlinearRegress[finalData[[16]],
   model, {{A1, A1guess}, {A2, A2guess}, {A3, A3guess}, {C1, C1guess},
    {C2, C2guess}, {C3, C3guess}, {W1, W1guess}, {W2, W2guess}, {W3, W3guess}}, x,
   RegressionReport → {BestFitParameters, ParameterCITable}, MaxIterations → 500];
test1 = BestFitParameters /. temp;
CITable = ParameterCITable /. temp;
Print[CITable];
{A1, A2, A3, C1, C2, C3, W1, W2, W3} = {Abs[A1] /. test1, Abs[A2] /. test1, Abs[A3] /. test1,
   C1 /. test1, C2 /. test1, C3 /. test1, W1 /. test1, W2 /. test1, W3 /. test1};
peakOne = A1 * Exp[-(x - C1)^2 / (2 * W1^2)];
peakTwo = A2 * Exp[-(x - C2)^2 / (2 * W2^2)];
peakThree = A3 * Exp[-(x - C3)^2 / (2 * W3^2)];
function = peakOne + peakTwo + peakThree;
modelPlot = Plot[function, {x, startValue, endValue}, PlotRange → All,
   PlotStyle → {RGBColor[1, 0, 0]}];
Show[plotT1, modelPlot]
```

	Estimate	Asymptotic SE	CI
A1	10 210.	154.924	{9905.21, 10 514.7}
A2	12 738.5	266.401	{12 214.4, 13 262.5}
A3	18 738.2	146.854	{18 449.4, 19 027.1}
C1	-58.1967	0.539073	{-59.2572, -57.1363}
C2	-31.1048	0.334548	{-31.7629, -30.4467}
C3	31.8325	0.0871767	{31.661, 32.004}
W1	12.402	0.423156	{11.5696, 13.2345}
W2	-9.55357	0.239915	{-10.0255, -9.08161}
W3	9.63329	0.0871776	{9.4618, 9.80478}




```
plotT1fits =
  Plot[{peakOne, peakTwo, peakThree}, {x, startValue, endValue}, PlotRange → All];
Show[plotT1, plotT1fits]
```



■ Fit all Data, Keeping Centers Fixed (clear only A1, A2, A3)

Now, only A1, A2, and A3 will be fit for each 2D spectrum. This is performed using a For loop. The result of the fit is placed in the matrix "ampData." The data to fit each peak can then be extracted to perform the fit of the saturation recovery data.

```
A1guess = A1;
A2guess = A2;
A3guess = A3;

ampData = {};
```

```
For[i = 0, i < num2D,
  (
   Clear[A1, A2, A3, A4, A5, A6, model, test1, peakOne,
    peakTwo, peakThree, peakFour, peakFive, peakSix, function, modelPlot];

   model = Abs[A1] * Exp[-(x - C1)^2 / (2 * W1^2)] + Abs[A2] * Exp[-(x - C2)^2 / (2 * W2^2)] +
     Abs[A3] * Exp[-(x - C3)^2 / (2 * W3^2)];
   test1 = FindFit[finalData[[i]], model,
     {{A1, A1guess}, {A2, A2guess}, {A3, A3guess}}, {x}, MaxIterations → 500];
   {A1, A2, A3} = {Abs[A1] /. test1, Abs[A2] /. test1, Abs[A3] /. test1};

   ampData = Append[ampData, {timeList[[i]], A1, A2, A3}];

  ), i++];
```

```
ampData
```

```
{{0.003, 2648.1, 582.423, 2297.74}, {0.0075, 4587.62, 1098.62, 4611.99},
 {0.015, 6756.43, 1546.51, 8179.34}, {0.03, 8390.75, 2185.79, 12473.5},
 {0.075, 9275.58, 3703.65, 17836.2}, {0.15, 9479.84, 5838.96, 19298.5},
 {0.3, 9833.87, 7500.18, 19184.7}, {0.75, 9658., 10288.7, 18722.},
 {7.5, 9981.32, 11021.8, 18554.9}, {15, 10371.8, 11230.3, 18543.6},
 {30, 10186.3, 11440.4, 18152.4}, {75, 10088.7, 12092.4, 18509.3},
 {150, 9974.46, 12231.3, 17616.7}, {300, 10018.8, 11870.2, 18015.4},
 {750, 9769.24, 11880.6, 17579.4}, {900, 10210., 12738.5, 18738.2}}
```

```
MatrixForm[ampData]
```

0.003	2648.1	582.423	2297.74
0.0075	4587.62	1098.62	4611.99
0.015	6756.43	1546.51	8179.34
0.03	8390.75	2185.79	12473.5
0.075	9275.58	3703.65	17836.2
0.15	9479.84	5838.96	19298.5
0.3	9833.87	7500.18	19184.7
0.75	9658.	10288.7	18722.
7.5	9981.32	11021.8	18554.9
15	10371.8	11230.3	18543.6
30	10186.3	11440.4	18152.4
75	10088.7	12092.4	18509.3
150	9974.46	12231.3	17616.7
300	10018.8	11870.2	18015.4
750	9769.24	11880.6	17579.4
900	10210.	12738.5	18738.2

Analyze Data

We now extract the relevant data for the first peak at - 64 ppm to find the T1.

■ One T1 Fit (-58ppm)

This puts the data from column 1 of "ampData" into the variable "peakOneData" in the form {time delay, amplitude}, which is needed for the NonlinearRegress function below.

```
peakOneData = {};
For[i = 0, i < 10, peakOneData = Append[peakOneData, {ampData[[i, 1]], ampData[[i, 2]]}];, i++];
```

The variables to be fit - A, B, and τ - are then cleared. The model equation is defined, and the NonlinearRegress function is called using peakOneData and the model. Initial guesses are provided for A, B, and τ.

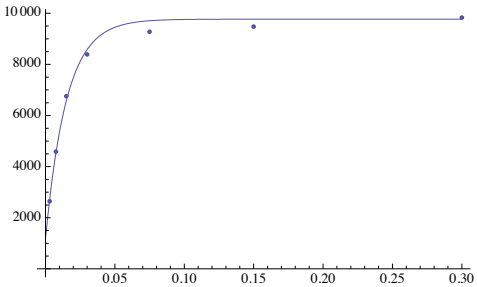
```
Clear[A, B, τ, model]
model = A * (1 - Exp[-t / τ]) + B;
temp = NonlinearRegress[peakOneData, model, {{A, 10^9}, {B, 300.}, {τ, 0.05}}, t,
   RegressionReport → {BestFitParameters, ParameterCITable}, MaxIterations → 1000];
{fit, CITable} = {BestFitParameters /. temp, ParameterCITable /. temp};
Print[CITable];
```

	Estimate	Asymptotic SE	CI
A	8577.22	491.516	{7414.97, 9739.47}
B	1192.47	490.952	{31.5542, 2353.39}
τ	0.0151764	0.00177148	{0.0109875, 0.0193653}

The Best Fit Paramters and corresponding confidence intervals are displayed above. The model equation with the best fit parameters can then be plotted against the data used in the fit to confirm that the fit matches the data:

```
{A, B, τ} = {A /. fit, B /. fit, τ /. fit};

peakOnePlot = ListPlot[Drop[peakOneData, -3]];
peakOnefit = Plot[model, {t, 0, timeList[[7]]}, PlotRange → All];
Show[peakOnefit, peakOnePlot, AxesOrigin → {0, 0}]
```



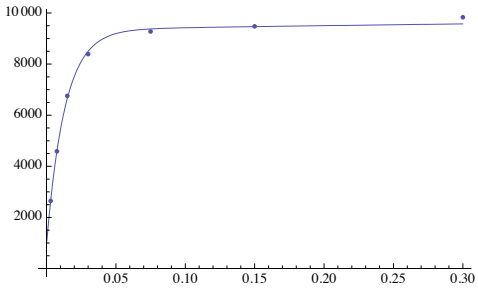
The fit looks pretty good, although it is possible that there is a second slower T1. An additional experiment with many more 2D points would be needed to measure this T1 with great confidence. We can try a fit with this current data, though.

```
Clear[A1, A2, B, τ1, τ2, model]
model = A1 * (1 - Exp[-t / τ1]) + A2 * (1 - Exp[-t / τ2]) + B;
temp = NonlinearRegress[peakOneData, model,
   {{A1, 9. * 10^3}, {A2, 8. * 10^2}, {B, 900.}, {τ1, 0.05}, {τ2, 0.08}}, t,
   RegressionReport → {BestFitParameters, ParameterCITable}, MaxIterations → 1000];
{fit, CITable} = {BestFitParameters /. temp, ParameterCITable /. temp};
Print[CITable];
```

	Estimate	Asymptotic SE	CI
A1	829.205	233.999	{227.69, 1430.72}
A2	8381.63	333.649	{7523.96, 9239.3}
B	956.625	330.102	{108.07, 1805.18}
τ1	0.900073	0.735513	{-0.990623, 2.79077}
τ2	0.013195	0.00118693	{0.0101439, 0.0162461}

```
{A1, A2, B, τ1, τ2} = {A1 /. fit, A2 /. fit, B /. fit, τ1 /. fit, τ2 /. fit};

peakOnePlot = ListPlot[Drop[peakOneData, -3]];
peakOnefit = Plot[model, {t, 0, timeList[[7]]}, PlotRange → All];
Show[peakOnefit, peakOnePlot, AxesOrigin → {0, 0}]
```



As can be seen, the data fit is much improved, but the uncertainty of the longer T1 is very high. As mentioned above, more data is needed for a more reliable fit.

This same process is repeated for the other two peaks below, both of which require only a single T1 to complete a good fit:

■ One T1 Fit (-31ppm)

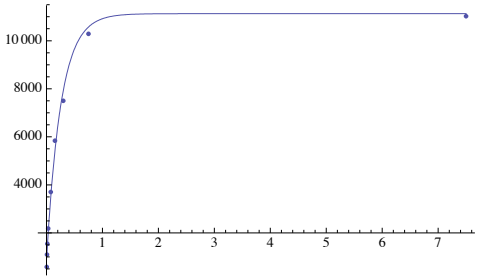
```
peakTwoData = {};
For[i = 0, i < 11, peakTwoData = Append[peakTwoData, {ampData[[i, 1]], ampData[[i, 3]]}];, i++];

Clear[A, B, τ, model]
model = A * (1 - Exp[-t / τ]) + B;
temp = NonlinearRegress[peakTwoData, model, {{A, 30000.}, {B, 3000.}, {τ, 0.011}}, t,
   RegressionReport → {BestFitParameters, ParameterCITable}, MaxIterations → 1000];
{fit, CITable} = {BestFitParameters /. temp, ParameterCITable /. temp};
Print[CITable];
```

	Estimate	Asymptotic SE	CI
A	10245.3	238.894	{9694.42, 10796.2}
B	882.589	180.712	{465.867, 1299.31}
τ	0.25704	0.0192543	{0.21264, 0.301441}

```
{A, B, τ} = {A /. fit, B /. fit, τ /. fit};
```

```
peakTwoPlot = ListPlot[Drop[peakTwoData, -2]];
peakTwofit = Plot[model, {t, 0, timeList[[9]]}, PlotRange → All];
Show[peakTwofit, peakTwoPlot, PlotRange → All]
```



■ One T1 Fit (31ppm)

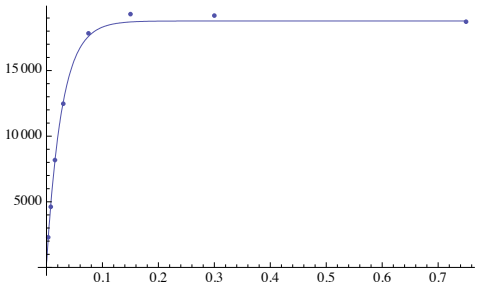
```
peakThreeData = {};
For[i = 0, i < 11,
  peakThreeData = Append[peakThreeData, {ampData[[i, 1]], ampData[[i, 4]]}];, i++];
```

```
Clear[A, B, τ, model]
model = A * (1 - Exp[-t / τ]) + B;
temp = NonlinearRegress[peakThreeData, model, {{A, 1000.}, {B, 600.}, {τ, 0.03}}, t,
   RegressionReport → {BestFitParameters, ParameterCITable}, MaxIterations → 1000];
{fit, CITable} = {BestFitParameters /. temp, ParameterCITable /. temp};
Print[CITable];
```

	Estimate	Asymptotic SE	CI
A	18 510.2	422.608	{17 535.7, 19 484.7}
B	264.325	414.904	{-692.446, 1221.1}
τ	0.0271772	0.00155165	{0.0235991, 0.0307553}

```
{A, B, τ} = {A /. fit, B /. fit, τ /. fit};
```

```
peakThreePlot = ListPlot[Drop[peakThreeData, -3]];
peakThreefit = Plot[model, {t, 0, timeList[[8]]}, PlotRange → All];
Show[peakThreefit, peakThreePlot]
```



Appendix F

Single T_2 Spin Echo Fit: Example Mathematica Code

This notebook demonstrates how to import and fit T2 data from a Spin Echo Experiment. The data in this case comes from a study of the 19F T2 in a PEO and LiTFSI sample that was done on the 65.6 MHz instrument at 61.7015 MHz and 90 C.

T2 PEO Data

The following commands import the data and provide the time delays for the Spin Echo experiment. The data was processed (NDFT) in NTNMR on the spectrometer computer and exported as a text file. The text file is being imported below, and the Drop[] command removes the column headers so *Mathematica* doesn't get confused.

```
num2D = 11;
numPoints = 2048;
delayList = {1, 2, 5, 10, 15, 20, 30, 50, 100, 500, 1000} / 1000;
data =
  Import["/Users/Shared/Data/19F NMR Data/110408 PEO Data/19F SE T2 PEO 90 C.txt", "Data"];
data = Drop[data, 4];
```

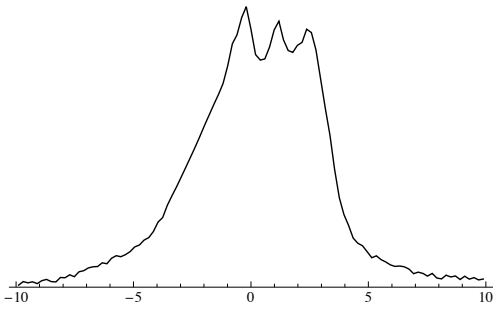
The following command partitions the imported data into a {ppm, real signal} format so the real data from the NMR spectrum can be used.

```
totalData = Table[{}, {i, 1, num2D}];
For[i = 0, i < num2D,
  (
   For[j = 0, j < numPoints,
     (
      totalData[[i]] =
        Append[totalData[[i]], {data[[j + (i - 1) * numPoints, 3]], data[[j + (i - 1) * numPoints, 1]]}];
     ), j++];
  ), i++];
```

The following commands allow one to select the window for display (below) and ultimately for numerican integration (found by just adding up all of the points in the given ppm range). The peak is simply integrated in this case because it is known that there should only be one type of 19F in the system. The broad line shape of the peak is due to magnetic field inhomogeneity. plot1 below shows the first data point in the Spin Echo experiment, which is positively phased, as it should be.

```
startValue = -10;
endValue = 10;
finalData = Table[{}, {i, 1, num2D}];
For[i = 0, i < num2D,
  (
   For[j = 0, j < numPoints, If[totalData[[i, j, 1]] > startValue && totalData[[i, j, 1]] < endValue,
      finalData[[i]] = Append[finalData[[i]], totalData[[i, j]]]], j++];
  ),
  i++];

plot1 = ListPlot[finalData[[1]], Joined → True, PlotRange → All,
  Axes → {True, False}, PlotStyle → {RGBColor[0, 0, 0], Thickness[0.003`]}]
```



Printed by Mathematica for Students

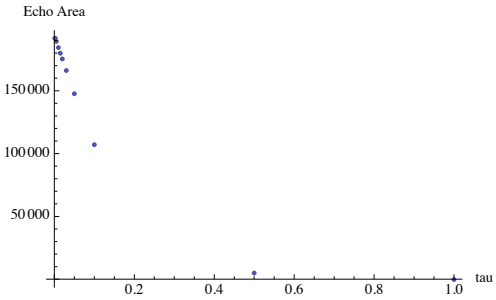
The following command performs the numerical integration from startValue to endValue, provided above.

```
tempSum = 0;
areaList = {};
For[i = 0, i < num2D,
  (
   tempSum = 0;
   For[j = 0, j < Length[finalData[[i]]], tempSum = tempSum + finalData[[i, j, 2]], j++];
   areaList = Append[areaList, tempSum];
  ), i++];
```

The Transpose function is used to merge the list of delays to the areas computed from the numerical integration above.

```
expData = Transpose[{delayList, areaList}];

plot1 = ListPlot[expData, PlotRange → All,
  AxesOrigin → {0, 0}, AxesLabel → {"tau", "Echo Area"}]
```



Single T2 Fit

The NonlinearRegression package is needed if the user would like to generate confidence intervals.

```
Needs["NonlinearRegression`"]
```

The parameters to be fit must be cleared before performing the fit. The model equation for a single T2 Spin Echo experiment is provided below. Note that in this case, the delays provided above are the delays between the 90 and 180 pulses, which is why the time variable (t) is multiplied by 2 in the model equation below. If the total delay is being used rather than the delay between pulses, the 2 would not be necessary.

```
Clear[A, B, T2];
model = A + B * Exp[-2 * t / T2];

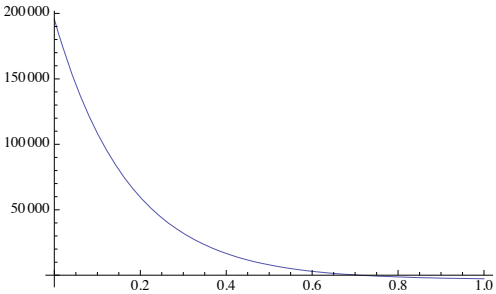
dataFit = NonlinearRegress[expData, model, {{A, 5000.}, {B, 60 000.}, {T2, 0.1}},
   t, RegressionReport → {BestFitParameters, ParameterCITable}];
fit = BestFitParameters /. dataFit;
CITable = ParameterCITable /. dataFit;
```

Displaying the CI Table provides the nonlinear regression best fit values of A, B, and T2. It also provides the 95 % confidence intervals for each variable. In this case, those of T2 are of interest. Although the fit is quite good, the confidence interval is still quite large (on the order of 25 ms or so). In this case, the T2 was of interest to ensure that a PFG experiment, which requires a T2 of greater than 20ms, could be performed, so this level of confidence is sufficient. For a narrower confidence interval, more 2D data points should be used.

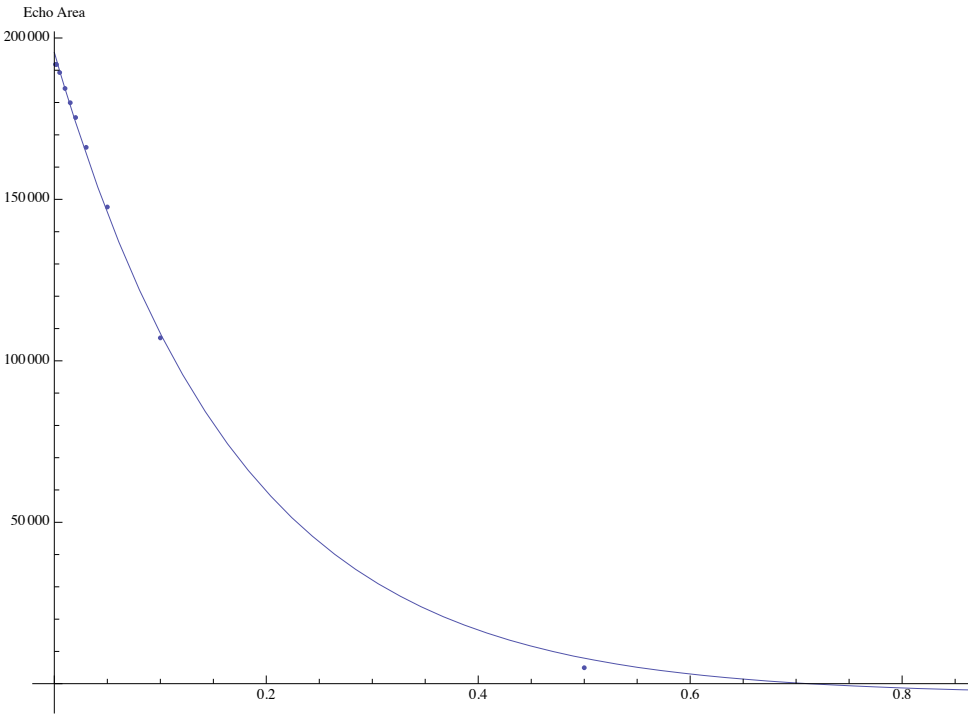
CITable

	Estimate	Asymptotic SE	CI
A	-3294.96	1829.53	{-7513.87, 923.949}
B	198763.	1917.7	{194341., 203185.}
T2	0.347603	0.012187	{0.3195, 0.375707}

```
A = A /. fit;
B = B /. fit;
T2 = T2 /. fit;
plot2 = Plot[model, {t, 0, 1}, PlotRange → All]
```




```
plot3 = Show[plot1, plot2]
```



Appendix G

Multiple T_2 Spin Echo Fit: Example Mathematica Code

This notebook demonstrates how to import and fit T2 data from a Spin Echo Experiment. The data in this case comes from a study of the 1H T2 in a polymer sample that was done on the 65.6 MHz instrument.

Import Polymer Data

The following commands import the data and provide the time delays for the Spin Echo experiment. The data was processed (NDFT) in NTNMR on the spectrometer computer and exported as a text file. The text file is being imported below, and the Drop[] command was not used in this case because the column headers were removed manually in the text file.

```
num2D = 12;
numPoints = 4096;
timeList = {0.00001, 0.00002, 0.00005,
   0.0001, 0.0002, 0.0005, 0.001, 0.002, 0.005, 0.010, 0.020, 0.050};
data = Import["/Users/Shared/Data/1H NMR Data/65 MHz Data/Justin
     Samples/1H SpinEcho T2 polymer 105C.txt", "Data"];
```

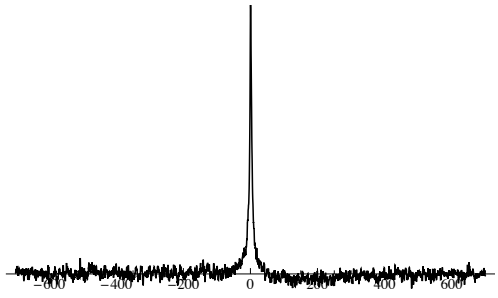
The following command partitions the imported data into a {ppm, real signal} format so the real data from the NMR spectrum can be used.

```
totalData = Table[{}, {i, 1, num2D}];
For[i = 0, i < num2D,
  (
   For[j = 0, j < numPoints,
     (
      totalData[[i]] =
        Append[totalData[[i]], {data[[j + (i - 1) * numPoints, 3]], data[[j + (i - 1) * numPoints, 1]]}];
     ), j++];
  ), i++];
```

The following commands allow one to select the window for display (below) and ultimately for peak fitting. plot1 below shows the first data point in the Spin Echo experiment, which is positively phased, as it should be.

```
startValue = -700;
endValue = 700;
finalData = Table[{}, {i, 1, num2D}];
For[i = 0, i < num2D,
  (
   For[j = 0, j < numPoints, If[totalData[[i, j, 1]] > startValue && totalData[[i, j, 1]] < endValue,
      finalData[[i]] = Append[finalData[[i]], totalData[[i, j]]]], j++];
  ),
  i++];

plot1 = ListPlot[finalData[[1]], Joined → True, PlotRange → All,
  Axes → {True, False}, PlotStyle → {RGBColor[0, 0, 0], Thickness[0.003`]}]
```



Rather than numerically integrate the peak, this first peak is fit to a Lorentzian in order to find the peak center of mass (chemical

shift) and the weak width.

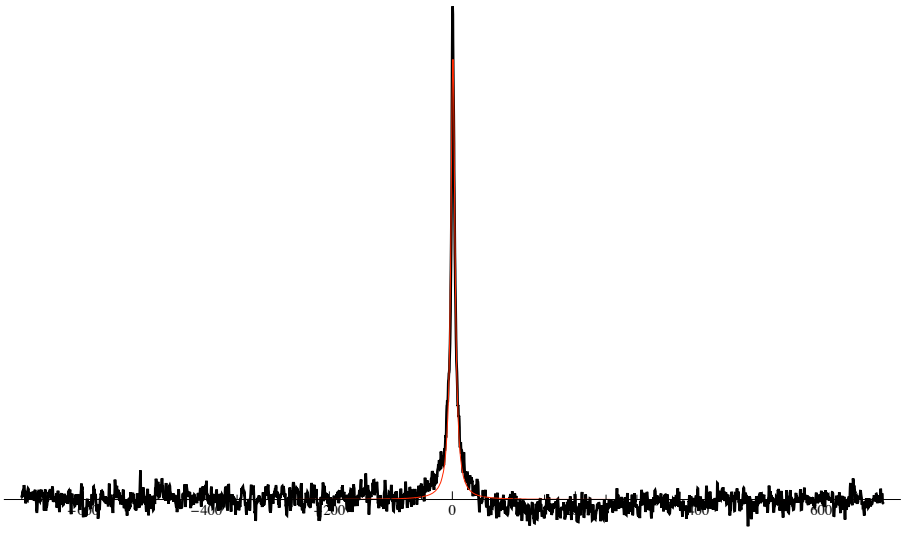
■ Fit Final Data Set One Peak

In order to fit the peak, the parameters are first cleared and then the mathematical model for the Lorentzian line shape is defined. FindFit is used to fit the data. (If confidence intervals for the Lorentzian line shape parameters are needed, the Nonlinear Regression package should be used.) The results of the fit are then plotted with the original data, and the fit looks pretty good.

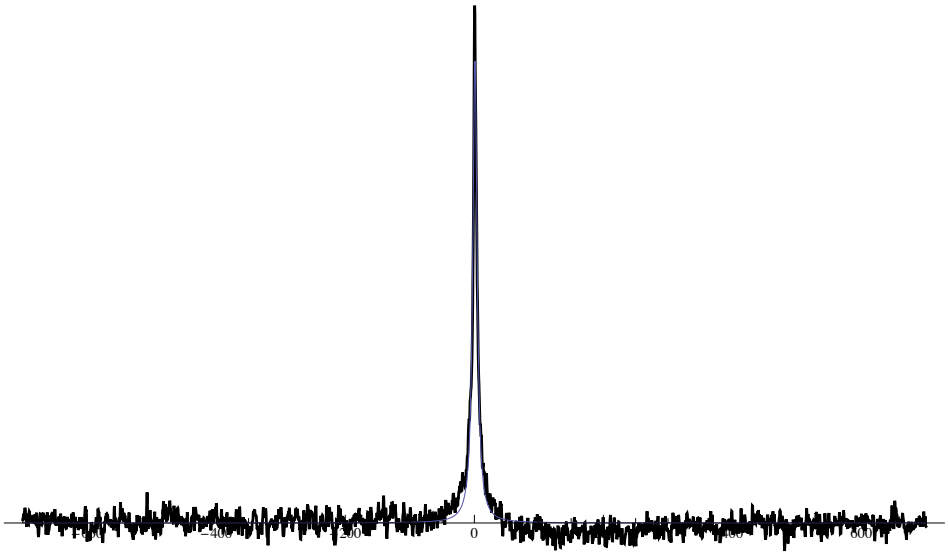
```
Clear[A1, A2, A3, C1, C2, C3, W1, W2, W3, model,
  test1, peakOne, peakTwo, peakThree, function, modelPlot];
A1guess = 10.^9;
C1guess = 7.;
W1guess = 18.;
model = Abs[A1] * 1/(W1^2 + (x - C1)^2);
test1 = FindFit[finalData[[1]], model,
   {{A1, A1guess}, {C1, C1guess},
    {W1, W1guess}}, {x}, MaxIterations → 500];
{A1, C1, W1} = {Abs[A1] /. test1, C1 /. test1, W1 /. test1};
Print[MatrixForm[{{"A", "C", "W"}, {A1, C1, W1}, {A2, C2, W2}}]];
peakOne = A1 * 1/(W1^2 + (x - C1)^2);

function = peakOne;
modelPlot = Plot[function, {x, startValue, endValue}, PlotRange → All,
   PlotStyle → {RGBColor[1, 0, 0]}];
Show[plot1, modelPlot]
```

```
A        C         W
24189.4  0.926564  4.02685
A2       C2        W2
```



```
plot1fits = Plot[{peakOne}, {x, startValue, endValue}, PlotRange → All];
Show[plot1, plot1fits]
```



The two dimensional data set is then fit with the peak center and peak width fixed (from the above fit), and only the amplitude term of the Lorentzian peak is allowed to change. This is accomplished by using a For loop to go through the data and fit each of the spectra.

■ Fit all Data, Keeping Centers Fixed (clear only A1, A2, A3)

```
A1guess = A1;

ampData = {};

For[i = 0, i < num2D,
  (
  Clear[A1, A2, model, test1, peakOne, function, modelPlot];

  model = Abs[A1] * 1/(W1^2 + (x - C1)^2);
  test1 = FindFit[finalData[[i]], model,
    {{A1, A1guess}, {A2, A2guess}}, {x}, MaxIterations → 500];
  {A1, A2} = {Abs[A1] /. test1, Abs[A2] /. test1};

  ampData = Append[ampData, {timeList[[i]], A1}];

  ), i++];
```

```
ampData
```

```
{{0.00001, 24189.4}, {0.00002, 23389.}, {0.00005, 21932.7}, {0.0001, 20285.7},
 {0.0002, 18422.7}, {0.0005, 15646.}, {0.001, 13196.2}, {0.002, 9589.65},
 {0.005, 5260.64}, {0.01, 2375.05}, {0.02, 331.123}, {0.05, 65.7111}}
```

```
MatrixForm[ampData]
```

0.00001	24189.4
0.00002	23389.
0.00005	21932.7
0.0001	20285.7
0.0002	18422.7
0.0005	15646.
0.001	13196.2
0.002	9589.65
0.005	5260.64
0.01	2375.05
0.02	331.123
0.05	65.7111

Analyze Data - One Peak

A fit is first attempted with a single exponential, using the FindFit function. This function, while very simple to use, does not generate a confidence interval. If a confidence interval is needed, the Nonlinear Regression package should be used.

■ Single Exponential Fit

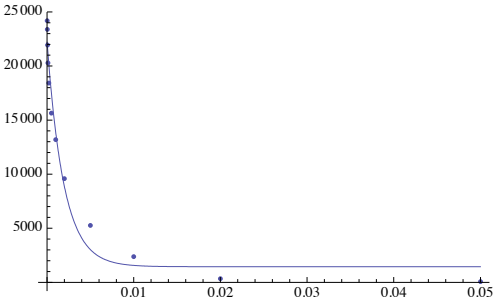
```
peakOneData = ampData;

Clear[A, B, τ]
model = A * (1 - Exp[-t / τ]) + B;
fit = FindFit[peakOneData, model, {{A, 10^4}, B, {τ, 0.05}}, t, MaxIterations → 1000]
```

```
{A → -20747.2, B → 22191.8, τ → 0.001941}
```

```
{A, B, τ} = {A /. fit, B /. fit, τ /. fit};

peakOnePlot = ListPlot[peakOneData, PlotRange → All];
peakOnefit = Plot[model, {t, 0, timeList[[12]]}, PlotRange → All];
Show[peakOnePlot, peakOnefit]
```



As can be seen, the single exponential is close, but appears to overestimate the T2 of some of the spins in the system while

underestimating others. A double exponential fit is now attempted.

■ Double Exponential Fit

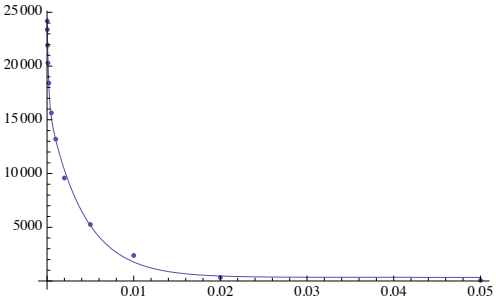
```
peakOneData = ampData;

Clear[ A1, A2, B, τ1, τ2]
model = A1 * (1 - Exp[-t / τ1]) + A2 * (1 - Exp[-t / τ2]) + B;
fit = FindFit[peakOneData, model,
  {{A1, 10^4}, {A2, 10^4}, {B, 0}, {τ1, 0.001}, {τ2, 0.1}}, t, MaxIterations → 1000]
```

```
{A1 → -7720.01, A2 → -16 280.3, B → 24 341.1, τ1 → 0.000172623, τ2 → 0.00410415}
```

```
{A1, A2, B, τ1, τ2} = {A1 /. fit, A2 /. fit, B /. fit, τ1 /. fit, τ2 /. fit};

peakOnePlot = ListPlot[peakOneData, PlotRange → All];
peakOnefit = Plot[model, {t, 0, timeList[[12]]}, PlotRange → All];
Show[peakOnePlot, peakOnefit]
```



As can be seen, the double exponential provides a second T2 to describe the spin echo experimental data. This experiment was performed to provide a preliminary estimate of relevant relaxation parameters for a more compliated system, and so confidence intervals were not measured. Had they been generated, theycertainly would have indicated that the uncertainty of the calculated T2 values is high. This could be improved by increasing the number of two-dimensional delay points in the experiment.

Appendix H

Line Shape Fitting: Example Mathematica Code

This notebook defines and illustrates the use of a Mathematic function that generates a regression fit function that can be used to fit NMR data. Noncrystalline solids, especially the calcium lanthanum phosphate glass ceramic compound studied in this example, often have a distribution of bond lengths, the line shape of an NMR spectrum of nuclei in the compound being studied will be Gaussian in nature. The function defined below to simplify data analysis could easily be adapted for Lorentzian line shapes as well - the function of the For loop following "model = 0" simply needs to be rearranged.

Because several of the variables used in this notebook have similar spelling (which elicits a warning from Mathematica), the spelling error alerts have been turned off:

In[115]:=
```
<< "NonlinearRegression`"
Off[General::"spell"];
Off[General::"spell1"];
```

First the n Gaussian fit function is defined. A brief description on how to input the data is included, although the examples below may be more helpful.

n Gaussian Fit Function Definition

Note:
nGaussianFit[fD, mI, gM, cM] will fit n Gaussians of form A*Exp[-(x-C)^2/(2*W^2)] to a data set (fD) of the form fD = {{x1, y1}, {x2, y2}, ...,{xn, yn}}.
mI is the maximum number of iterations to be used by the function in fitting the data - it must be an integer.
gM (guess matrix) provides the initial guesses for the best fit routine and should be of the form gm = {{A1, A2, A3, ..., An}, {C1, C2, C3,..., C2}, {W1, W2, W3, ..., Wn}}.
cM (constant matrix) provides binary instructions for any guesses that should be held as constant throughout the evaluation, and is of the form cM = {{0,0,0,...}, {0,0,0,...}, {0,0,0,...}}. Replacing any of the zeros with a one will cause that particular guess to be held constant.
n is the number of Gaussians to be used to fit the data - it must be an integer.

In[118]:=
```
nGaussianFit[fD_, mI_, gM_, cM_, n_, compPlot_] :=
 Module[{finalData, maxIt, guessMatrix, constantMatrix, nG, Area, Cent, Width,
   mArea, mCent, mWidth, guessList, variableList, model, myFit, numList,
   areaList, centerList, widthList, outValues, finalModel, finalPlot},
  (
   finalData = fD;
   maxIt = mI;
   guessMatrix = gM;
   constantMatrix = cM;
   nG = n;

   guessList = {};
   For[i = 0, i < nG, If[constantMatrix[[1, i]] == 1, Area[i] = guessMatrix[[1, i]],
     guessList = Append[guessList, {Area[i], guessMatrix[[1, i]]}] ], i++];
   For[i = 0, i < nG, If[constantMatrix[[2, i]] == 1, Cent[i] = guessMatrix[[2, i]],
     guessList = Append[guessList, {Cent[i], guessMatrix[[2, i]]}] ], i++];
   For[i = 0, i < nG, If[constantMatrix[[3, i]] == 1, Width[i] = guessMatrix[[1, i]],
     guessList = Append[guessList, {Width[i], guessMatrix[[3, i]]}] ], i++];

   model = 0;
   For[i = 0, i < nG,
    model = model + Abs[Area[i]] * Exp[-(x - Cent[i])^2 / (2 (Width[i])^2)], i++];

   myFit = BestFitParameters /. NonlinearRegress[finalData, model, guessList,
      x,
      RegressionReport → {BestFitParameters}, MaxIterations → maxIt];

   For[i = 0, i < nG, If[constantMatrix[[1, i]] == 0,
     mArea[i] = Abs[Area[i]] /. myFit, mArea[i] = guessMatrix[[1, i]]], i++];
   For[i = 0, i < nG, If[constantMatrix[[2, i]] == 0, mCent[i] = Cent[i] /. myFit,
     mCent[i] = guessMatrix[[2, i]], i++];
   For[i = 0, i < nG, If[constantMatrix[[3, i]] == 0, mWidth[i] = Abs[Width[i]] /. myFit,
     mWidth[i] = guessMatrix[[3, i]], i++];

   numList = {"n"};
   areaList = {"Area"};
   centerList = {"Center"};
   widthList = {"Width"};
   For[i = 0, i < nG,
    (
     numList = Append[numList, i];
     areaList = Append[areaList, mArea[i]];
     centerList = Append[centerList, mCent[i]];
     widthList = Append[widthList, mWidth[i]];
    ), i++];

   outValues = Transpose[{numList, areaList, centerList, widthList}];
   Print[MatrixForm[outValues]];

   finalModel = 0;
   For[i = 0, i < nG, finalModel =
     finalModel + Abs[mArea[i]] * Exp[-(x - mCent[i])^2 / (2 (mWidth[i])^2)], i++];

   finalPlot = Plot[finalModel, {x, startValue, endValue}, PlotRange → All,
     PlotStyle → {RGBColor[1, 0, 0]}, Axes → {True, False}];

   Show[compPlot, finalPlot];
   Return[{Delete[areaList, 1], Delete[centerList, 1], Delete[widthList, 1]}];
  )];
```

Heat Treated Composite Glass Data

The data is imported from a Tecmag file in which the data has been Fourier Transformed, phased, and baseline corrected. The header columns have been deleted.

In[119]:=
```
data = Import["/Users/Shared/Data/31P 1D NMR/65 MHz
     Data/070716 G Composite Glass/Guojing HT Glass 070716v2.txt", "Data"];
```

The data is normalized per mass per scan, which is necessary when one wishes to perform a quantitative analysis of the 31 P NMR data. It is not necessary in this particular notebook.

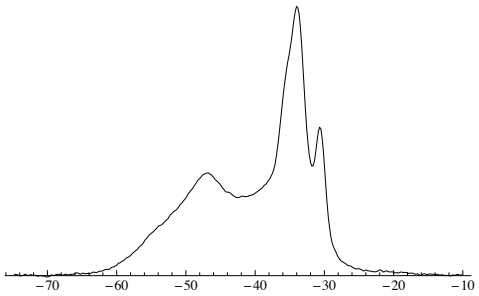
In[120]:=
```
mass = 0.0541;
scans = 64;
totalData = {};
For[i = 1, i < Length[data],
  totalData = Append[totalData, {data[[i, 3]], data[[i, 1]] / (mass * scans)}], i++];
```

A window of interest is defined, which both allows the fit function to focus its efforts on the NMR signal (rather than any artifacts in the outlying regions of the spectrum) and allows the user to more easily view the results of the fit algorithm.

In[124]:=
```
startValue = -75;
endValue = -10;
finalData = {};
For[i = 0, i < Length[totalData], If[totalData[[i, 1]] > startValue && totalData[[i, 1]] < endValue,
   finalData = Append[finalData, totalData[[i]]]], i++];
```

In[128]:=
```
plot2 = ListPlot[finalData, Joined → True,
  PlotRange → All, Axes → {True, False}, PlotStyle → {RGBColor[0, 0, 0]}]
```

Out[128]=



Fit Heat Treated Composite Glass with n Gaussians

First, a fit with five Gaussians is attempted. The variables for the five Gaussians are defined and then placed in matrix form ("guessmatrix"). All variables are to be fit, so a 3 by 5 matrix of zeros is entered into the constantMatrix. The data is then entered into the n Gaussian fit function below. (The variable "itFourGuess" was used as the variable name only because in the full data analysis notebook, several other variations of fits were attempted first. This variable name, in fact, is completely arbitrary, so long as it is used consistantly when plotting data. It is wise to use different names throughout a single notebook in order to avoid having a variable defined multiple times in the same notebook.)

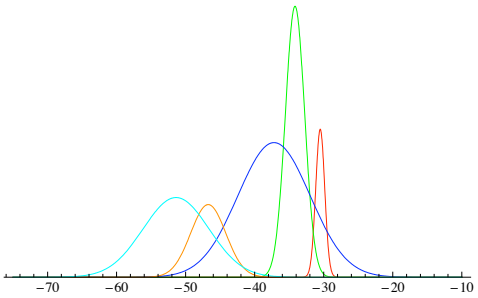
■ Iteration One: Five Gaussians

In[129]:=
```
A1guess = 26 000.;
A2guess = 43 000.;
A3guess = 19 000.;
A4guess = 13 000.;
A5guess = 10 300.;
C1guess = -30.5;
C2guess = -34.1;
C3guess = -37.3;
C4guess = -46.;
C5guess = -52.;
W1guess = 0.6;
W2guess = 1.2;
W3guess = 4.8;
W4guess = 2.7;
W5guess = 4.3;
guessMatrix = {{A1guess, A2guess, A3guess, A4guess, A5guess}, {C1guess, C2guess,
    C3guess, C4guess, C5guess}, { W1guess, W2guess, W3guess, W4guess, W5guess}};
constantMatrix = {{0, 0, 0, 0, 0, 0}, {0, 0, 0, 0, 0, 0}, {0, 0, 0, 0, 0, 0}};
itFourGuess = nGaussianFit[finalData, 500, guessMatrix, constantMatrix, 5, plot2];
```

n	Area	Center	Width
1	28 972.6	-30.5065	0.650526
2	53 024.9	-34.1594	1.39314
3	26 350.1	-37.201	5.22854
4	14 219.6	-46.73	2.54598
5	15 597.4	-51.3924	4.7799

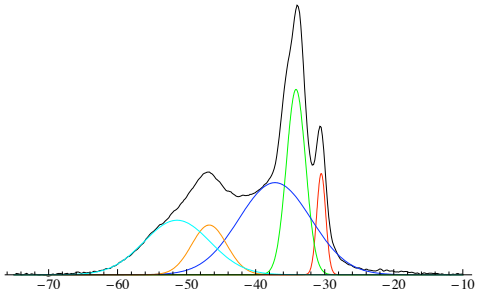
In[147]:=
```
peakOne = itFourGuess[[1, 1]] * Exp[-(x - itFourGuess[[2, 1]]) ^ 2 / (2 (itFourGuess[[3, 1]]) ^ 2)];
peakTwo =  itFourGuess[[1, 2]] * Exp[-(x - itFourGuess[[2, 2]]) ^ 2 / (2 (itFourGuess[[3, 2]]) ^ 2)];
peakThree =  itFourGuess[[1, 3]] * Exp[-(x - itFourGuess[[2, 3]]) ^ 2 / (2 (itFourGuess[[3, 3]]) ^ 2)];
peakFour = itFourGuess[[1, 4]] * Exp[-(x - itFourGuess[[2, 4]]) ^ 2 / (2 (itFourGuess[[3, 4]]) ^ 2)];
peakFive = itFourGuess[[1, 5]] * Exp[-(x - itFourGuess[[2, 5]]) ^ 2 / (2 (itFourGuess[[3, 5]]) ^ 2)];
function = peakOne + peakTwo + peakThree + peakFour + peakFive;
peakPlots =
 Plot[{peakOne, peakTwo, peakThree, peakFour, peakFive}, {x, startValue, endValue},
  PlotStyle → {RGBColor[1, 0, 0], RGBColor[0, 1, 0], RGBColor[0, 0, 1], RGBColor[1, 0.5, 0],
    RGBColor[0, 1, 1], RGBColor[1, 0, 1]}, PlotRange → All, Axes → {True, False}]
```

Out[153]=



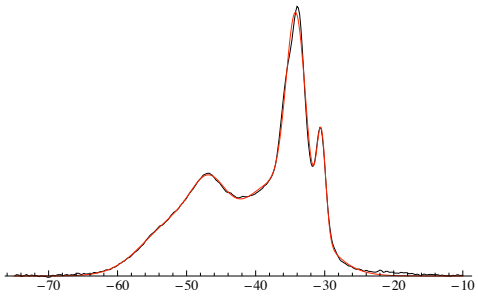
In[154]:=
```
Show[plot2, peakPlots]
```

Out[154]=



In[155]:=
```
Show[plot2, Plot[function, {x, startValue, endValue},
  PlotStyle → {RGBColor[1, 0, 0]}, PlotRange → All, Axes → {True, False}]]
```

Out[155]=



As can be seen by the final comparison of real data (black) and the results of the fit function, five Gaussians results in a nice fit everywhere but on the tallest peak in the spectrum, suggesting that at least six peaks will be needed.

■ Iteration Two: Six Gaussians

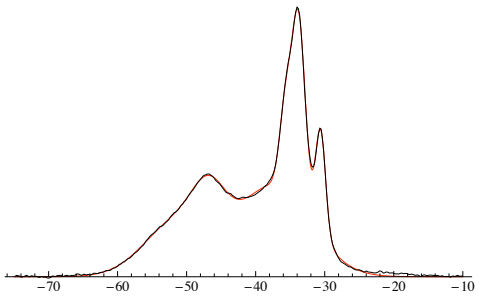
The variables for the six Gaussians are defined as for the five Gaussian fit and are then placed in matrix form ("guessmatrix"). All variables are to be fit, so a 3 by 6 matrix of zeros is entered into the constantMatrix. The data is then entered into the n Gaussian fit function below.

In[156]:=
```
A1guess = 25 000.;
A2guess = 20 000.;
A3guess = 20 000.;
A4guess = 5000.;
A5guess = 25 000.;
A6guess = 5000.;
C1guess = -30.52;
C2guess = -34.2;
C3guess = -34.4;
C4guess = -36.3;
C5guess = -47.4;
C6guess = -55.7;
W1guess = 0.55;
W2guess = 1.2;
W3guess = 1.1;
W4guess = 2.;
W5guess = 1.7;
W6guess = 2.3;
guessMatrix = {{A1guess, A2guess, A3guess, A4guess, A5guess, A6guess},
   {C1guess, C2guess, C3guess, C4guess, C5guess, C6guess},
   {W1guess, W2guess, W3guess, W4guess, W5guess, W6guess}};
constantMatrix = {{0, 0, 0, 0, 0, 0}, {0, 0, 0, 0, 0, 0}, {0, 0, 0, 0, 0, 0}};
itFiveGuess = nGaussianFit[finalData, 500, guessMatrix, constantMatrix, 6, plot2];
```

n	Area	Center	Width
1	30 087.1	-30.605	0.74212
2	21 132.9	-35.7597	0.831716
3	53 725.3	-33.8202	1.00532
4	25 863.	-37.25	5.28314
5	12 548.7	-46.7604	2.40818
6	16 291.5	-50.9883	4.95219

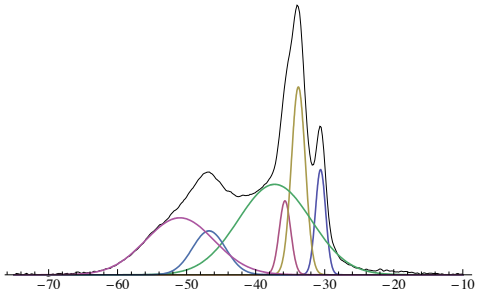
In[177]:=
```
peakOne = itFiveGuess[[1, 1]] * Exp[-(x - itFiveGuess[[2, 1]])^2 / (2 (itFiveGuess[[3, 1]])^2)];
peakTwo = itFiveGuess[[1, 2]] * Exp[-(x - itFiveGuess[[2, 2]])^2 / (2 (itFiveGuess[[3, 2]])^2)];
peakThree = itFiveGuess[[1, 3]] * Exp[-(x - itFiveGuess[[2, 3]])^2 / (2 (itFiveGuess[[3, 3]])^2)];
peakFour = itFiveGuess[[1, 4]] * Exp[-(x - itFiveGuess[[2, 4]])^2 / (2 (itFiveGuess[[3, 4]])^2)];
peakFive = itFiveGuess[[1, 5]] * Exp[-(x - itFiveGuess[[2, 5]])^2 / (2 (itFiveGuess[[3, 5]])^2)];
peakSix = itFiveGuess[[1, 6]] * Exp[-(x - itFiveGuess[[2, 6]])^2 / (2 (itFiveGuess[[3, 6]])^2)];
function = peakOne + peakTwo + peakThree + peakFour + peakFive + peakSix;
totalPlot = Plot[function, {x, startValue, endValue},
   PlotStyle → {RGBColor[1, 0, 0]}, PlotRange → All, Axes → {True, False}];
Show[totalPlot, plot2]
peakPlots1 = Plot[{peakOne, peakTwo, peakThree, peakFour, peakFive, peakSix},
   {x, startValue, endValue}, PlotStyle → Thickness[0.0033],
   PlotStyle → {RGBColor[1, 0, 0], RGBColor[0, 1, 0], RGBColor[0, 0, 1], RGBColor[1, 0.5, 0],
     RGBColor[0, 1, 1], RGBColor[1, 0, 1]}, PlotRange → All, Axes → {True, False}];
```

Out[185]=



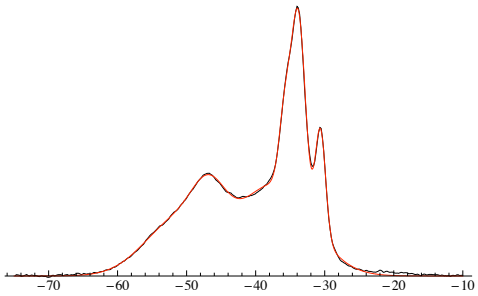
In[187]:=
```
quickPrint = Show[plot2, peakPlots1]
```

Out[187]=



In[188]:=
```
Show[plot2, Plot[function, {x, startValue, endValue},
  PlotStyle → {RGBColor[1, 0, 0]}, PlotRange → All, Axes → {True, False}]]
```

Out[188]=



As can be seen above, the real data (black) and the results of the fit function match remarkably well. The results shown here are those used in the study of the calcium lanthanum phosphate composite glass-ceramic material.

■ Iteration Three: Six Gaussians (with peak holds)

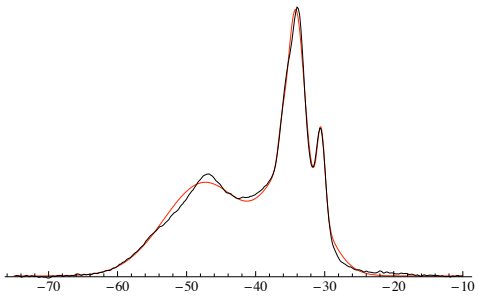
This final iteration demonstrates how to fix certain values when using the fit funciton. In this case, the peak centers from separate studies of heat treated calcium phosphate and heat treated lanthanum metaphosphate are fixed while the peak widths and peak heights are allowed to vary until the best fit is found. As before, the variables for the six Gaussians are defined and are then placed in matrix form ("guessmatrix"). Because the peak centers are to be fixed, an array of ones are included in the second row of the matrix (or, in the form shown below, the second element in the first dimension is an array of ones). The data is then entered into the n Gaussian fit function below.

In[189]:=
```
A1guess = 24 404.6;
A2guess = 43 850.1;
A3guess = 30 310.;
A4guess = 5533.;
A5guess = 2744.;
A6guess = 2961.;
C1guess = -30.52;
C2guess = -34.2;
C3guess = -34.4;
C4guess = -36.3;
C5guess = -47.4;
C6guess = -55.7;
W1guess = 0.59;
W2guess = 1.14;
W3guess = 3.7;
W4guess = 0.434;
W5guess = 3.5;
W6guess = 3.;
guessMatrix = {{A1guess, A2guess, A3guess, A4guess, A5guess, A6guess},
   {C1guess, C2guess, C3guess, C4guess, C5guess, C6guess},
   {W1guess, W2guess, W3guess, W4guess, W5guess, W6guess}};
constantMatrix = {{0, 0, 0, 0, 0, 0}, {1, 1, 1, 1, 1, 1}, {0, 0, 0, 0, 0, 0}};
itFiveGuess = nGaussianFit[finalData, 500, guessMatrix, constantMatrix, 6, plot2];
```

n	Area	Center	Width
1	24 068.2	-30.52	0.574427
2	44 440.5	-34.2	1.16088
3	29 602.3	-34.4	3.81256
4	5849.24	-36.3	0.489063
5	26 693.5	-47.4	5.89789
6	233.542	-55.7	102 992.

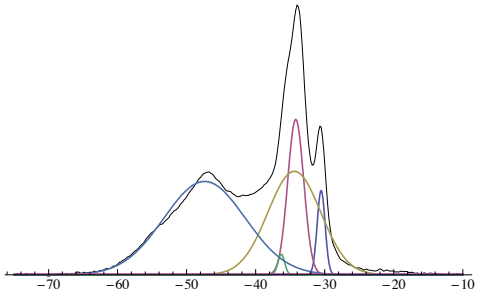
In[210]:=
```
peakOne = itFiveGuess[[1, 1]] * Exp[-(x - itFiveGuess[[2, 1]]) ^ 2 / (2 (itFiveGuess[[3, 1]]) ^ 2)];
peakTwo = itFiveGuess[[1, 2]] * Exp[-(x - itFiveGuess[[2, 2]]) ^ 2 / (2 (itFiveGuess[[3, 2]]) ^ 2)];
peakThree = itFiveGuess[[1, 3]] * Exp[-(x - itFiveGuess[[2, 3]]) ^ 2 / (2 (itFiveGuess[[3, 3]]) ^ 2)];
peakFour = itFiveGuess[[1, 4]] * Exp[-(x - itFiveGuess[[2, 4]]) ^ 2 / (2 (itFiveGuess[[3, 4]]) ^ 2)];
peakFive = itFiveGuess[[1, 5]] * Exp[-(x - itFiveGuess[[2, 5]]) ^ 2 / (2 (itFiveGuess[[3, 5]]) ^ 2)];
peakSix = itFiveGuess[[1, 6]] * Exp[-(x - itFiveGuess[[2, 6]]) ^ 2 / (2 (itFiveGuess[[3, 6]]) ^ 2)];
function = peakOne + peakTwo + peakThree + peakFour + peakFive + peakSix;
totalPlot = Plot[function, {x, startValue, endValue},
   PlotStyle → {RGBColor[1, 0, 0]}, PlotRange → All, Axes → {True, False}];
Show[totalPlot, plot2]
peakPlots1 = Plot[{peakOne, peakTwo, peakThree, peakFour, peakFive, peakSix},
   {x, startValue, endValue}, PlotStyle → Thickness[0.0033],
   PlotStyle → {RGBColor[1, 0, 0], RGBColor[0, 1, 0], RGBColor[0, 0, 1], RGBColor[1, 0.5, 0],
     RGBColor[0, 1, 1], RGBColor[1, 0, 1]}, PlotRange → All, Axes → {True, False}];
```

Out[218]=



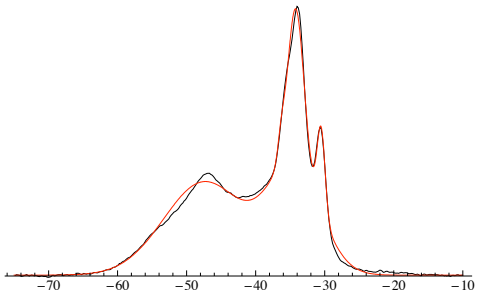
In[220]:=
```
Show[plot2, peakPlots1]
```

Out[220]=



In[221]:=
```
Show[plot2, Plot[function, {x, startValue, endValue},
  PlotStyle → {RGBColor[1, 0, 0]}, PlotRange → All, Axes → {True, False}]]
```

Out[221]=



As can be seen above, the real data (black) and the results of the fit function do not match as well in either the five- or six-Gaussian fit attempts, and one of the peaks returns peak width that several orders of magnitude larger than the others, which is not expected from this data. This suggests that the data is not simply a spectrum of the two model chemical shift references.

Appendix I

Single Self Diffusion Coefficient Measurement with PGSE with Square Pulses: Example Mathematica Code

This notebook demonstrates the use of the NonlinearRegress package to fit STRAFI data. In this particular example, the attenuation profile of a compound with a known self-diffusion coefficient - in this case, glycerol - is used to determine the magnitude of the magnetic field gradient. If the quality of the data is high, then both the gradient and the T2 of the diffusion calibration compound can be fit at the same time, as is done here.

Import Data

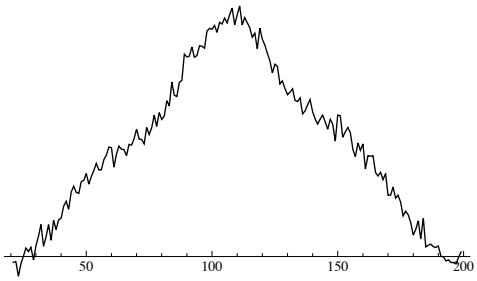
First, the relevant experimental parameters (number of two dimensional scans, number of one dimensional points) are entered as variables, and a time list of delays is created. The data is then separated into a two dimensional matrix of one dimensional arrays that consist of one free induction decay (FID). Unlike the analyses in which there is spectroscopic resolution to provide the spectroscopist with insight into the number of diffusing species being probed, the steady gradient present in the STRAFI experiment destroys chemical shift resolution. As a result, the full echo produced by the spin echo experiment is acquired, and the data will be in a (time, real) format. Once properly processed, the echo itself is numerically integrated, and is transposed with the timeList provided by the experimenter.

```
num2D = 45;
numPoints = 1024;
timeList = {0.0425, 0.0625, 0.0825, 0.1025, 0.1225, 0.1425, 0.1625,
   0.1825, 0.2025, 0.2225, 0.2425, 0.2625, 0.2825, 0.3025, 0.3225, 0.3425,
   0.3625, 0.3825, .4025, 0.4225, 0.4425, 0.4625, 0.4825, 0.5025, 0.5225, 0.5425,
   0.5625, 0.5825, 0.6025, 0.6225, 0.6425, 0.6625, 0.6825, 0.7025, 0.7225, 0.7425,
   0.7625, 0.7825, 0.8025, 0.8225, 0.8425, 0.8625, 0.8825, 0.9025, 0.9225};
data = Import["/Users/Shared/Data/Fringe Field Experiments/Black 300
     Gradient Measurement/Eighth Attempt/gradientMeasure8.txt", "Data"];

totalData = Table[{}, {i, 1, num2D}];
For[i = 0, i < num2D,
  (
   For[j = 0, j < numPoints,
     (
      totalData[[i]] =
        Append[totalData[[i]], {data[[j + (i - 1) * numPoints, 3]], data[[j + (i - 1) * numPoints, 1]]}];
     ), j++];
  ), i++];

startValue = 20;
endValue = 200;
finalData = Table[{}, {i, 1, num2D}];
For[i = 0, i < num2D,
  (
   For[j = 0, j < numPoints, If[totalData[[i, j, 1]] > startValue && totalData[[i, j, 1]] < endValue,
      finalData[[i]] = Append[finalData[[i]], totalData[[i, j]]]], j++];
  ),
  i++];
```

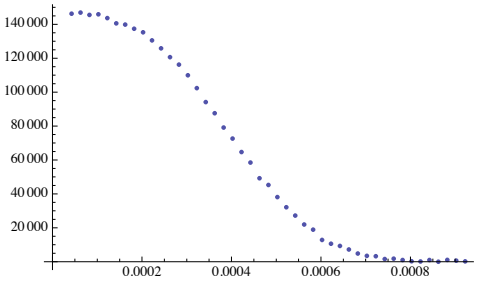
```
plot1 = ListPlot[finalData[[1]], Joined → True, PlotRange → All,
  Axes → {True, False}, PlotStyle → {RGBColor[0, 0, 0], Thickness[0.003`]}]
```




```
tempSum = 0;
areaList = {};
For[i = 0, i < num2D,
  (
   tempSum = 0;
   For[j = 0, j < Length[finalData[[i]]], tempSum = tempSum + finalData[[i, j, 2]], j++];
   areaList = Append[areaList, tempSum];
  ), i++];
```

```
expData = Transpose[{timeList / 1000, areaList}];
```

```
plot1 = ListPlot[expData, PlotRange → All, AxesOrigin → {0, 0}]
```



Two pulse Hahn spin echo, ordinary diffusion

In order to perform the analysis, the NonlinearRegression package must first be loaded.

```
Needs["NonlinearRegression`"]
```

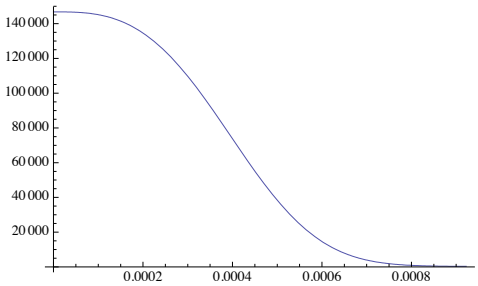
The known inputs to the steady gradient spin echo experiment with a diffusion standard will be the magnetogyric ratio for the nucleus being investigated (in this case, that of protons), and the known self diffusion coefficient. In this case, both the self diffusion coefficient and the T2 will be fit. Included in the Regression Report will be the paramters and the confidence interval table, which provides the uncertainty of the gradient measurement.

```
γ = 267.522 * 10^6;
d = 2.299 10^-9;
```

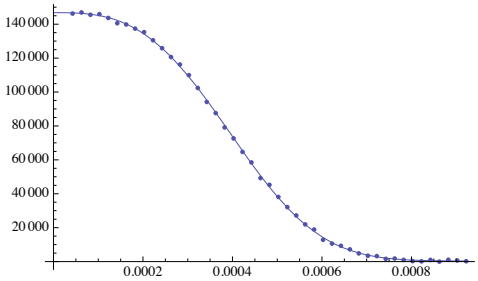
```
Clear[A, G, T2, b];
model = A * Exp[-2 * τ / T2] * Exp[(-2 * γ^2 * d * G^2 * τ^3) / 3] + b;
datafit = NonlinearRegress[expData, model, {{G, 9.9}, {T2, 0.505}, {A, 120000}, {b, 300.}},
   τ, RegressionReport → {BestFitParameters, ParameterCITable}];
fit = BestFitParameters /. datafit;
CITable = ParameterCITable /. datafit;
CITable
```

	Estimate	Asymptotic SE	CI
G	9.90452	0.0553678	{9.7927, 10.0163}
T2	0.505921	3.16372	{-5.88334, 6.89518}
A	146494.	623.471	{145235., 147753.}
b	308.451	220.031	{-135.911, 752.813}

```
A = A /. fit;
G = G /. fit;
T2 = T2 /. fit;
b = b /. fit;
plot2 = Plot[model, {τ, 0, expData[[Length[expData], 1]]}]
```




```
plot3 = Show[plot1, plot2]
```



As is seen above, the results of the fit match the experimentally acquired data closely. The confidence interval table above indicates that the gradient strength is 9.9 T/m, with an uncertainty of +/- 0.1 T/m.

Appendix J

Single Self Diffusion Coefficient Measurement with PGSE with Square Pulses: Example Mathematica Code

This notebook demonstrates how the STRAFI CPMG experimental data is fit in *Mathematica*. This data is the result of a STRAFI CPMG experiment performed at 200 C on the B1 sample discussed in the chapter on self diffusion measurements. An experiment on glycerol at 25 C indicated that the gradient strength was G = 12.4 T/m.

Import 200 C STRAFI CPMG Data

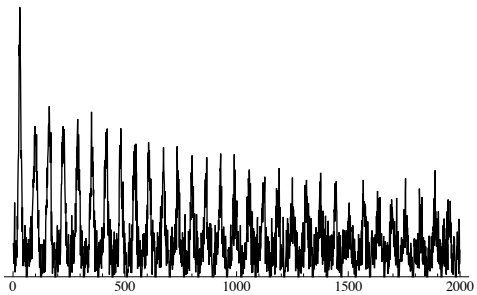
The relevant experimental parameters are entered : The number of 2D scans (num2D), number of acquired points (numPoints), and the time delays of the first echo (timeList). The acquisition data is then imported. In this case, the data is not Fouerier Transformed, but rather the sequence of CPMG echos are imported as they were acquired.

```
num2D = 40;
numPoints = 4096;
timeList =
  N[{0.1, 0.12, 0.14, 0.16, 0.18, 0.2, 0.22, 0.24, 0.26, 0.28, 0.3, 0.32, 0.34, 0.36, 0.38,
     0.4, 0.42, 0.44, 0.46, 0.48, 0.5, 0.6, 0.7, 0.8, 0.9, 1, 1.2, 1.4, 1.6, 1.8,
     2, 2.4, 2.6, 2.8, 3, 3.2, 3.4, 3.6, 3.8, 4} / 1000];
data = Import["/Users/Shared/Data/1H NMR Data/300 MHz Data/110322 B1 Full
     Decay Experiments/1H STRAFI CPMG B1 200C fullDecay.txt", "Data"];
data =
  Drop[
   data,
   4];

totalData = Table[{}, {i, 1, num2D}];
For[i = 0, i < num2D,
  (
   For[j = 0, j < numPoints,
     (
      totalData[[i]] = Append[totalData[[i]], {data[[j + (i - 1) * numPoints, 3]],
          Abs[data[[j + (i - 1) * numPoints, 1]] + data[[j + (i - 1) * numPoints, 2]] * I]}];
     ), j++];
  ), i++];

startValue = 0;
endValue = 2000;
finalData = Table[{}, {i, 1, num2D}];
For[i = 0, i < num2D,
  (
   For[j = 0, j < numPoints, If[totalData[[i, j, 1]] > startValue && totalData[[i, j, 1]] < endValue,
      finalData[[i]] = Append[finalData[[i]], totalData[[i, j]]]], j++];
  ),
  i++];

plot1 = ListPlot[finalData[[1]], Joined → True, PlotRange → All,
  Axes → {True, False}, PlotStyle → {RGBColor[0, 0, 0], Thickness[0.003`]}]
```



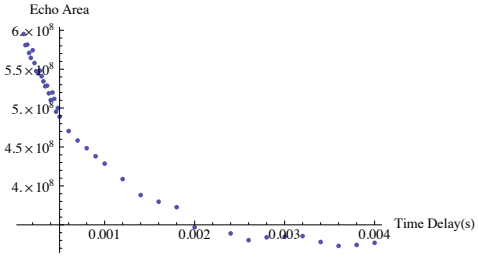
All acquisitions are then summed together to get a list of summed data at each time setting.

```
tempSum = 0;
areaList = {};
For[i = 0, i < num2D,
  (
   tempSum = 0;
   For[j = 0, j < Length[finalData[[i]]], tempSum = tempSum + finalData[[i, j, 2]], j++];
   areaList = Append[areaList, tempSum];
  ), i++];
```

Once the summed data is transposed with the time data, the signal versus time can be plotted for the STRAFI CPMG experiment.

```
expData = Transpose[{timeList, areaList}];

plot2 = ListPlot[expData, PlotRange → All, AxesLabel → {"Time Delay(s)", "Echo Area"}]
```



The data can now be fit two different ways: The first method uses the NonlinearRegress function to fit the two self diffusion coefficients and the T2. The second method fixes the T2 as determined from the CPMG train of the first acquisition, reducing the number of variables to fit by one.

Fiting the FID data - Two D's

The parameters that must be fixed for the STRAFI CPMG model NonlinearRegression fit include the magnetogyric ratio (γ) and the maximum gradient strength(G).

```
γ = 267.522 * 10^6;
G = 12.39744986704897;
```

The model equation in this case is as given in the discussion on Diffusion Methods earlier in this work.

```
Clear[A, d1, d2, T2, B, frac];
Needs["NonlinearRegression`"]
model = A * Exp[-2 * τ / T2] * (frac * Exp[-2 * γ^2 * d1 * G^2 * τ^3 / 3] + (1 - frac) * Exp[-2 * γ^2 * d2 * G^2 * τ^3 / 3]) + B;

dataFit = NonlinearRegress[expData, model, {{d1, 2.1 * 10^(-9)}, {d2, 2.1 * 10^(-12)},
    {T2, 0.005}, {A, 6 * 10^8 - 3.5 * 10^8}, {B, 3.5 * 10^8}, {frac, 0.5}},
   τ, RegressionReport → {BestFitParameters, ParameterCITable}];
fit = BestFitParameters /. dataFit;
CITable = ParameterCITable /. dataFit;
```

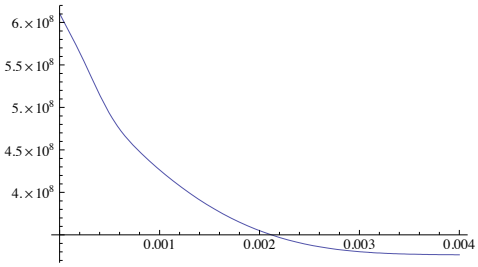
The Confidence Interval table displays the best fit parameters and the corresponding undertainty.

```
CITable
```

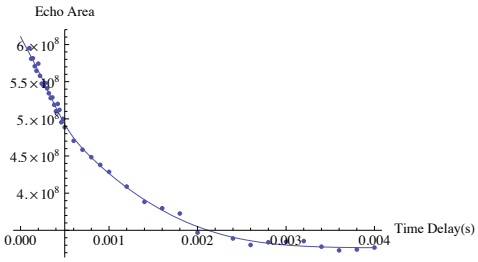
	Estimate	Asymptotic SE	CI
d1	1.48048×10^{-9}	3.64965×10^{-10}	$\{7.38777\times10^{-10}, 2.22217\times10^{-9}\}$
d2	8.68158×10^{-12}	1.85547×10^{-12}	$\{4.91081\times10^{-12}, 1.24523\times10^{-11}\}$
T2	0.00247282	0.000143292	{0.00218162, 0.00276402}
A	2.84104×10^{8}	2.92692×10^{-10}	$\{2.84104\times10^{8}, 2.84104\times10^{8}\}$
B	3.26442×10^{8}	2.54422×10^{-10}	$\{3.26442\times10^{8}, 3.26442\times10^{8}\}$
frac	0.157217	0.0321227	{0.0919358, 0.222498}

The best fit parameters can then be entered into the model equation and compared with the data :

```
d1 = Abs[d1] /. fit;
d2 = Abs[d2] /. fit;
T2 = Abs[T2] /. fit;
A = A /. fit;
B = B /. fit;
frac = frac /. fit;
plot3 = Plot[model, {τ, 0, timeList[[Length[timeList]]]}, PlotRange → All]
```




```
plot4 = Show[plot2, plot3]
```



The best fit parameter model fits the data quite well. The T2 determined by the model is also relatively close to (and within error of) that measured with the CPMG experiment (2.71 ms).

Fiting the FID data with T2 fixed at its calculated value (T2 = 0.00271335) - with two D's

The parameters that must be fixed for the STRAFI CPMG model with fixed T2 NonlinearRegression fit include the magnetogyric ratio (γ), the maximum gradient strength(G) and T2.

```
γ = 267.522 * 10^6;
G = 12.39744986704897;
T2 = 0.0027133542267033066;
```

The fit is then performed as before, but without T2 as a parameter to be fitted.

```
Clear[A, d1, d2, B, frac];
Needs["NonlinearRegression`"]
model = A * Exp[-2 * τ / T2] * (frac * Exp[-2 * γ^2 * d1 * G^2 * τ^3 / 3] + (1 - frac) * Exp[-2 * γ^2 * d2 * G^2 * τ^3 / 3]) + B;

dataFit = NonlinearRegress[expData, model, {{d1, 1. * 10^(-9)},
    {d2, 1. * 10^(-11)}, {A, 6 * 10^8 - 3.5 * 10^8}, {B, 3.5 * 10^8}, {frac, 0.5}},
   τ, RegressionReport → {BestFitParameters, ParameterCITable}];
fit = BestFitParameters /. dataFit;
CITable = ParameterCITable /. dataFit;

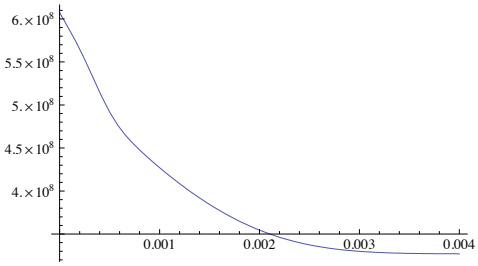
fit
```

$$\{d1 \to 1.45329 \times 10^{-9},\ d2 \to 1.07563 \times 10^{-11},\ A \to 2.80483 \times 10^{8},\ B \to 3.26964 \times 10^{8},\ frac \to 0.19184\}$$

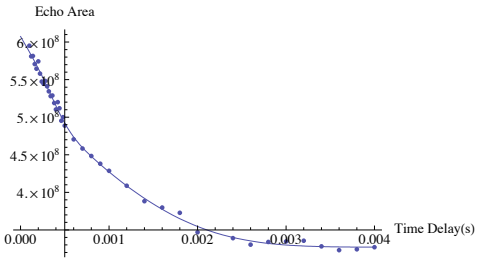
```
CITable
```

	Estimate	Asymptotic SE	CI
d1	1.45329×10^{-9}	2.63744×10^{-10}	$\{9.17863 \times 10^{-10},\ 1.98872 \times 10^{-9}\}$
d2	1.07563×10^{-11}	1.52827×10^{-12}	$\{7.6537 \times 10^{-12},\ 1.38588 \times 10^{-11}\}$
A	2.80483×10^{8}	2.46527×10^{-11}	$\{2.80483 \times 10^{8},\ 2.80483 \times 10^{8}\}$
B	3.26964×10^{8}	3.61516×10^{-11}	$\{3.26964 \times 10^{8},\ 3.26964 \times 10^{8}\}$
frac	0.19184	0.0182332	{0.154825, 0.228855}

```
d1 = d1 /. fit;
d2 = d2 /. fit;
A = A /. fit;
B = B /. fit;
frac = frac /. fit;
plot3 = Plot[model, {τ, 0, timeList[[Length[timeList]]]}, PlotRange → All]
```



```
plot4 = Show[plot2, plot3]
```



These best fit parameters also fit the data rather well, and the best fit parameters from this analysis are within error of those found by the non-fixed T2 method above.

Appendix K

Single Self Diffusion Coefficient Measurement with STRAFI: Example Mathematica Code

This notebook demonstrates how to fit pulsed gradient spin echo experiments (PGSE) using square pulses at a predetermined gradient strength. In this particular example, a PEO and LiTFSI system is being studied with 19F NMR which probes the TFSI anion.

Experimental Note : The experiment was run with G = 7 on the LapNMR. Glycerol calibration indicates that G = 3.8 T/m.

Import PGSE Data

First, the number of two dimensional scans (num2D) and the number of one dimensional acquisition points (numPoints) is entered, along with the gradient list given as a percentage of the maximum gradient used in the experiment. This data was processed prior to being imported into *Mathematica* using the NDFT command in NTNMR followed by any necessary phasing. The data is then imported, and the first four lines - which include the data headers from the NTNMR software - are dropped. The data is then placed into a matrix of NMR spectral data.

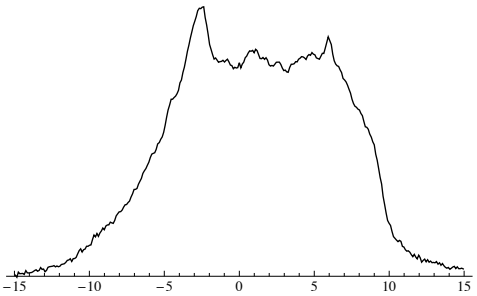
In[188]:=
```
num2D = 20;
numPoints = 4096;
gradList =
  gradList = {1, 6, 11, 16, 21, 26, 31, 36, 41, 46, 51, 56, 61, 66, 71, 76, 81, 86, 91, 96} / 100;
data = Import["/Users/Shared/Data/19F NMR Data/110408 PEO Data/19F PGSE PEO 90 C.txt",
   "Data"];
data = Drop[data, 4];
```

In[193]:=
```
totalData = Table[{}, {i, 1, num2D}];
For[i = 0, i < num2D,
  (
   For[j = 0, j < numPoints,
     (
      totalData[[i]] =
        Append[totalData[[i]], {data[[j + (i - 1) * numPoints, 3]], data[[j + (i - 1) * numPoints, 1]]}];
     ), j++];
  ), i++];
```

In[195]:=
```
startValue = -15;
endValue = 15;
finalData = Table[{}, {i, 1, num2D}];
For[i = 0, i < num2D,
  (
   For[j = 0, j < numPoints, If[totalData[[i, j, 1]] > startValue && totalData[[i, j, 1]] < endValue,
      finalData[[i]] = Append[finalData[[i]], totalData[[i, j]]]], j++];
  ),
  i++];
```

In[199]:=
```
plot1 = ListPlot[finalData[[1]], Joined → True, PlotRange → All,
  Axes → {True, False}, PlotStyle → {RGBColor[0, 0, 0], Thickness[0.003`]}]
```

Out[199]=



The data is then numerically integrated over the range of interest and transposed into a list of gradient settings and integrated

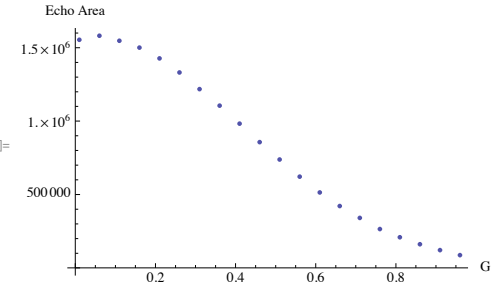
intensities so the data can be fit to extract the self diffusion coefficient.

In[200]:=
```
tempSum = 0;
areaList = {};
For[i = 0, i < num2D,
  (
   tempSum = 0;
   For[j = 0, j < Length[finalData[[i]]], tempSum = tempSum + finalData[[i, j, 2]], j++];
   areaList = Append[areaList, tempSum];
  ), i++];
```

In[203]:=
```
expData = Transpose[{gradList, areaList}];
```

In[204]:=
```
plot1 =
 ListPlot[expData, PlotRange → All, AxesOrigin → {0, 0}, AxesLabel → {"G", "Echo Area"}]
```

Out[204]=



Two pulse Hahn spin echo, ordinary diffusion

The NonlinearRegression package must be imported :

In[205]:=
```
Needs["NonlinearRegression`"]
```

The parameters that must be fixed for the PGSE model NonlinearRegression fit include the magnetogyric ratio (γ), the maximum gradient strength(g), the gradient duration (δ) and the diffusion time (Δ).

In[206]:=
```
γ = 251.815 * 10^6;
G = 3.8;
δ = 0.005;
Δ = 0.015075;
```

In[210]:=
```
Clear[A, b, g, d];
model = A * Exp[-γ^2 * d * G^2 * g^2 * δ^3 * (Δ/δ - 1/3)] + b;
```

In[212]:=
```
dataFit = NonlinearRegress[expData, model, {{d, 10^-11}, {A, 380 000.}, {b, 100.}},
   g, RegressionReport → {BestFitParameters, ParameterCITable}];
fit = BestFitParameters /. dataFit;
CITable = ParameterCITable /. dataFit;
```

The NonlinearRegress function returns a confidence interval table of the fit for each parameter :

In[215]:=
```
CITable
```

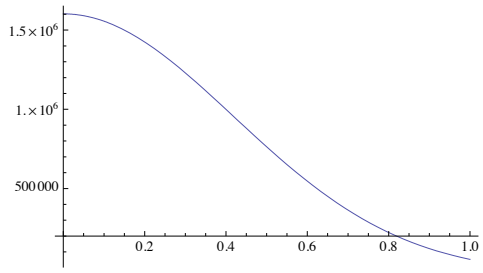
Out[215]//TableForm=

	Estimate	Asymptotic SE	CI
d	9.30782×10^{-12}	7.73314×10^{-14}	$\{9.14467\times10^{-12}, 9.47097\times10^{-12}\}$
A	1.64389×10^{6}	6.07231×10^{-31}	$\{1.64389\times10^{6}, 1.64389\times10^{6}\}$
b	-41463.3	1.50106×10^{-30}	{-41463.3, -41463.3}

The fit can then be plotted against the acquired data :

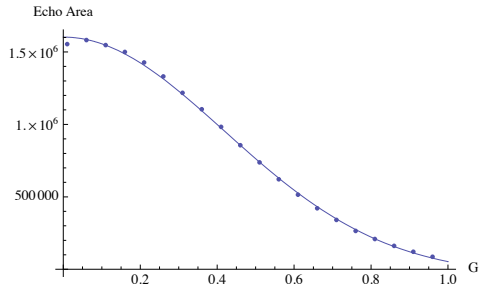
In[216]:=
```
A = A /. fit;
d = d /. fit;
b = b /. fit;
plot2 = Plot[model, {g, 0, 1}, PlotRange → All]
```

Out[219]=



In[220]:=
```
plot3 = Show[plot1, plot2]
```

Out[220]=



As can be seen, the fit to the data is quite good. This could be the end of the analysis, but often people want to fit and/or display the data on a semilog plot. The data analysis below demonstrates how this is done.

Changing to a log - x^2 graph ...

In[221]:=
```
Needs["NonlinearRegression`"]
```

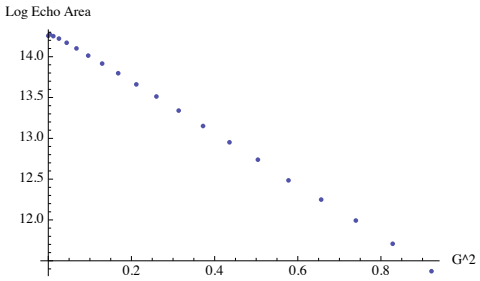
First the data is converted to a semilog versus g^2 format:

In[222]:=
```
logExpData = Transpose[{gradList^2, Log[areaList]}];
```

We can now plot the data to make sure things look linear, as the model equation suggests that it should :

In[223]:=
```
plot4 = ListPlot[logExpData, AxesLabel → {"G^2", "Log Echo Area"}]
```

Out[223]=



The data is then fit as above, but this time the model equation will be linear.

In[224]:=
```
γ = 251.815 * 10^6;
G = 3.8;
δ = 0.005;
Δ = 0.015075;
```

In[228]:=
```
Clear[b, g, d];
model = -γ^2 * d * G^2 * g * δ^3 * (Δ/δ - 1/3) + b;
```

In[230]:=
```
dataFit = NonlinearRegress[logExpData, model, {{d, 10^-11}, {b, 100.}},
   g, RegressionReport → {BestFitParameters, ParameterCITable}];
fit = BestFitParameters /. dataFit;
CITable = ParameterCITable /. dataFit;
```

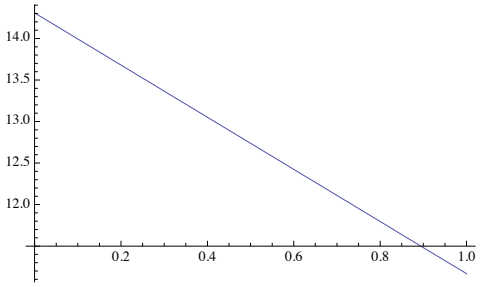
In[233]:=
```
CITable
```

Out[233]//TableForm=

	Estimate	Asymptotic SE	CI
d	1.02299×10^{-11}	5.13151×10^{-14}	$\{1.01221\times10^{-11}, 1.03377\times10^{-11}\}$
b	14.3079	0.00677531	{14.2936, 14.3221}

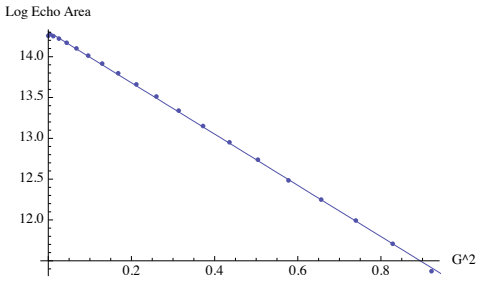
In[234]:=
```
d = Abs[d] /. fit;
b = b /. fit;
plot5 = Plot[model, {g, 0, 1}, PlotRange → All]
```

Out[236]=



In[237]:=
```
plot6 = Show[plot4, plot5]
```

Out[237]=



Again the data looks very good, and is reasonably close to that seen in the first analysis above. The small difference arises from numerical integration over a small baseline offset. This can be corrected by subtracting the baseline offset found in the first analysis ("b") from the data before taking the natural log of the data. The following analysis demonstrates this procedure.

Changing to a log - x^2 graph and subtracting "b" from areas

In[238]:=
```
Needs["NonlinearRegression`"]
```

The "b" from the first (nonlinear) analysis is defined :

In[239]:=
```
b = -41463.29798775784;
```

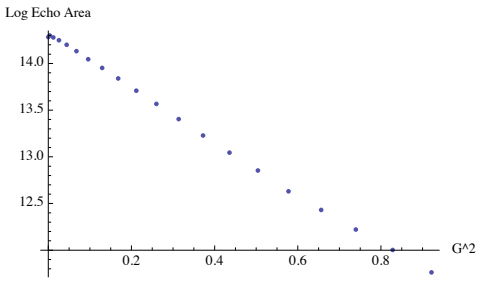
This is then subtracted from the integrated data ("areaList") before taking the natural log of the data :

In[240]:=
```
logExpData = Transpose[{gradList^2, Log[areaList - b]}];
```

The analysis then proceedes as in the second analysis :

In[241]:=
```
plot4 = ListPlot[logExpData, AxesLabel → {"G^2", "Log Echo Area"}]
```

Out[241]=



In[242]:=
```
γ = 251.815 * 10^6;
G = 3.8;
δ = 0.005;
Δ = 0.015075;
```

In[246]:=
```
Clear[b, g, d];
model = -γ^2 * d * G^2 * g * δ^3 * (Δ/δ - 1/3) + b;
```

In[248]:=
```
dataFit = NonlinearRegress[logExpData, model, {{d, 10^-11}, {b, 100.}},
   g, RegressionReport → {BestFitParameters, ParameterCITable}];
fit = BestFitParameters /. dataFit;
CITable = ParameterCITable /. dataFit;
```

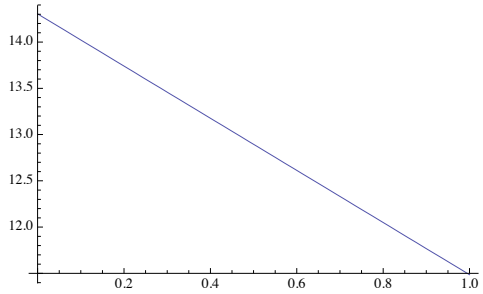
In[251]:=
```
CITable
```

Out[251]//TableForm=

	Estimate	Asymptotic SE	CI
d	9.18045×10^{-12}	6.4014×10^{-14}	$\{9.04596\times10^{-12}, 9.31494\times10^{-12}\}$
b	14.3037	0.008452	{14.286, 14.3215}

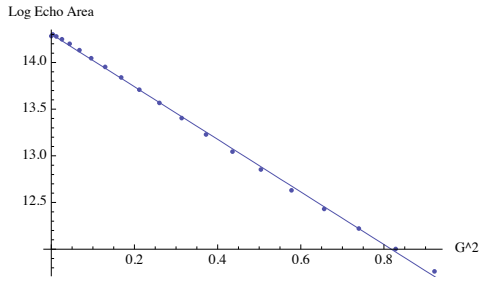
In[252]:=
```
d = Abs[d] /. fit;
b = b /. fit;
plot5 = Plot[model, {g, 0, 1}, PlotRange → All]
```

Out[254]=



In[255]:=
```
plot6 = Show[plot4, plot5]
```

Out[255]=



Again, the data fit is quite good. More importantly, the quantified self diffusion coefficient is within error of that measured by the first proceedure.

Appendix L

Single Self Diffusion Coefficient Measurement with STRAFI: Example Mathematica Code

This notebook demonstrates how to fit pulsed gradient spin echo experiments (PGSE) using sinusoidal pulses at a predetermined gradient strength. In this particular example, a PEO and LiTFSI system is being studied with 19F NMR which probes the TFSI anion.

Experimental Note : The experiment was run with G = 10 on the LapNMR. Glycerol calibration indicates that G = 5.6 T/m. The field strenght was 65.6 MHz.

Input Data

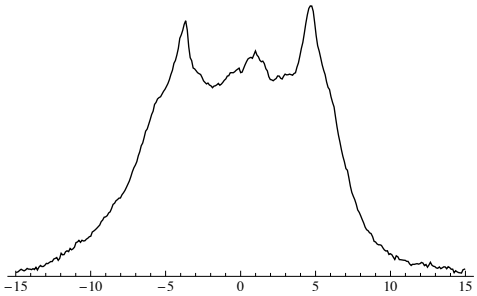
First, the number of two dimensional scans (num2D) and the number of one dimensional acquisition points (numPoints) is entered, along with the gradient list given as a percentage of the maximum gradient used in the experiment. This data was processed prior to being imported into *Mathematica* using the NDFT command in NTNMR followed by any necessary phasing. The data is then imported, and the first four lines - which include the data headers from the NTNMR software - are dropped. The data is then placed into a matrix of NMR spectral data.

```
num2D = 20;
numPoints = 4096;
gradList =
  gradList = {1, 6, 11, 16, 21, 26, 31, 36, 41, 46, 51, 56, 61, 66, 71, 76, 81, 86, 91, 96} / 100;
data = Import["/Users/Shared/Data/19F NMR Data/110408 PEO
     Data/19F PGSE Sinusoidal PEO 90 C_result.txt", "Data"];
data =
  Drop[
   data,
   4];

totalData = Table[{}, {i, 1, num2D}];
For[i = 0, i < num2D,
  (
   For[j = 0, j < numPoints,
     (
      totalData[[i]] =
        Append[totalData[[i]], {data[[j + (i - 1) * numPoints, 3]], data[[j + (i - 1) * numPoints, 1]]}];
     ), j++];
  ), i++];

startValue = -15;
endValue = 15;
finalData = Table[{}, {i, 1, num2D}];
For[i = 0, i < num2D,
  (
   For[j = 0, j < numPoints, If[totalData[[i, j, 1]] > startValue && totalData[[i, j, 1]] < endValue,
      finalData[[i]] = Append[finalData[[i]], totalData[[i, j]]]], j++];
  ),
  i++];
```

```
plot1 = ListPlot[finalData[[1]], Joined → True, PlotRange → All,
  Axes → {True, False}, PlotStyle → {RGBColor[0, 0, 0], Thickness[0.003`]}]
```

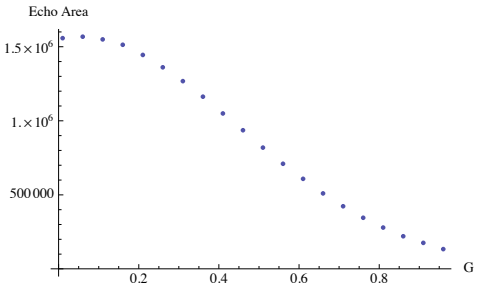


The data is then numerically integrated over the range of interest and transposed into a list of gradient settings and integrated intensities so the data can be fit to extract the self diffusion coefficient.

```
tempSum = 0;
areaList = {};
For[i = 0, i < num2D,
  (
   tempSum = 0;
   For[j = 0, j < Length[finalData[[i]]], tempSum = tempSum + finalData[[i, j, 2]], j++];
   areaList = Append[areaList, tempSum];
  ), i++];

expData = Transpose[{gradList, areaList}];

plot1 =
 ListPlot[expData, PlotRange → All, AxesOrigin → {0, 0}, AxesLabel → {"G", "Echo Area"}]
```



Two pulse Hahn spin echo, ordinary diffusion

The NonlinearRegression package must be imported :

```
Needs["NonlinearRegression`"]
```

The parameters that must be fixed for the PGSE model NonlinearRegression fit include the magnetogyric ratio (γ), the maximum gradient strength(g), the gradient duration (δ) and the diffusion time (Δ).

```
γ = 251.815 * 10^6;
G = 5.6;
δ = 0.005;
Δ = 0.015075;
```

The model equation in this case is different than that ordinarily used for PGSE experiments. While similar to the equation for the PGSE experiment with square gradient pulses, this model accounts for reduced effective gradient resulting from the sinusoidal shape of the gradient pulses. More information can be found in the Price and Kuchel reference in the Bibliography.

```
Clear[A, b, g, d];
model = A * Exp[-γ^2 * d * G^2 * g^2 * δ^2 * (3 * δ * (Cos[π / 2]) ^ 2 + (4 * Δ - δ) * (Sin[π / 2]) ^ 2) * 1 / (π)^2] + b;
```

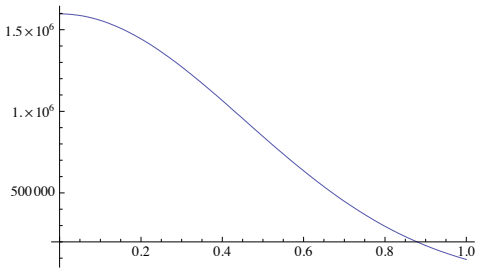
The NonlinearRegress function returns a confidence interval table of the fit for each parameter :

```
dataFit = NonlinearRegress[expData, model, {{d, 10^-11}, {A, 380000.}, {b, 100.}},
   g, RegressionReport → {BestFitParameters, ParameterCITable}];
fit = BestFitParameters /. dataFit;
CITable = ParameterCITable /. dataFit;
CITable
```

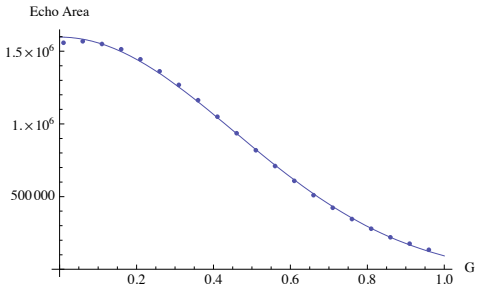
	Estimate	Asymptotic SE	CI
d	8.72643×10^{-12}	6.34326×10^{-14}	$\{8.5926 \times 10^{-12}, 8.86027 \times 10^{-12}\}$
A	1.64969×10^{6}	4.81242×10^{-31}	$\{1.64969 \times 10^{6}, 1.64969 \times 10^{6}\}$
b	-52 659.7	1.12463×10^{-30}	{-52 659.7, -52 659.7}

The fit can then be plotted against the acquired data :

```
A = A /. fit;
d = d /. fit;
b = b /. fit;
plot2 = Plot[model, {g, 0, 1}, PlotRange → All]
```



```
plot3 = Show[plot1, plot2]
```



The fit to the data is quite good. This could be the end of the analysis, but often people want to fit and/or display the data on a semilog plot. The data analysis below demonstrates how this is done.

Changing to a log - x^2 graph ...

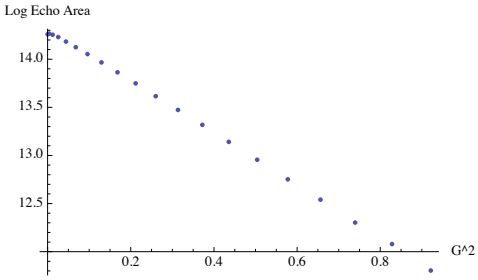
```
Needs["NonlinearRegression`"]
```

First the data is converted to a semilog versus g^2 format:

```
logExpData = Transpose[{gradList^2, Log[areaList]}];
```

We can now plot the data to make sure things look linear, as the model equation suggests that it should :

```
plot4 = ListPlot[logExpData, AxesLabel → {"G^2", "Log Echo Area"}]
```



The data is then fit as above, but this time the model equation will be linear.

```
γ = 251.815 * 10^6;
G = 5.6;
δ = 0.005;
Δ = 0.015075;

Clear[b, g, d];

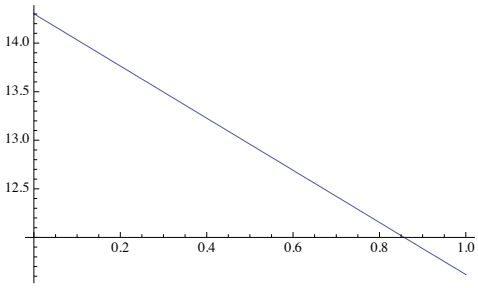
model = -γ^2 * d * G^2 * g * δ^2 * (3 * δ * (Cos[π / 2]) ^ 2 + (4 * Δ - δ) * (Sin[π / 2]) ^ 2) * 1/(π)^2 + b;
```

```
dataFit = NonlinearRegress[logExpData, model, {{d, 10^-11}, {b, 100.}},
   g, RegressionReport → {BestFitParameters, ParameterCITable}];
fit = BestFitParameters /. dataFit;
CITable = ParameterCITable /. dataFit;
```

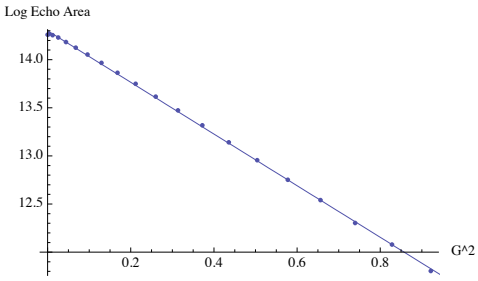
```
CITable
```

	Estimate	Asymptotic SE	CI
d	9.63498×10^{-12}	4.55844×10^{-14}	$\{9.53921\times10^{-12}, 9.73075\times10^{-12}\}$
b	14.3009	0.0054621	{14.2895, 14.3124}

```
d = d /. fit;
b = b /. fit;
plot5 = Plot[model, {g, 0, 1}, PlotRange → All]
```




```
plot6 = Show[plot4, plot5]
```



Again the fit to the data looks very good, and is reasonably close to that seen in the first analysis above. The small difference arises from numerical integration over a small baseline offset. This can be corrected by subtracting the baseline offset found in the first analysis ("b") from the data before taking the natural log of the data. The following analysis demonstrates this procedure.

Changing to a log - x^2 graph and subtracting "b" from areas

The "b" from the first (nonlinear) analysis is defined :

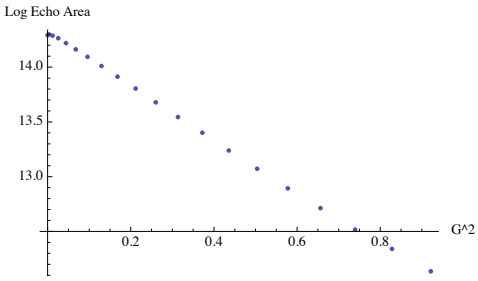
```
b = -52659.67738380773;
```

This is then subtracted from the integrated data ("areaList") before taking the natural log of the data :

```
logExpData = Transpose[{gradList^2, Log[areaList - b]}];
```

The analysis then proceedes as in the linear analysis performed above:

```
plot4 = ListPlot[logExpData, AxesLabel → {"G^2", "Log Echo Area"}]
```




```
γ = 251.815 * 10^6;
G = 5.6;
δ = 0.005;
Δ = 0.015075;

Clear[b, g, d];

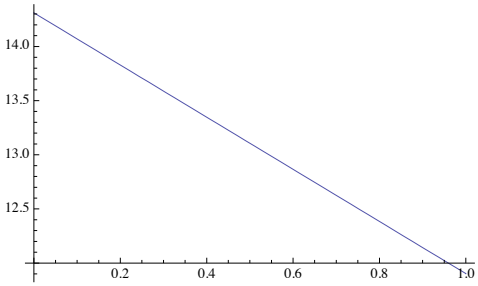
model = -γ^2 * d * G^2 * g * δ^2 * (3 * δ * (Cos[π / 2]) ^ 2 + (4 * Δ - δ) * (Sin[π / 2]) ^ 2) * 1/(π)^2 + b;

dataFit = NonlinearRegress[logExpData, model, {{d, 10^-11}, {b, 100.}},
   g, RegressionReport → {BestFitParameters, ParameterCITable}];
fit = BestFitParameters /. dataFit;
CITable = ParameterCITable /. dataFit;

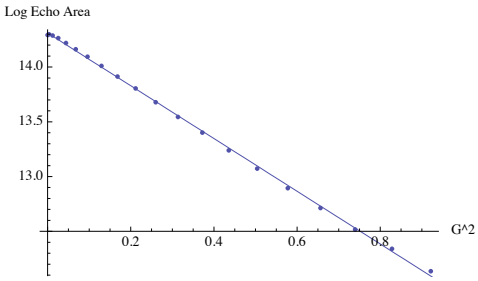
CITable
```

	Estimate	Asymptotic SE	CI
d	8.64504×10^{-12}	5.30429×10^{-14}	$\{8.5336\times10^{-12}, 8.75648\times10^{-12}\}$
b	14.3107	0.0063558	{14.2974, 14.3241}

```
d = d /. fit;
b = b /. fit;
plot5 = Plot[model, {g, 0, 1}, PlotRange → All]
```



```
plot6 = Show[plot4, plot5]
```



Again, the data fit is quite good. The self diffusion coefficient calculated from this regression is within error of that measured by the first proceedure, and is reasonably close (within 10%) of that found with the square pulse field gradient spin echo experiment described elsewhere in this appendix.